Chapter 11: Upper Stratosphere Lower Mesosphere

Chapter lead authors

V. Lynn Harvey	(1) Laboratory for Atmospheric and Space Physics (2) Atmospheric and Oceanic Sciences Department, University of Colorado	USA
John Knox	Department of Geography, University of Georgia	USA

Co-authors

Jeff France	White Ridge Solutions	USA
Masatomo Fujiwara	Faculty of Environmental Earth Science, Hokkaido University	Japan
Lesley Gray	(1) Atmospheric, Oceanic and Planetary Physics, University of Oxford; (2) NERC National Centre for Atmospheric Science	United Kingdom
Toshihiko Hirooka	Department of Earth and Planetary Sciences, Kyushu University	Japan
Peter Hitchcock	Department of Earth and Atmospheric Sciences, Cornell University	USA
Matthew Hitchman	Department of Atmospheric and Oceanic Sciences, University of Wisconsin – Madison	USA
Yoshio Kawatani	Japan Agency for Marine-Earth Science and Technology	Japan
Gloria L. Manney	(1) NorthWest Research Associates; (2) Department of Physics, New Mexico Institute of Mining and Technology,	USA
John McCormack	Heliophysics Division, Science Mission Directorate, NASA Headquarters *previously at Space Science Division, Naval Research Laboratory*	USA
Yvan Orsolini	Norwegian Institute for Air Research	Norway
Takatoshi Sakazaki	Graduate School of Science, Kyoto University	Japan
Yoshihiro Tomikawa	(1) National Institute of Polar Research (2) The Graduate University for Advanced Studies (SOKENDAI)	Japan

Abstract. This chapter focuses on the uppermost levels in the reanalyses, where assimilated data sources are most sparse. The first part of the chapter includes a brief discussion of the effects of the model top and physical parameterizations relevant to the USLM. Long-term signatures of discontinuities in data assimilation and variability among reanalyses are then presented. A climatology of the basic state variables of temperature, horizontal winds, and residual circulation velocities is given. The climatology includes estimates of variability among the reanalyses. Annual cycles highlight the dependence of reanalysis difference on time of year. We then document dominant modes of variability in the reanalyses in the tropical regions and at high latitudes, and longer-term variability including solar cycle, volcanic, ENSO, and QBO signals. The tropical Semi-Annual Oscillation (SAO), the middle atmosphere Hadley circulation, and the occurrence of inertial instability are compared among the reanalyses. High latitude processes considered include polar vortex variability and extreme disruptions therein observed during "elevated stratopause" events. Planetary wave amplitudes are quantified and compared to observations. The chapter ends with a comparison of solar atmospheric tides, 2-day wave amplitudes, and 5-day wave amplitudes in the USLM.

Contents

11.1 Introduction 533
11.1.1 Reanalysis products used in this chapter 533
11.1.2 Satellite observational products 534
11.1.3 Upper boundary conditions in the reanalyses 535
11.1.4 Physical parameterizations in the reanalyses specific to USLM 535
11.1.5 Long-term effects of data assimilation discontinuities 535
11.1.6 Variability among reanalyses 537
11.2 Climatology of the USLM 539
11.2.1 Seasonal zonal means 539
11.2.2 Annual cycles 544
11.2.3 Long-term variability 548
11.3 Tropical Dynamics 552
11.3.1 Semi-Annual Oscillation 552
11.3.2 Middle-atmosphere Hadley circulation 554
11.3.3 Inertial instability 555
11.4 Polar Dynamics 557
11.4.1 Polar vortices 557
11.4.2 Planetary waves 558
11.4.3 Elevated stratopause events 559
11.5 Tides and Normal Modes 562
11.5.1 Tides 562
11.5.2 Quasi-2-day wave 564
11.5.3 Quasi-5-day wave 567
11.6 Summary, Key Findings, and Recommendations 568
References 572
Major abbreviations and terms 579

11.1 Introduction

It is now widely accepted that there are vertical coupling processes that allow the stratosphere to impact surface weather patterns (*Baldwin and Dunkerton*, 2001). Conversely, the upper atmosphere (thermosphere and ionosphere) is strongly influenced by near-surface processes that generate waves that propagate through the stratosphere and mesosphere (*Pedatella et al.*, 2018; *Liu et al.*, 2011; *Goncharenko et al.*, 2010). In between, in the region we refer to as the upper stratosphere and lower mesosphere (USLM), there is a two-way interaction that both affects and is affected by meteorological processes. The modeling of the USLM is therefore critically dependent on meteorological data in the lower and middle atmosphere (*e.g.*, *Pedatella et al.*, 2014) as well as the parameterization of meteorological processes (*e.g.*, sub-grid-scale gravity waves). This chapter compares the reanalysis datasets in the USLM. It is important to document differences at these upper levels because this is the region of the atmosphere where assimilated observations are sparse and differences among the reanalyses are large (*e.g.*, *Chapter 3*; *Long et al.*, 2017). Without an abundance of data to tether forecast models to observations in the USLM, differences in forecast model details may play a prominent role in explaining differences in reanalyses.

The USLM region, apparently first defined as such in the literature by *Gerrard et al.* (2002), is home to numerous dynamical, chemical and other processes of importance for understanding the Earth's atmosphere. Dynamically, at the shortest time scales, mesoscale gravity waves break as they amplify in the rarefied atmosphere or reach critical layers, causing "drag" that closes jet streams and drives meridional circulations, with concomitant thermal and chemical effects (*e.g.*, *Fritts and Alexander*, 2003). Migrating diurnal, semi-diurnal and terdiurnal tides lead to large temperature and wind perturbations in this region (*e.g.*, *Lilienthal et al.*, 2018; *Hagan and Forbes*, 2003). Planetary waves affect this region as well via upward propagation. Perhaps the most spectacular phenomenon, the sudden stratospheric warming (SSW), is driven by planetary wave absorption and breaking and leads to major changes in temperature, wind, and chemistry especially in the high latitudes on the time scales of days to weeks (*Butler et al.*, 2017). At longer time scales, the Semi-Annual Oscillation (*e.g.*, *Smith et al.*, 2017) and the Quasi-Biennial Oscillation (*Baldwin et al.*, 2001), both driven by complex combinations of wave forcings at multiple spatial scales, represent major dynamical and thermal reversals that define many aspects of the tropical and extratropical middle and upper atmosphere. At even longer time scales, changes in the USLM due to solar variability can and do affect its thermal, dynamical and chemical characteristics (*e.g.*, *Beig et al.*, 2008). There is also a rich interplay among these different phenomena that, in many cases, is still to be understood. Since the drivers of these phenomena generally originate in the lower atmosphere and impact regions extending up to the top of the atmosphere, the USLM is in some sense the gateway between "weather" in the troposphere and "space weather" in the thermosphere/ionosphere (*Baker et al.*, 2019). Clearly, an understanding of the USLM benefits not only researchers of the USLM, but those interested in weather and climate from the top to the bottom of the Earth's atmosphere.

In this chapter, we first describe the reanalyses and satellite observations used to evaluate the reanalyses. This is followed by a brief discussion of the effects of the model top and physical parameterizations relevant to the USLM. Long-term signatures of discontinuities in data assimilation and variability among reanalyses are then presented. A climatology of the basic state variables of temperature, horizontal winds, and residual circulation velocities are given. The climatology includes estimates of variability among the reanalyses. Annual cycles highlight the dependence of reanalysis differences as a function of time of the year. We then document dominant modes of variability in the reanalyses in the tropical regions and at high latitudes, and longer-term variability including solar cycle, volcanic, El Niño Southern Oscillation (ENSO), and Quasi-Biennial Oscillation (QBO) signals. The tropical Semi-Annual Oscillation (SAO), the middle-atmosphere Hadley circulation, and the occurrence of inertial instability are compared among the reanalyses. Polar phenomenology evaluated here comprise the polar vortices and extreme disruptions therein observed during "elevated stratopause" events. Planetary wave amplitudes are quantified and compared to observations. The chapter ends with a comparison of solar atmospheric tides, 2-day wave amplitudes, and 5-day wave amplitudes in the USLM.

11.1.1 Reanalysis products used in this chapter

Table 11.1 lists the reanalysis datasets examined in this chapter. These include reanalyses considered in the overall S-RIP project (*Fujiwara et al.*, 2017; also see, *e.g.*, the list given here **https://s-rip.ees.hokudai.ac.jp/pubs/reanalysis.html**) that cover the USLM region with upper air observations assimilated, *i.e.*, the Modern Era Retrospective analysis for Research and Applications version 2 (MERRA-2), MERRA, the European Centre for Medium-Range Weather Forecasts (ECMWF) interim reanalysis (ERA-Interim), the ERA-40, and the latest ERA-5, the Japanese 55-year Reanalysis (JRA-55), the JRA-55C (with only conventional data assimilated), the JRA-55AMIP (with no data assimilated and only constrained by sea surface temperatures), the JRA-25 (covering 25 years from 1979 - 2004) and the combined data records from the Climate Forecast System Reanalysis of NCEP (CFSR) and the Climate Forecast System, version 2 (CFSv2). Note that CFSR is excluded in many comparisons shown in this chapter. The reason for this is that the CFSR top is lower than in the other reanalyses (see *Chapter 2*) and that no pressure levels above 1 hPa are post-processed.

When CFSR is included in comparisons it is only for completeness. For MERRA-2, the M2I3NPASM collection (*GMAO*, 2015a) was used in *Sections 11.1.6*, *11.2* and *11.3*, the M2I6NVANA collection (*GMAO*, 2015b) was used in *Section 11.4*, and the M2I3NVASM collection (*GMAO*, 2015c) was used in *Sections 11.5.2* and *11.5.3*. Users of MERRA-2 reanalyses should be aware of differences between "ANA" and "ASM" products (*GMAO*, 2017) especially when calculating long-term trends in the Hadley Cell (*Garfinkel et al.*, 2015) and when modeling lower stratospheric transport (*Orbe et al.*, 2017). State-of-the-art data assimilation (DA) models such as the Whole Atmosphere Community Climate Model with Data Assimilation Research Testbed are not run operationally and thus are not considered "reanalyses" for the purposes of S-RIP. Comparison of reanalyses, observations, and high-top DA models is the subject of future work. A few essential details of the reanalysis systems relevant to the USLM are given in the references in **Table 11.1**, including the model top altitude and the gravity wave parameterizations that play a key role in the characteristics of this region. The reader is directed to *Chapter 2* and *Fujiwara et al.* (2017) for more details on the models, including a comprehensive list of assimilated observations, model parameterizations, and changes to the models over time. In the following sections, key points regarding the reanalyses and the observations to which they are compared are briefly summarized for ease of reference.

Table 11.1: *List of reanalysis datasets used in this chapter, overall references, model top altitude, and gravity wave specifications. In the 4th column, ORO refers to the parametrization for orographic gravity waves while NON refers to that of non-orographic gravity waves.*

Reanalysis Dataset	Reference	Model Top (hPa)	Gravity Wave Drag Parameterizations
MERRA	*Rienecker et al.* (2011)	0.01	ORO: *McFarlane* (1987) NON: *Garcia & Boville* (1994)
MERRA-2	*Bosilovich et al.* (2015); *Gelaro et al.* (2017); *Molod et al.* (2015)	0.01	ORO: *McFarlane* (1987) NON: *Garcia & Boville* (1994); *Molod et al.* (2015)
ERA-40	*Uppala et al.* (2005)	0.1	ORO: *Lott & Miller* (1997) NON: none
ERA-Interim	*Dee et al.* (2011)	0.1	ORO: *Lott & Miller* (1997) NON: none
ERA5	*Hersbach & Dee* (2016)	0.01	ORO: *Lott & Miller* 1997; NON: *Orr et al.* (2010)
JRA-55 JRA-55C JRA-55AMIP	*Kobayashi et al.* (2015)	0.1	ORO: *Iwasaki et al.* (1989a, b) NON: none
JRA-25	*Onogi et al.* (2007)	0.4	ORO: *Iwasaki et al.* (1989a, b) NON: none
NCEP-CFSR	*Saha et al.* (2010)	~0.266	ORO: *Kim & Arakawa* (1995); *Lott & Miller* (1997) NON: none
CFSv2	*Saha et al.* (2014)	~0.266	ORO: *Kim & Arakawa* (1995); *Lott & Miller* (1997) NON: *Chun & Baik* (1998)

11.1.2 Satellite observational products

Throughout this chapter and in science studies that employ reanalyses, it is critically important to compare the reanalyses to independent data sources whenever possible. This analysis step acts to quantify model biases (either known or unknown) and establishes a level of consistency between the reanalysis fields and observations. The following satellite datasets appear in this chapter for this purpose.

The Earth Observing System (EOS) Microwave Limb Sounder (MLS) satellite data record spans August 2004 to the present and provides ~3500 vertical profiles of temperature, geopotential height (from which horizontal winds can be derived) and trace gases each day that cover the globe (*Waters et al.*, 2006). The retrieval methods and error estimates for the most recent version-4 data products are given by *Livesey et al.* (2017). Some of the comparisons among reanalyses shown in this chapter also include MLS data to provide a (mostly) independent reference point. Note that MERRA-2 assimilates MLS temperature at pressures 5 hPa and less starting in October 2004. Likewise, ERA-Interim, MERRA-2, and ERA5 assimilate MLS ozone profiles starting in 2008, 2004, and 2004, respectively (see *Chapter 2* and **Tables 2.10**, **2.20**, and **2.22**). An advantage of comparing reanalyses to MLS observations is that the consistent near-global coverage does not result in data gaps at polar latitudes.

The Thermosphere, Ionosphere, Mesosphere, Energetics and Dynamics (TIMED) satellite launched in December 2001 provides daily near-global measurements of ozone, temperature, and geopotential height from the troposphere up to the lower thermosphere. The Sounding of the Atmosphere using Broadband Emission Radiometry (SABER) instrument aboard TIMED is a 10-channel radiometer that measures infrared Earth limb emissions. On any given day, SABER observes from the ~82° latitude in one hemisphere to 52° latitude in the other. The TIMED satellite then "yaws" to allow SABER to view the other pole every ~60 days. SABER temperature profiles have 2 km vertical resolution and estimates of precision are within 4 K throughout the mesosphere (*Remsberg et al.*, 2003). Since SABER data are not currently assimilated into any of the reanalysis systems they provide an important independent reference point for comparison in the USLM.

Ultimately, the observational datasets employed in each of the following sub-sections depend on the choice of the author(s) writing each sub-section. Future users of reanalysis data products in the USLM are encouraged to compare to other data sources not necessarily listed above. These include other national and international satellite data, ground-based radars and lidars, and sub-orbital rocket data. While some of these data sources are inherently geographically sparse, all provide an invaluable source of independent data with which to establish the fidelity of USLM reanalysis output products and place scientific results on more solid footing.

11.1.3 Upper boundary conditions in the reanalyses

The results in this chapter are, to a larger degree than in the other S-RIP chapters, impacted by the effects of proximity to the model top. The approximate vertical grid spacing of the reanalyses becomes coarser nearer the model top, from about 1.5 km for MERRA and MERRA-2 in the upper stratosphere to 8 km for the CFSR and CFSv2 in the lower mesosphere. See **Figure 3** in *Chapter 2* for more detailed information on vertical grid spacing. Sponge layers are employed in the models used in the reanalyses to avoid problems created by a "rigid lid" top, which would otherwise spuriously reflect wave energy. Different reanalyses implement sponge layers differently, thus the reader is referred to S-RIP *Chapter 2* for more information and references regarding sponge layers and model top treatments. Briefly, the MERRA/MERRA-2 sponge layer is applied by increasing the divergence damping coefficient in the topmost nine layers, while also reducing the order of advection in the top model level to a first-order scheme (*Bill Putman, personal communication*, 2018). The ERA reanalyses' sponge layer covers the atmosphere above 10 hPa in which an additional term is applied to horizontal diffusion specifically to absorb vertically propagating gravity waves. This means the K coefficient is multiplied by a factor that depends on wavenumber and model level, consistent with "enhanced hyperdiffusion in the sponge layer". Rayleigh drag is also applied above 10 hPa in ERA-40 and above the stratopause in ERA-Interim. In JRA-25 and JRA-55, gradually larger horizontal diffusion coefficients are applied for pressures of less than 100 hPa in the data assimilation system, and Rayleigh friction is also applied to the temperature deviations from the global average at pressures less than 50 hPa (see *Chapter 2*, **Table 2.3**). CFSR, like JRA, also uses gradually increasing horizontal diffusion coefficients with increasing height; like ERA, CFSR also uses Rayleigh drag beginning in the upper stratosphere, at pressures less than 2 hPa. It is important to keep in mind that sponge layers, while minimizing the obvious contamination effects of unrealistic gravity wave reflection, can also introduce spurious effects of their own in winds and temperature (*Shepherd et al.*, 1996).

11.1.4 Physical parameterizations in the reanalyses specific to USLM

The model parameterizations that have the largest impact in the USLM involve horizontal diffusion and the methods that account for small-scale gravity waves, both orographic and non-orographic. Horizontal diffusion is represented by implicit linear 4th order (for ERA-40, ERA-Interim, JRA-25, and JRA-55) or 8th order (for CFSR/CFSv2) diffusion in spectral space. For MERRA and MERRA-2, horizontal diffusion is accounted for using explicit 2nd order horizontal divergence damping. See *Chapter 2* **Table 2.8** for differences in the treatment of horizontal diffusion among the reanalyses. Each reanalysis center treats orographic gravity waves differently (see **Table 11.1** for references that describe each scheme; see *Chapter 2*, **Table 2.7** for additional details). Of the reanalysis datasets used in this chapter, only MERRA, MERRA-2, and CFSv2 apply non-orographic gravity wave drag schemes (see *Chapter 2,* **Table 2.7** and *Fujiwara et al.* (2017), **Table 3** and discussions therein for more details). The MERRA-2 non-orographic gravity wave parameterization has been modified from that used in MERRA by increasing the background source at certain latitudes and by increasing the intermittency (*Molod et al.*, 2015). As noted in the previous section, Rayleigh drag is used in several of the reanalyses, both in the USLM and below it, both to simulate non-orographic gravity wave drag (in the ERA-Interim) and also more generally as a damping/sponge effect. The use of Rayleigh drag to simulate non-orographic gravity wave drag is problematic, since these waves can have substantial phase speeds.

11.1.5 Long-term effects of data assimilation discontinuities

Reanalysis efforts aim to minimize the effects of discontinuities to a given assimilation system. However, there remain discontinuities in the data records due to differences in the data that are assimilated from year to year (*e.g.*, *Chapter 3; Long et al.*, 2017; *Simmons et al.*, 2014). To discuss discontinuities, we need to describe (1) major observations assimilated, and (2) execution streams, because they are the main sources of discontinuities in reanalysis time series. What follows is a brief synopsis of *Chapter 3.3*, where additional details can be found.

Because radiosondes generally do not reach the upper stratosphere, the major observations that are assimilated in this region are satellite-based. The ERA-40 reanalysis used SSU data, which introduced discontinuities because of the multiple NOAA polar orbiters that provided SSU data. The ERA-Interim has biases as a result of the polar orbiter issue in 1985 and, in 1998, the transition from TOVS to ATOVS. The reader is referred to *McLandress et al.* (2014) for a characterization of these discontinuities and a numerical method to remove them. Similarly, the JRA-25 also has a discontinuity in 1998 because of the transition from TOVS to ATOVS.

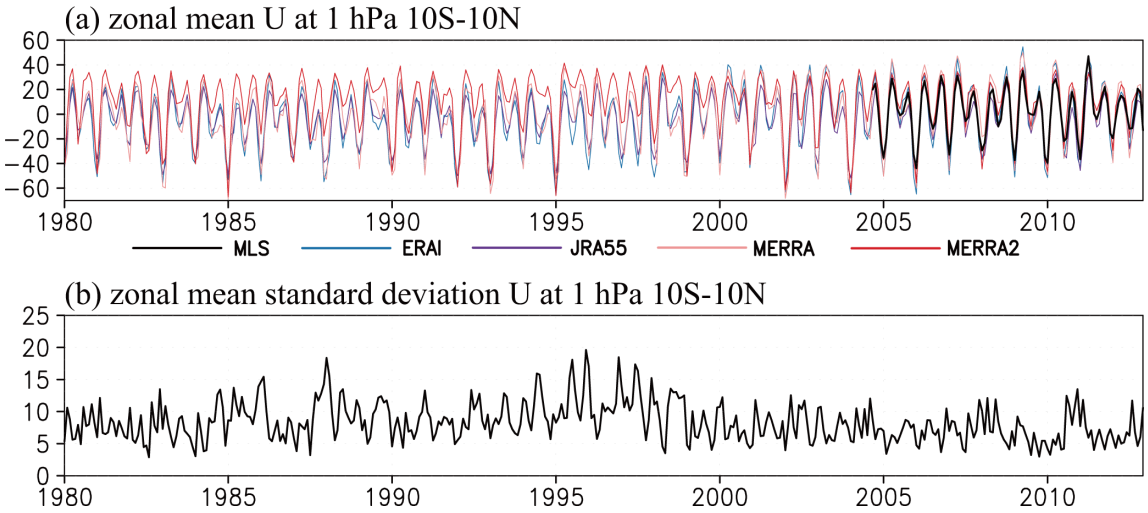

Figure 11.1: *35-year time series at 1hPa from 10°S-10°N of (a) zonal mean zonal wind in 4 reanalyses and MLS and (b) zonal mean zonal wind standard deviation among the reanalyses. Winds are in ms^{-1}. Figure 11.1a is modified from Kawatani et al. (2020).*

The CFSR has multiple discontinuities in the middle and upper stratosphere in 1986, 1989, 1994, 1999, 2005, 2009 due to multiple execution streams and a biased SSU bias correction method. MERRA-2 has discontinuities in 1995 (SSU), 1998 (transition to AMSU) and 2004 (transition to MLS Aura). In general, the discontinuities are less of a factor from 1998 onward, in the post-SSU era.

Now we examine a few examples of how the discontinuities affect phenomena in the USLM. **Figure 11.1** reveals some of the impacts of these discontinuities in winds near the stratopause (at 1 hPa, near 50 km). The black line in panel (**a**) shows monthly and zonally averaged zonal winds estimated by MLS geopotential heights (*Smith et al.,* 2017). This method obtains tropical zonal winds by cubic spline interpolation of the balanced winds across the Equator. The zonal winds estimated using MLS and SABER are in good agreement at most altitudes (see **Figure 1** of *Smith et al.*, 2017). **Figure 11.1** shows that reanalysis zonal winds are in agreement with those estimated from MLS data. A notable difference among the reanalyses is that the westerlies in MERRA-2 are larger than the other reanalyses during the 1980s and most of the 1990s. This MERRA-2 bias prior to 1998 results in larger standard deviations among the reanalyses, as shown in panel (**b**). The reader is referred to *Kawatani et al.* (2020) for representation of the equatorial zonal wind in the USLM in several reanalyses and satellite observations.

In order to quantify the spread among reanalyses, the 3D standard deviations among the reanalyses ($\sqrt{\sum (u_i - [u])^2/N}$) are calculated, where i labels the individual datasets and there are N datasets included. The square brackets denote the mean over all N reanalyses (*cf.*, *Kawatani et al.*, 2016). The standard deviation is calculated for each month using monthly mean zonal wind. **Figure 11.1** panel (**b**) shows that the zonal mean standard deviation among the reanalyses is larger prior to 1998 compared to the period after 1998, consistent with expectations.

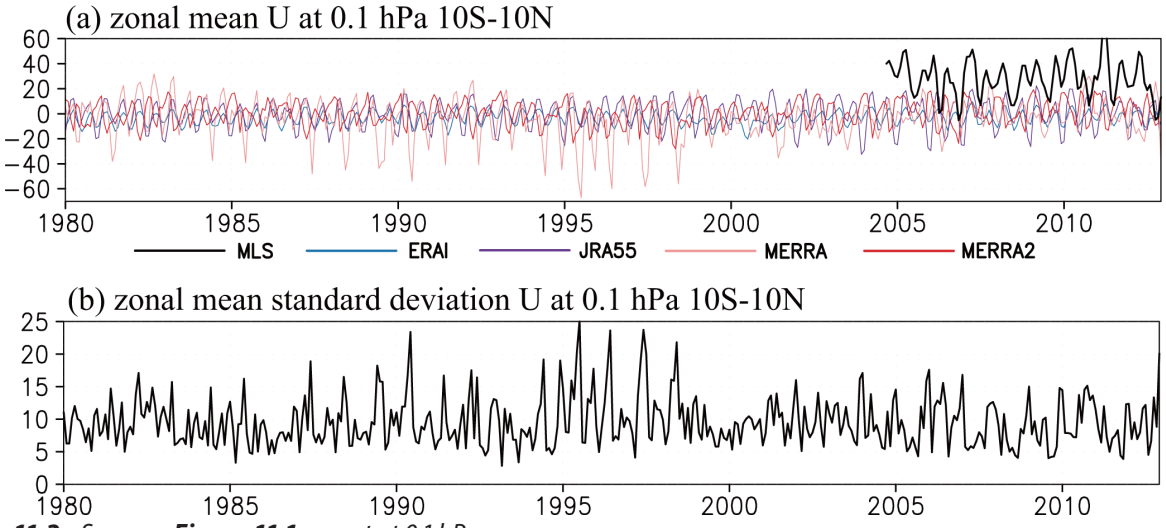

Figure 11.2: *Same as* ***Figure 11.1*** *except at 0.1 hPa.*

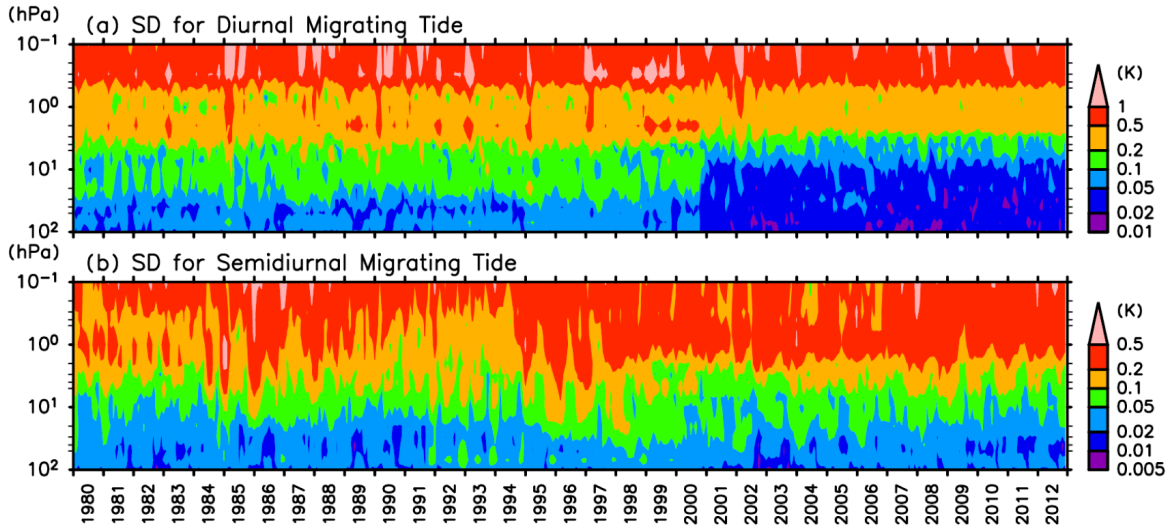

Figure 11.3: *32-year altitude-time section of the standard deviation averaged over 10 °S - 10 °N in the amplitude of the (a) diurnal and (b) semidiurnal temperature tide using MERRA, MERRA-2, ERA-Interim and JRA-55.*

Temporal discontinuities in the zonal winds are especially obvious at lower mesospheric altitudes. **Figure 11.2** of zonal winds at 0.1 hPa (near 60 km) shows strong easterlies in MERRA for the period before 1998 (panel **a**) that are not corroborated by the other reanalyses.This MERRA bias results in the standard deviations among the reanalyses being larger prior to 1998 (panel **b**). These results are consistent with *Das et al.* (2016) (see their **Figure 4a**, top panel) who showed 1) a MERRA easterly bias in the tropical zonal winds in the USLM (compared to rocket observations) during 1979 - 1991 and 2) that this easterly bias disappeared after 1998. Reanalyses zonal winds do not agree with the MLS winds due to different time-mean values (~ 28 m s^{-1} for the MLS and ~ 0 m s^{-1} for reanalyses, see also **Fig. 11.6**).

Atmospheric tides are also affected by temporal discontinuities in input data. In **Figure 11.3**, the impact of differences in the data assimilation stream on the diurnal (panel **a**) and semidiurnal (panel **b**) tides is depicted. See *Sakazaki et al.* (2018) for interannual variability in individual reanalysis datasets. In the stratosphere, the variance in the diurnal temperature tidal amplitudes among the reanalyses is significantly larger (note the logarithmic color scale) before 2000 compared to later years. In the lower mesosphere the variance among the reanalysis data sets is large (~ 1 K) and fairly steady throughout the entire record. The reanalyses are presumably strongly dependent on the tides simulated in the forecast model used in producing each reanalysis in this altitude region. An abrupt change due to the TOVS-to-ATOVS transition around 2000 is not apparent for the semidiurnal tide (panel b). However, a decadal variation is seen before ~2000 (*e.g.*, relatively large variance around 1985 and 1995 above 10 hPa level). This is caused by anomalously large interannual variations in ERA-Interim, which are likely related to the orbital drift of TOVS and the transition between different NOAA satellites carrying the TOVS (*Sakazaki et al.*, 2018)

11.1.6 Variability among reanalyses

As shown in the previous section, significant differences in the tropical zonal winds exist among the different reanalysis datasets. This section quantifies those differences for zonal mean temperature and zonal mean zonal winds over a range of latitudes and altitudes. These differences are likely conservative estimates and day-to-day differences among the reanalyses are likely larger. Data users are advised to keep in mind the magnitude of these differences when drawing scientific conclusions.

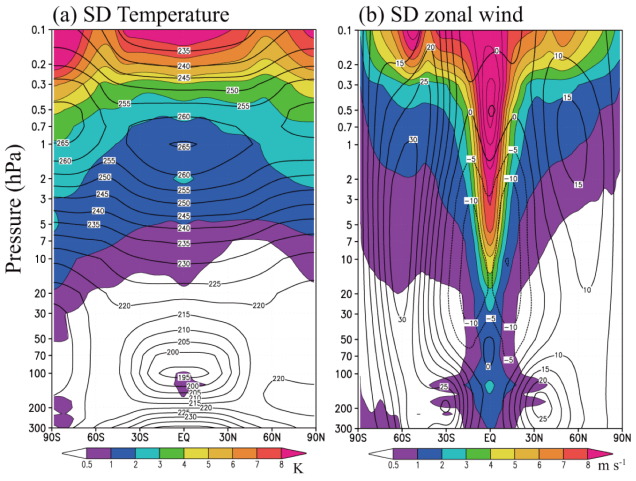

Figure 11.4: *Latitude-altitude distribution of zonal mean and time mean (1980 - 2012) standard deviation (color fill) of (a) temperature and (b) zonal winds among the four reanalyses (ERA-Interim, JRA-55, MERRA, MERRA-2). Annually averaged zonal-mean temperature contours every 5 K are added to (a) and zonal winds contours every 5 m s^{-1} are added to (b) where westerlies are solid and easterlies are dotted. Modified from Kawatani et al. (2020).*

In **Figure 11.4**, a comparison of cross-sections of zonal mean and time mean (1980 - 2012) standard deviations of temperature (panel **a**) indicates increasing differences among four reanalyses (ERA-Interim, JRA-55, MERRA, and MERRA-2) with height into the mesosphere at all latitudes. The latitudinal dependence of the differences is rather weak, though the differences are somewhat smaller in the equatorial upper stratosphere and slightly larger in the Southern Hemisphere (SH) stratosphere and mesosphere than in the Northern Hemisphere (NH). Above about 10 hPa there are limited data and different models create different solutions that lead to differences in variability. Another factor contributing to variability among the reanalyses are sponge layers in the mesosphere of the JRA-55 and ERA-Interim models, leading to the broad large standard deviation region above ~1 hPa. MERRA and MERRA2, which have a much higher top, do not have significant sponge-layer damping below 0.2 hPa (see *Chapter 2; Kawatani et al.*, 2020).

The zonal wind standard deviation (**b**) increases in the equatorial region and with increasing height. There is a notable "v-shape" of increased variability in the Tropics in **Figure 11.4b**. These results are consistent with Das et al. (2016) (see their **Figure 5a**, left panel) who showed root-mean-square differences between reanalysis and rocket observed zonal winds in the Tropics that increased linearly with altitude. One possible explanation is the relatively weak constraints of the thermal wind balance associated with satellite temperature observations over the Equator (*Kawatani et al.*, 2016). Without strong data constraints in the USLM (see previous section), differences among reanalyses such as MERRA and MERRA-2 are likely ascribable to model differences (*Krzysztof Wargan, personal communication*, 2018). The lack of a non-orographic gravity wave parameterization in JRA-55 may also contribute to its variability relative to other reanalyses (*Yayoi Harada, personal communication*, 2018).

Figure 11.5 depicts standard deviations of temperature in the lower mesosphere (**a**) and at the stratopause (**c**) and for zonal wind in the lower mesosphere (**b**) and at the stratopause (**d**) in plan view. Standard deviations are averages from 1980 to 2012. Overall, the temperature and zonal wind standard deviations are much larger in the mesosphere (top panels) than in the stratosphere (bottom panels). Panels (**a**) and (**c**) show that temperature differences among the reanalyses are relatively large in the polar region at both levels. There are no data assimilated at 0.1 hPa (except MLS in MERRA-2 after August 2004), so these differences result largely from model performance. Panel (**b**) shows that in the lower mesosphere, areas of large standard deviation in the zonal wind are globally spread with two maxima at the Equator and 50 °S. Smaller variability over the North Pacific at 0.1 hPa compared to other longitude sectors may be due to weaker zonal winds associated with the climatological Aleutian anticyclone (*Harvey and Hitchman*, 1996).

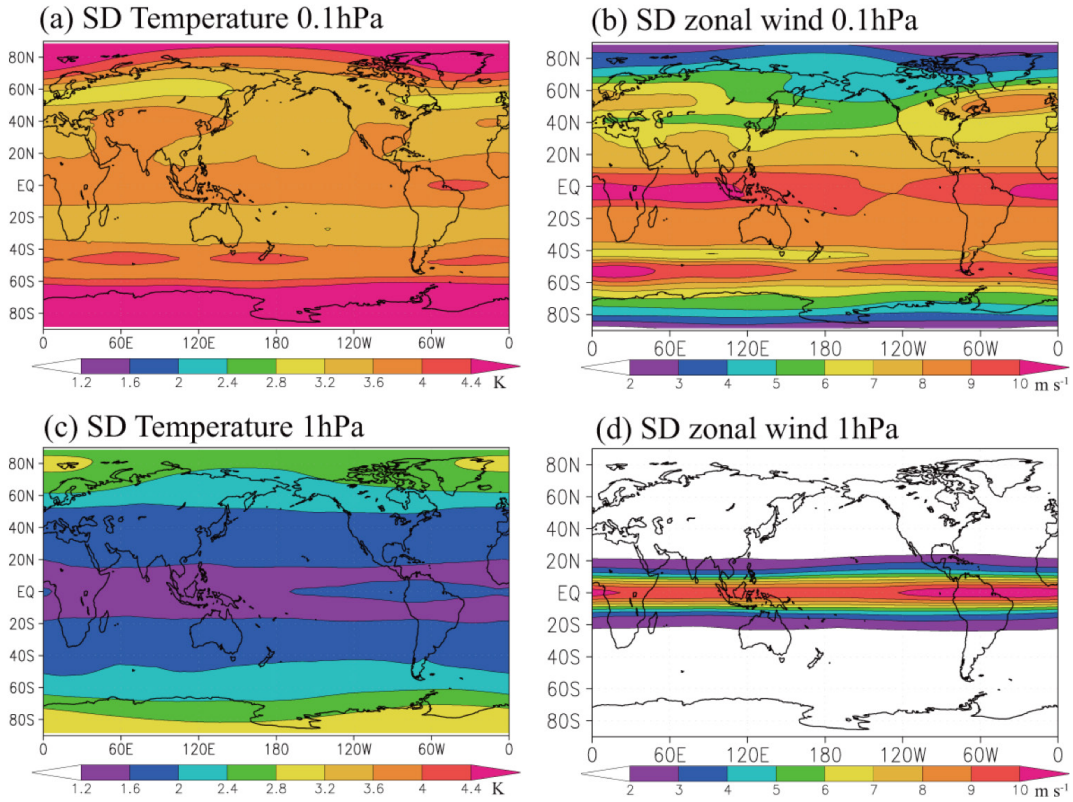

Figure 11.5: *Mercator maps at 0.1 hPa (top) and 1 hPa (bottom) of the standard deviation among reanalysis temperature (panels a and c) and zonal wind (panels b and d). Temperature is in degrees K and wind is in m s^{-1}. Figures 11.5b and 11.5d are modified from Kawatani et al. (2020).*

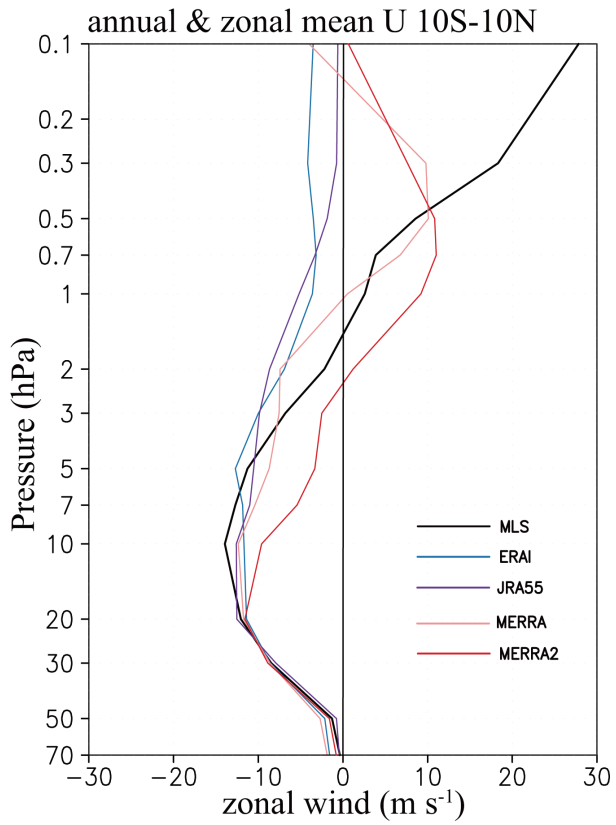

Figure 11.6: *Vertical profiles of climatological annual mean zonal mean zonal winds averaged from 10°S - 10°N in four reanalyses (MERRA, MERRA-2, ERA-Interim, and JRA-55). MLS gradient winds are shown in black. Modified from Kawatani et al. (2020).*

The largest spread in the SH occurs where a strong polar night jet exists. Large differences among the reanalyses may trace back to the large absolute value of variability in this region. At 1 hPa (panel **d**) areas of large standard deviation are well concentrated near the Equator with relatively small zonal variability. Note that the 0.1 hPa levels correspond to sponge layers in ERA-Interim and JRA-55. Due to this, the physical interpretation of differences in the mesosphere is less clear.

Figure 11.6 summarizes the climatological (1980 - 2012) annual average inter-reanalyses differences in the zonal mean zonal wind near the Equator, where wind differences maximize. The black line shows the MLS zonal wind averaged from September 2004 to August 2014. Westerly biases in MERRA-2 are large between 10 hPa and 1 hPa. Since MERRA-2 includes a non-stationary gravity wave parameterization it may result in a westerly bias (*Coy et al.*, 2016; *Molod et al.*, 2015). More investigation is needed to quantify this potential bias. Westerly MLS gradient winds are stronger than all of the reanalyses above 0.5 hPa. *Section 11.3* will demonstrate that this is due to the emergence of summer SAO easterlies in most reanalyses that offset equinox westerlies and time-average to be near zero. Weak time-mean zonal winds in ERA-I and JRA55 above 1 hPa are attributed to sponge layer effects. However, MERRA and MERRA2 time-mean winds also converge to zero but do not suffer as much from sponge layer effects at these altitudes. The reader is cautioned that satellite-derived gradient wind approximations are not particularly accurate in the equatorial mesosphere because of the importance of Reynolds stress terms, *e.g.*, from the diurnal tide, and thus the MLS wind values at 0.1 hPa may be overestimated (*McLandress et al.*, 2006). That said, MLS and SABER agree with each other (*Smith et al.*, 2017) and with rocketsonde observations (*Kishore Kumar et al.*, 2015). Overall, users of reanalysis zonal wind data in the tropical USLM are cautioned to keep these large differences in mind when drawing scientific conclusions.

11.2 Climatology of the USLM

In this section we describe the climatology of the USLM in different reanalyses, giving a closer look at this region than provided in *Chapter 3*. Reanalysis data used in this section include MERRA, MERRA-2, ERA-Interim, JRA-25, JRA-55, and ERA-40. For comparison, data were interpolated to common grids by taking the following steps: 1) Monthly- and zonal-mean data were computed from the original data. 2) Data on common pressure levels were extracted. These pressure levels consist of the following 26 levels: 1000, 925, 850, 700, 600, 500, 400, 300, 250, 200, 150, 100, 70, 50, 30, 20, 10, 7, 5, 3, 2, 1, 0.7, 0.5, 0.3, 0.1 hPa. 3) All the common pressure level data were linearly interpolated onto the common latitudinal grid every 1.5 degree (*i.e.*, same as ERA-Interim). 4) The 1980 - 2001 common time period is used. This time period precludes large differences that would arise if years since 2004 were included, due to the assimilation of MLS into MERRA-2. Note that this common time period is different from that used in *Chapter 3* (1980 - 2010), hence anomalies may be different. Residual-mean meridional and vertical velocities are given by the Transformed Eulerian-Mean (TEM) formulation (*Andrews et al.*, 1987).

11.2.1 Seasonal zonal means

Here we provide a global "atlas" of seasonal (*i.e.*, December-January-February (DJF), March-April-May (MAM), June-July-August (JJA), and September-October-November (SON)) zonal means of temperature, Eulerian zonal and meridional winds, and Lagrangian TEM residual circulation velocities averaged over 1980 - 2001 for each of the six reanalyses listed above and their differences from MERRA (Reanalyses minus MERRA). MERRA was chosen as a reference because it covers the lower mesosphere above 1 hPa and has been widely used. However, this does not imply that MERRA should be considered "truth". In fact, if differences are similar among multiple reanalyses then this likely indicates that MERRA is biased.

Figure 11.7 shows latitude-pressure sections of seasonal zonal means of temperature. Here, data above 1 hPa are available only for MERRA and MERRA-2.

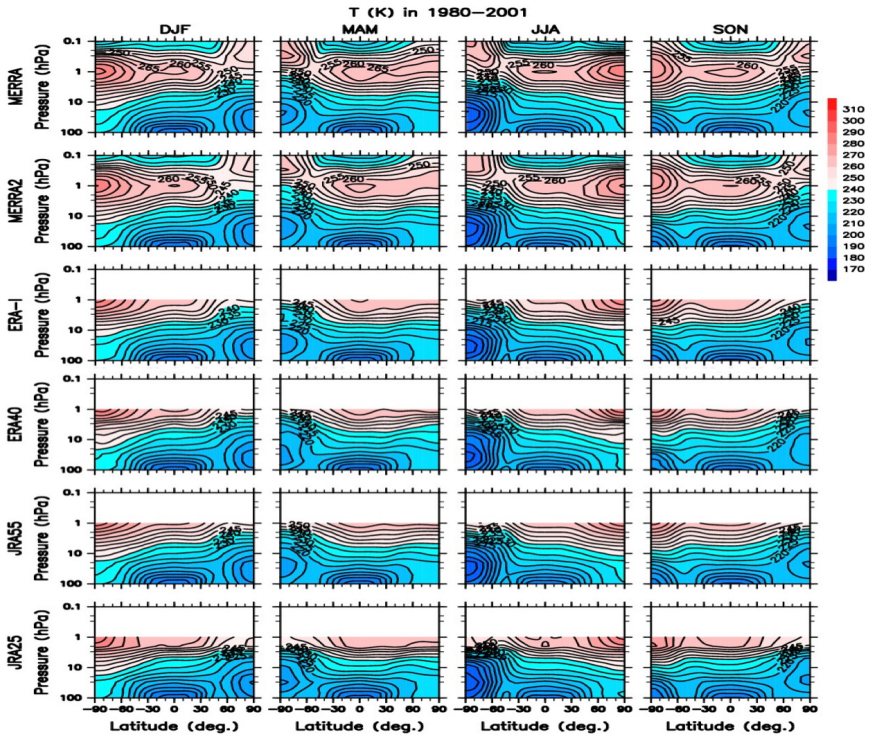

Figure 11.7: *Latitude-pressure sections of seasonal zonal-mean temperature averaged over 1980 - 2001 from MERRA, MERRA-2, ERA-Interim, ERA-40, JRA-55, and JRA-25. Contour intervals are 5 K.*

Overall features of the temperature distributions are similar among all the available reanalyses except for JRA-25, in which an anomalous vertical temperature gradient is seen around 3 hPa. This is induced by systematic positive and negative temperature biases in the upper and middle stratosphere, respectively (see also **Fig. 11.8**), which result from problems in the radiative transfer model used in JRA-25 (*Onogi et al.*, 2007). The stratopause is located around 1 hPa both in MERRA and MERRA-2 except for polar autumn and winter, during which it is located above 1 hPa (*e.g.*, *Hitchman et al.*, 1989).

Temperature differences from MERRA are shown in **Figure 11.8**. While the latest reanalyses (*i.e.*, MERRA-2, ERA-Interim, and JRA-55) show small differences (*i.e.*, mostly < 1 K) below 10 hPa, ERA-40 and JRA-25 show large differences (*i.e.*, > 2 K) from the latest reanalyses even below 10 hPa. On the other hand, there can be seen vertically stacked structures of temperature differences with large magnitudes (*i.e.*, > 2 K) above 10 hPa even for the latest reanalyses. MERRA-2 has positive and negative temperature differences between 10 hPa and 3 hPa and between 3 hPa and 0.3 hPa, respectively, and the magnitude of these anomalies is larger in the polar regions. ERA-Interim has positive and negative temperature differences from MERRA at 10 hPa and 1 hPa, respectively, which are especially large in the SH winter extratropics. JRA-55 has negative temperature differences between 10 hPa and 1 hPa in the tropical and mid-latitude regions and positive differences in the polar regions in autumn and winter between 3 hPa and 1 hPa. In JRA-25, there are weak vertical temperature gradients above ~ 2 - 3 hPa, due to sponge layer effects, that give rise to large vertical gradients in the temperature differences between JRA-25 and MERRA (bottom row). To summarize, temperature differences (with respect to MERRA) are often substantial among older and newer reanalyses, in both the lower and upper stratosphere, and ranging from the tropics to the high latitudes.

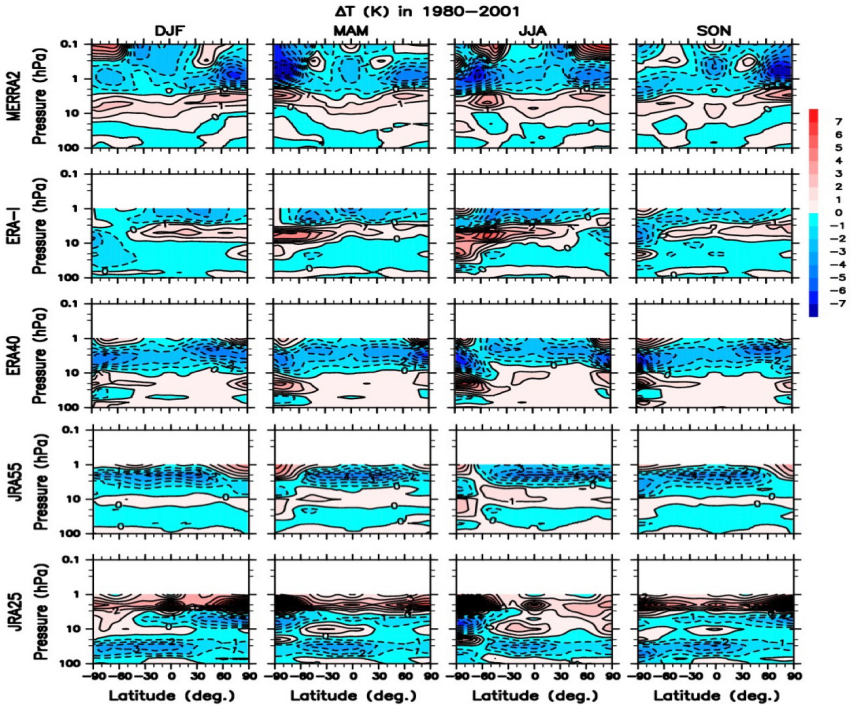

Figure 11.8: *Same as* ***Figure 11.7*** *except for differences from MERRA. Contour intervals are 1 K.*

Figure 11.9 shows latitude-pressure sections of seasonal zonal means of zonal wind.

Westerly and easterly jets in the winter and summer stratosphere, respectively, are well reproduced in all the available reanalyses. An equatorward tilt of the polar-night westerly jet in autumn and winter is common to all the available reanalyses. Likewise, all reanalyses show a poleward-tilting summer easterly jet (except for the NH summer jet in MERRA, which tilts poleward below 1 hPa and equatorward above that level).

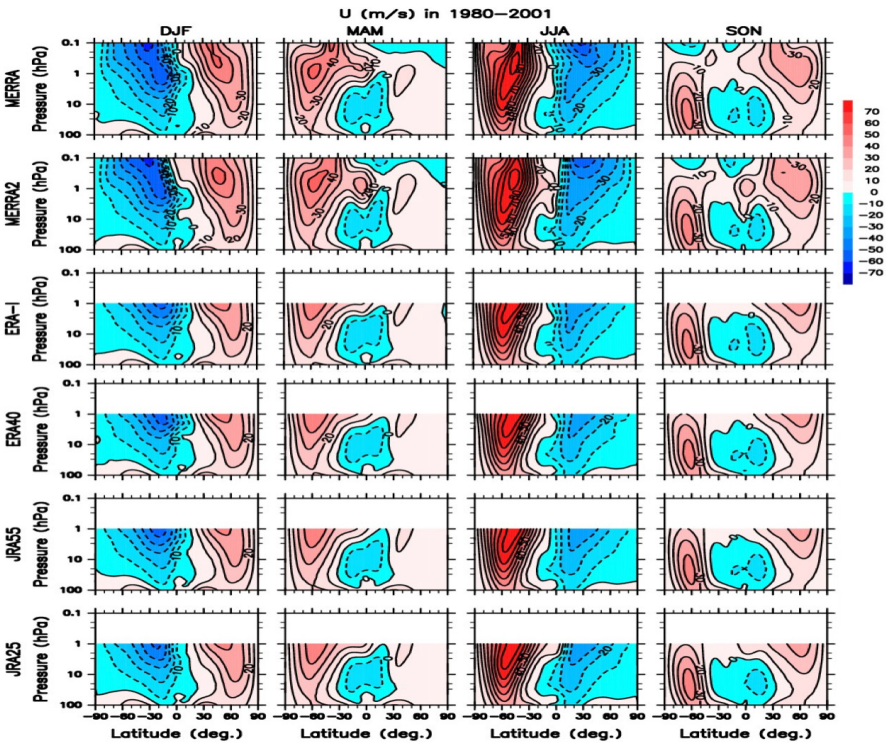

Figure 11.9: *Same as* ***Figure 11.7*** *except for zonal wind. Contour interval is 10 m s^{-1}.*

Zonal wind differences from MERRA are shown in **Figure 11.10**. Differences among reanalyses are largest (*i.e.*, > 4 m s^{-1}) in the tropical stratosphere (and mesosphere), which is probably due to the dearth of wind observations assimilated and because the available temperature observations do not provide a strong constraint on the wind in the deep Tropics. MERRA-2 shows a year-round positive (westerly) bias near the tropical stratopause and semi-annually oscillating differences in the tropical mesosphere compared to MERRA.

Figure 11.11 and **Figure 11.12** depict latitude-pressure sections of seasonal means of Eulerian-mean and residual-mean meridional winds, respectively. The residual-mean meridional (and vertical) winds were computed from Eulerian-mean winds and resolved wave fluxes on the primitive equation system (*cf., Andrews et al.*, 1987). Eulerian-mean meridional wind shows a strong equatorward flow in the polar-night jet regions especially in the NH, which does not appear in the residual-mean meridional flow. This feature is also seen in the SH spring (SON) because of the persistent SH polar vortex. Other features in the stratosphere hardly change between Eulerian-mean and residual-mean flows, suggesting that the divergence of the eddy heat flux of Rossby waves is small. MERRA and MERRA-2 show the Eulerian-mean equatorward flow up to 0.2 hPa in the polar-night jet region, above which sponge layer effects may obscure the upward propagation of planetary waves. Another interesting feature is that both Eulerian-mean and residual-mean meridional flows above 1 hPa in MERRA and MERRA-2 have a weak negative peak around 20°S in addition to a strong negative peak around 60°S in MAM and JJA (*i.e.*, austral autumn and winter).

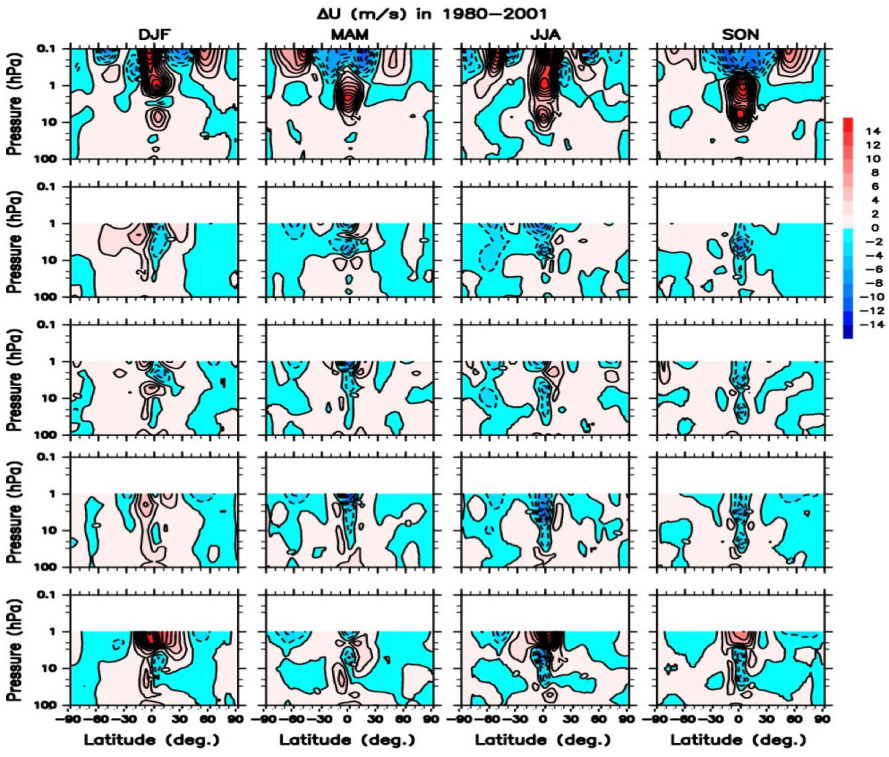

Figure 11.10: *Same as* ***Figure 11.8*** *except for zonal wind. Contour interval is 2 m s^{-1}.*

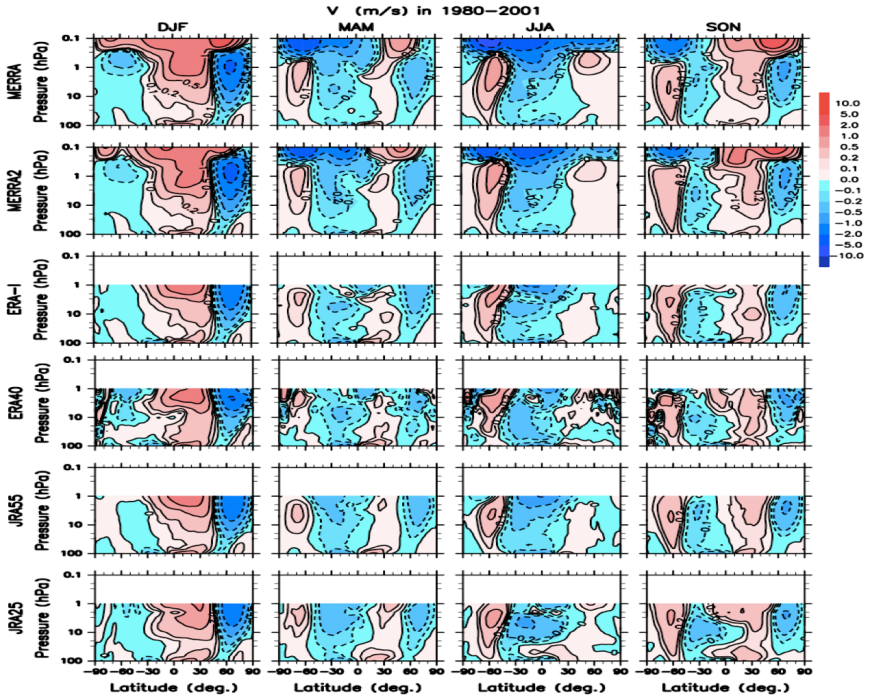

Figure 11.11: *Same as* ***Figure 11.7*** *except for meridional wind. Contour intervals are logarithmic to emphasize small speeds.*

Their extension down to 1 hPa is also partially seen in ERA-Interim and ERA-40, but not in JRA-55 and JRA-25 (see **Figure 11.12**). This meridional flow is likely driven by parameterized gravity wave drag in the forecast model. Gravity-wave resolving GCMs such as KANTO (*Watanabe et al.*, 2008) and KMCM (*Becker and Vadas*, 2018) do not show such separated peaks of gravity wave drag in the SH winter mesosphere. This suggests that meridional propagation of gravity waves neglected in the gravity wave drag parameterization is essential for the representation of the meridional circulation in the mesosphere (*cf.*, *Sato et al.*, 2009). It is also worth noting that both Eulerian-mean and residual-mean meridional flows in ERA-40 are noisier than those in the other reanalyses in the polar regions. This may be linked to the noisier vertical velocity in ERA-40 (*e.g.*, *Iwasaki et al.*, 2009; *Monge-Sanz et al.*, 2007; see also **Figs. 11.15**, **11.16**) through mass continuity; thus, science studies based on ERA-40 residual circulation velocities would likely generate noisier results.

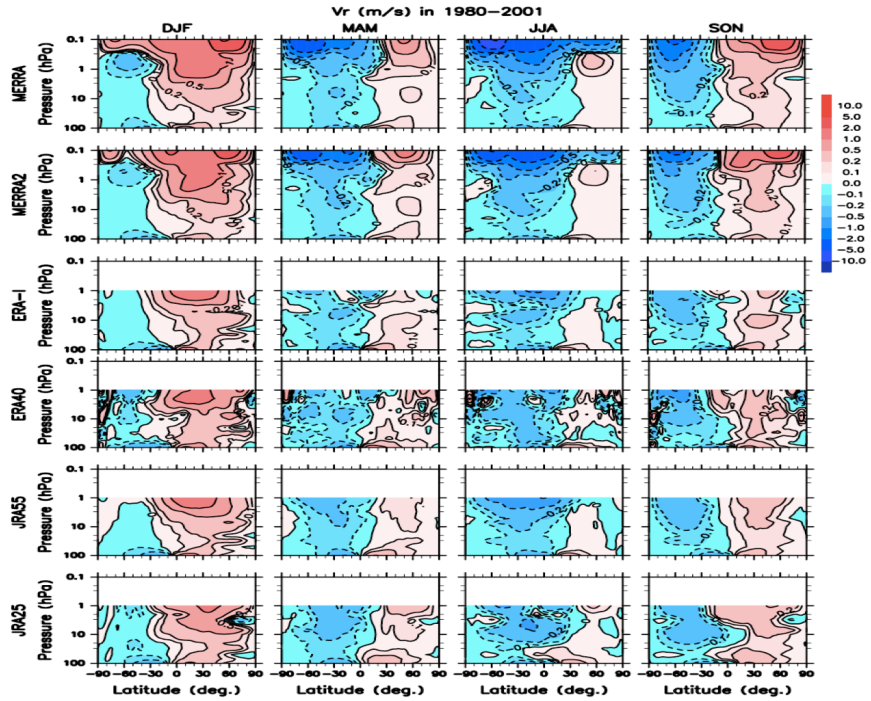

Figure 11.12: *Same as* ***Figure 11.7*** *except for the meridional component of the residual circulation. Contour intervals are logarithmic to emphasize small speeds.*

Eulerian-mean and residual-mean meridional wind differences from MERRA (Reanalyses minus MERRA) are shown in **Figure 11.13** and **Figure 11.14**, respectively. ERA-Interim, ERA-40, JRA-55, and JRA-25 have negative anomalies around 1 hPa in the SH winter midlatitudes (for JRA-25) or polar regions in both Eulerian-mean and residual-mean flows, which indicates that MERRA and MERRA-2 have stronger Eulerian-mean equatorward flow induced by the parameterized gravity wave drag. It may be because non-orographic gravity wave drag dominant in the SH is implemented only for MERRA and MERRA-2 (*e.g.*, *Fujiwara et al.*, 2017). On the other hand, the wind differences in ERA-Interim and JRA-55 are positive for Eulerian-mean but negative for residual-mean around 1 hPa in the NH winter polar region. This suggests that the Stokes drift induced by resolved planetary waves is different among ERA-Interim/JRA-55 and the other reanalyses. Eulerian-mean and residual-mean meridional wind differences in JRA-25 change signs around 3 hPa in the winter polar regions, which may be a result of the anomalous vertical temperature gradient there. Note also that 1 hPa is in the sponge layer for the lower top models, so that is another factor that might contribute to the differences.

In the winter mesosphere, MERRA has stronger (Eulerian-mean and residual-mean) poleward flow than MERRA-2. Such a difference between MERRA and MERRA-2 could be attributable to the difference of their gravity wave drag schemes (*i.e.*, non-orographic gravity wave source and intermittency of drag (*Molod et al.*, 2015)). Keep in mind that differences in the USLM also suffer from effects of the sponge layers and these may be different between high-top (*i.e.*, MERRA and MERRA-2) and low-top models. Since enhanced diffusion in the sponge layer is expected to be induced at a lower height in low-top models than in high-top models, pseudomomentum carried by resolved waves might be weaker in low-top models, which may lead to weaker Eulerian-mean meridional flow.

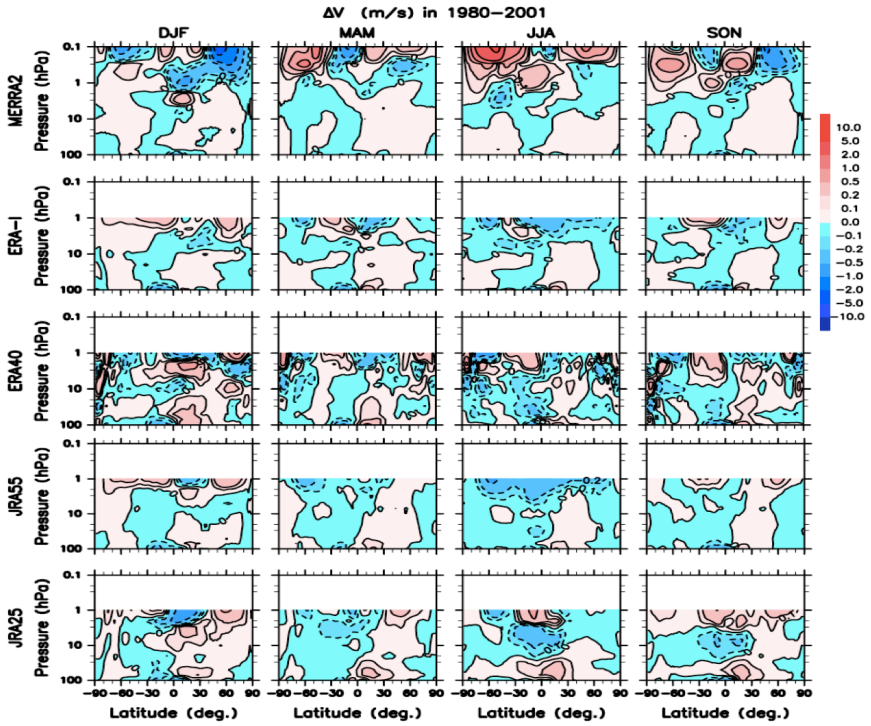

Figure 11.13: *Same as* ***Figure 11.8*** *except for meridional wind. Contour intervals are logarithmic to emphasize small differences.*

Figure 11.15 shows latitude-pressure sections of seasonal means of residual-mean vertical wind. A strong descending branch in the winter stratosphere can be seen in all the available reanalyses and is maximized around 75°N in the NH and around 50°S in the SH. Another weak descending branch is seen in the polar summer hemisphere below about 10 hPa, but only extends up to 1 hPa in JRA-25. A strong ascending branch in the stratosphere is maximized in the summer subtropics in all the available reanalyses. In the mesosphere from MERRA and MERRA-2, ascending and descending branches are maximized at the summer and winter poles, respectively. It should be noted that the residual-mean vertical and meridional winds in ERA-40 are much noisier than the other reanalysis especially in the polar regions. *Iwasaki et al.* (2009) reported a noisiness of residual-mean vertical wind in ERA-40 and attributed it to inconsistent dynamical noise induced by the assimilation process.

Residual-mean vertical wind differences from MERRA are shown in **Figure 11.16**. They clearly show that the differences in the winter polar stratosphere are positive, which indicates that the descending branch in the winter stratosphere is strongest in MERRA. In the mesosphere, the residual-mean vertical flow in MERRA is stronger than in MERRA-2 both at the summer and winter poles, which is consistent with the stronger summer-to-winter meridional flow in MERRA.

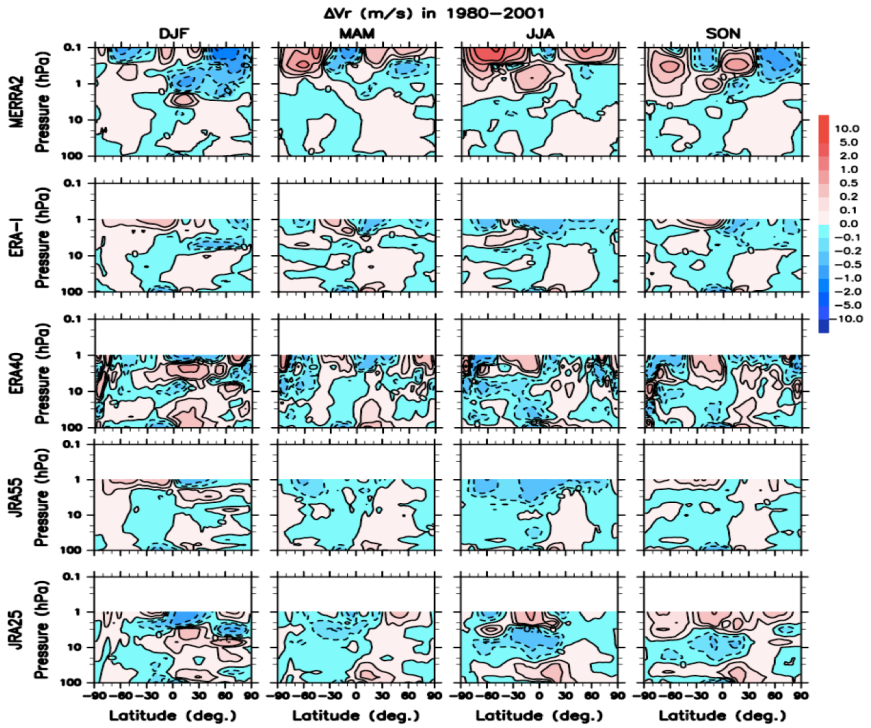

Figure 11.14: *Same as* ***Figure 11.8*** *except for the meridional component of the residual circulation. Contour intervals are logarithmic to emphasize small differences.*

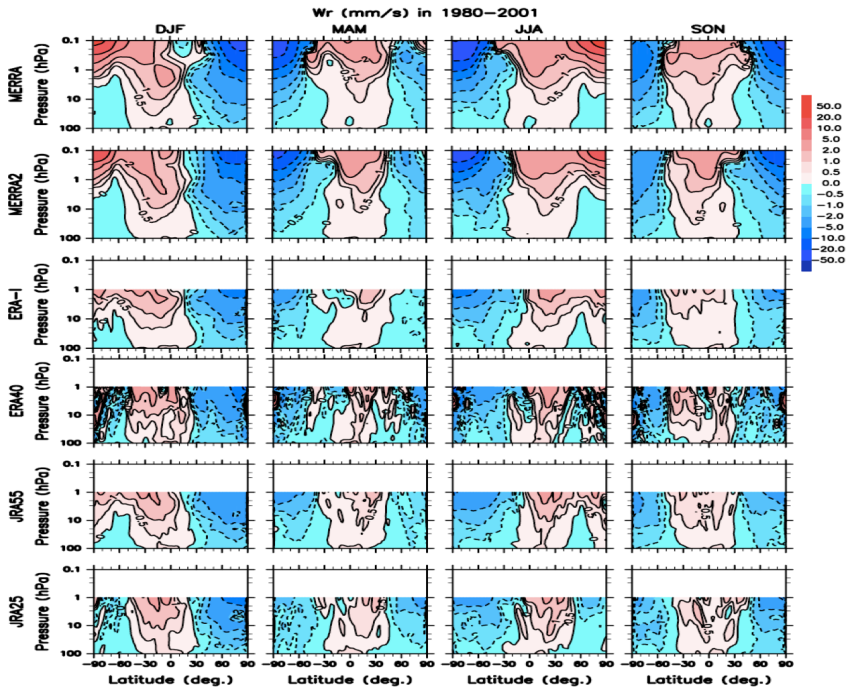

Figure 11.15: *Same as* ***Figure 11.7*** *except for the vertical component of the residual circulation. Contour intervals are logarithmic to emphasize small speeds.*

Comparisons of residual-mean meridional and vertical winds among the reanalyses do not conclude which reanalysis gives the most realistic and reliable meridional circulation in the stratosphere and mesosphere, but do inform the choice of which reanalysis dataset to use for different science applications. Noisy meridional and vertical winds in ERA-40 can cause larger dispersion of air parcels, which leads to shorter age of air and a weaker subtropical barrier in the stratosphere (*e.g.*, *Diallo et al.*, 2012; *Schoeberl et al.*, 2003). JRA-25 showed the upward extension of the descending branch in the summer stratosphere and anomalous flow around 3 hPa in the winter stratosphere, unlike the other reanalyses. The strongest descending branch in the winter stratosphere in MERRA may give shorter ages of air, similar to ERA-40. This result is consistent with results prepared for *Chapter 5* (not shown; *Thomas Birner, personal communication*, 2021), despite weak lower stratospheric tropical upwelling in MERRA (**Fig. 5.8**). *Abalos et al.* (2015) also reported differences among MERRA, ERA-Interim, and JRA-55. Thus, it is concluded that the newer MERRA-2, ERA-Interim, and JRA-55 reanalyses should be used to study transport by the residual circulation and that the older MERRA, ERA-40, and JRA-25 reanalyses are unsuitable for this purpose.

11.2.2 Annual cycles

In this section, we show annual cycles of zonal-mean temperature, Eulerian zonal and meridional winds, and Lagrangian TEM residual circulation velocities averaged over 1980 - 2001 for each of six reanalyses and their differences from MERRA.

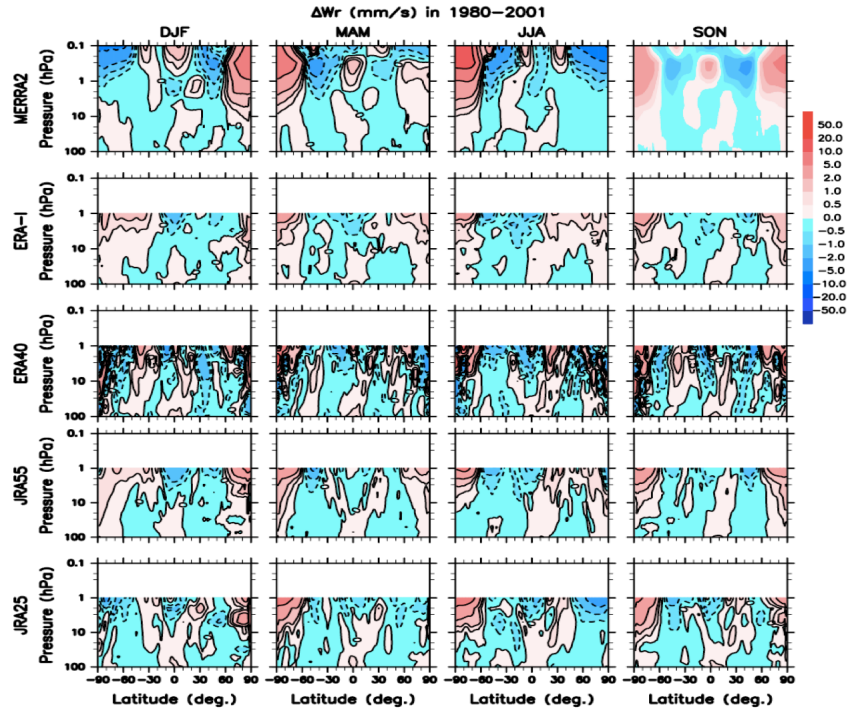

Figure 11.16: *Same as* ***Figure 11.8*** *except for the vertical component of the residual circulation. Contour intervals are logarithmic to emphasize small speeds.*

Figure 11.17 shows time-latitude sections of monthly zonal means of temperature at 1 hPa (left column) and their differences from MERRA (right column). The left column shows that the seasonal evolution of temperature near the stratopause (1 hPa) is similar among the reanalyses. While temperature is maximized in summer and minimized in the winter polar regions in both the NH and SH, its seasonal variation is smaller in the Tropics. Temperature differences from MERRA (right column) are larger in polar winter and spring and often exceed 4 K. The temperature in polar winter and spring is lower in MERRA-2, intermediate in MERRA, and higher in ERA-Interim, ERA-40, JRA-55, and JRA-25. The colder polar winter upper stratosphere in MERRA-2 is consistent with a slightly larger and longer-lived polar vortex, as will be shown in *Section 11.4.1*.

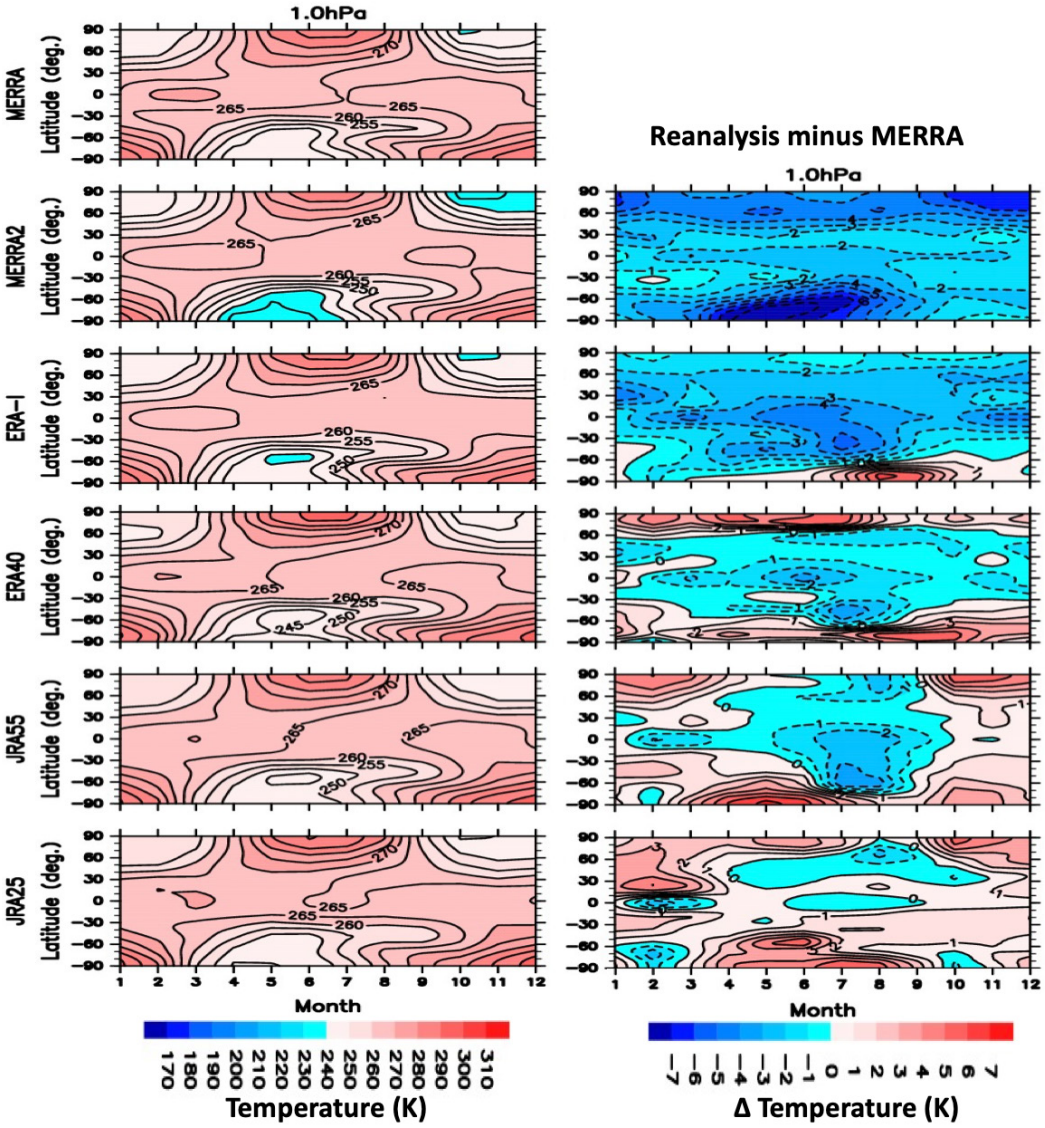

Figure 11.17: *Time-latitude sections of monthly-mean zonal-mean temperature (left column) at 1 hPa averaged over 1980 - 2001 from MERRA, MERRA-2, ERA-Interim, ERA-40, JRA-55, and JRA-25. Contour intervals are 5 K. The right column shows differences among each reanalysis on the left minus MERRA (top left). Contour interval is 1 K.*

Figure 11.18 shows time-latitude sections of monthly zonal mean zonal wind at 1 hPa (left column) and their differences from MERRA (right column). Overall, the evolution of the summer and winter zonal jets near the stratopause is in good agreement among the reanalyses (left column). Zonal wind differences from MERRA (right column) show that the Antarctic polar-night jet at this altitude is latitudinally broader in MERRA and MERRA-2 than in the other reanalyses. This is evidenced by the two negative regions on the poleward and equatorward flanks of the jet in May, June, and July in the ERA and JRA systems (though less clear in JRA-25). Unlike temperature (which showed largest differences at high latitudes), largest zonal wind differences occur in the Tropics and can be attributed to differences in the SAO among the reanalyses.

Time-latitude sections of monthly-means of Eulerian-mean and residual-mean meridional winds at 1 hPa and their differences from MERRA are shown in **Figure 11.19** and **Figure 11.20**, respectively. Although a couplet of Eulerian-mean equatorward and poleward flow is seen at 1 hPa in NH winter in all the available reanalyses (left column of **Figure 11.19**), it is stronger in MERRA than in the other reanalyses (right column of **Figure 11.19**). This difference is mostly confined between 0° and 30°N in February and may be associated with differences in the SAO's secondary circulation. A similar feature is partially seen in SH winter, but much weaker than in the NH. On the other hand, the residual-mean meridional flow in winter is always poleward in both the NH and SH (left column of **Figure 11.20**). While the poleward residual-mean flow in NH is maximized from 0° - 30°N in December and January in all the reanalyses, the latitude and month of the strongest poleward residual-mean flow in the SH are variable among the reanalyses.

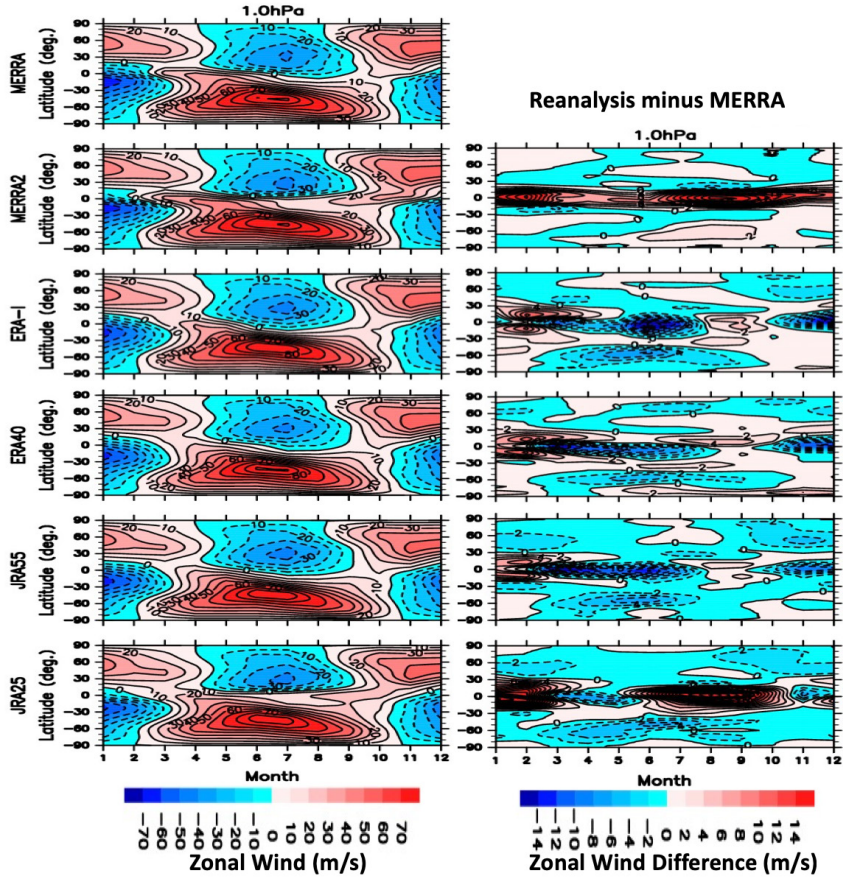

Figure 11.18: *Same as* ***Figure 11.17*** *except for zonal wind. Contour intervals are 10 m s^{-1} for panels in the left column and 2 m s^{-1} for panels in the right column.*

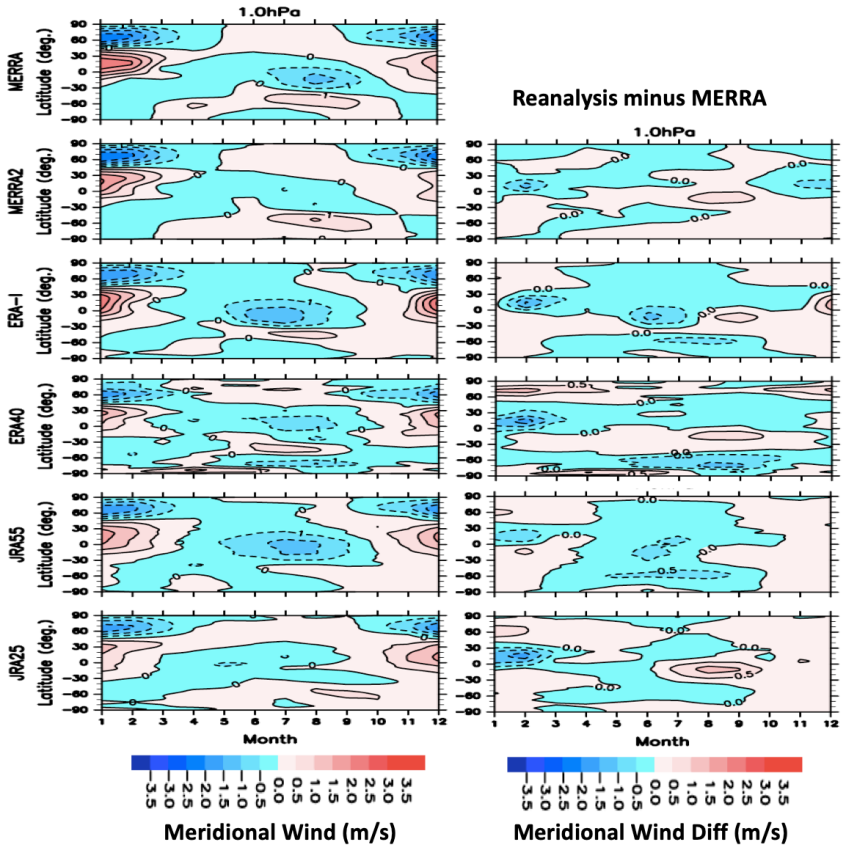

Figure 11.19: *Same as* ***Figure 11.17*** *except for meridional wind. Contour intervals are 0.5 m s^{-1} for all panels.*

Eulerian-mean and residual-mean meridional wind differences from MERRA are basically similar, so that the variable feature of residual-mean flow in SH could be attributable to the difference of parameterized gravity wave drag among the reanalyses as mentioned in *Section 11.2.1.*

Figure 11.21 shows time-latitude sections of monthly means of residual-mean vertical wind at 1 hPa (left column) and their differences from MERRA (right column). A strong descending branch is seen in the winter polar regions in all the reanalyses, but it is too noisy in ERA-40 as mentioned in *Section 11.2.1.* The descending branch in polar winter is strongest in MERRA. It indicates that the temperature differences among MERRA and the other reanalyses (except for MERRA-2) shown in **Figure 11.17** are not due to the difference of dynamical heating induced by the downward flow but more likely due to the difference in the radiation schemes and the assimilation process among the reanalyses.

Seasonal variations of residual-mean meridional wind in 30°-60°N and 30°-60°S at 1 hPa are shown in **Figure 11.22**. Poleward flow is maximized in December and January in NH and in August in SH (except for ERA-40), which is nearly coincident with the maxima of residual-mean downward flow from 60°-90°N and from 60°-90°S, respectively, at 1 hPa (see below). Seasonal variations of the residual-mean meridional wind are larger in NH than in SH because of the larger planetary wave activity in the NH winter. The residual-mean meridional flow in summer becomes equatorward both in NH and SH only for ERA-Interim and JRA-55, which was also seen in **Figure 11.20**. It looks consistent with the strongest upward residual flow in summer for ERA-Interim and JRA-55 as will be shown below. Since most of the planetary and orographic gravity waves are prohibited to propagate upward between the westerlies in the troposphere and the summer easterlies in the stratosphere because of the critical layer filtering, the differences in the meridional flow around the summer stratopause are likely due to the difference of non-orographic gravity wave drag among the reanalyses.

Seasonal variations in the residual-mean vertical velocities from 60°-90°N and from 60°-90°S at 1 hPa are presented in **Figure 11.23**. At this altitude the residual-mean downward flow in polar winter is maximized in December and January in NH and in August in SH (except for ERA-40). The different seasonal variations between the NH and SH (*i.e.*, not a 6-month shift) are consistent with their different seasonal marches of planetary wave activity (*e.g.*, *Shiotani and Hirota*, 1985). It is worth noting that seasonal marches of downward residual-mean flow at 10 hPa are delayed by 1 - 2 months compared to at the 1 hPa altitude level (not shown).

Turning specifically to the deep Tropics, the annual march of zonal-mean zonal winds and their variability are shown in **Figure 11.24**. Comparing four reanalyses to MLS gradient winds (panel **a**) show good agreement between the reanalyses and the observations time-averaged annual cycle of zonal winds from 10°S-10°N. The year-round westerly bias in MERRA-2 is apparent. While the mean annual cycle in zonal wind (panel **a**) in each reanalysis is similar the interannual variability (panel **b**) is quite different among the reanalyses. Future studies need to document and understand the cause of these year-to-year variations. In panel (**c**), we demonstrate that the standard deviation among the four reanalyses varies as a function of the time of year; it is smaller (6 - 7 m s^{-1}) during the westerly phase of the SAO around the equinoxes and larger (8 - 9 m s^{-1}) during the easterly phases in solstice seasons. Separating the tropical regions by hemisphere (10°-20°N and 10°-20°S) reveals a clear annual cycle. Namely, the variability among the reanalyses is twice as large (5 - 6 m s^{-1}) in the winter than in summer (2 - 3 m s^{-1}) (not shown).

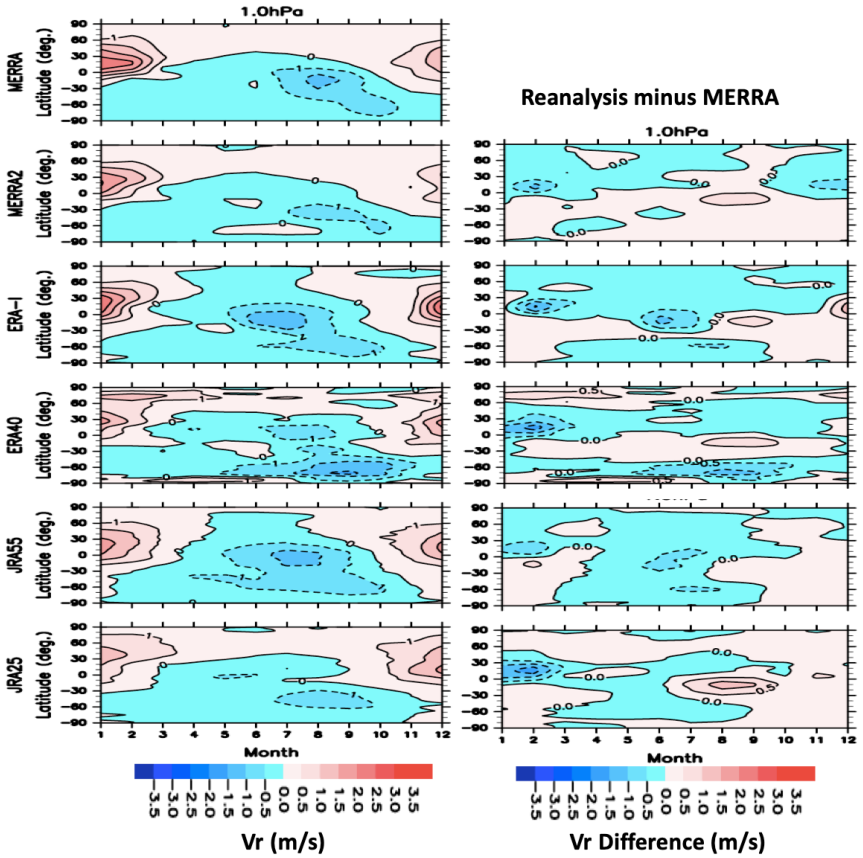

Figure 11.20: *Same as* ***Figure 11.17*** *except for the meridional component of the residual circulation. Contour intervals are 0.5 m s^{-1} for all panels.*

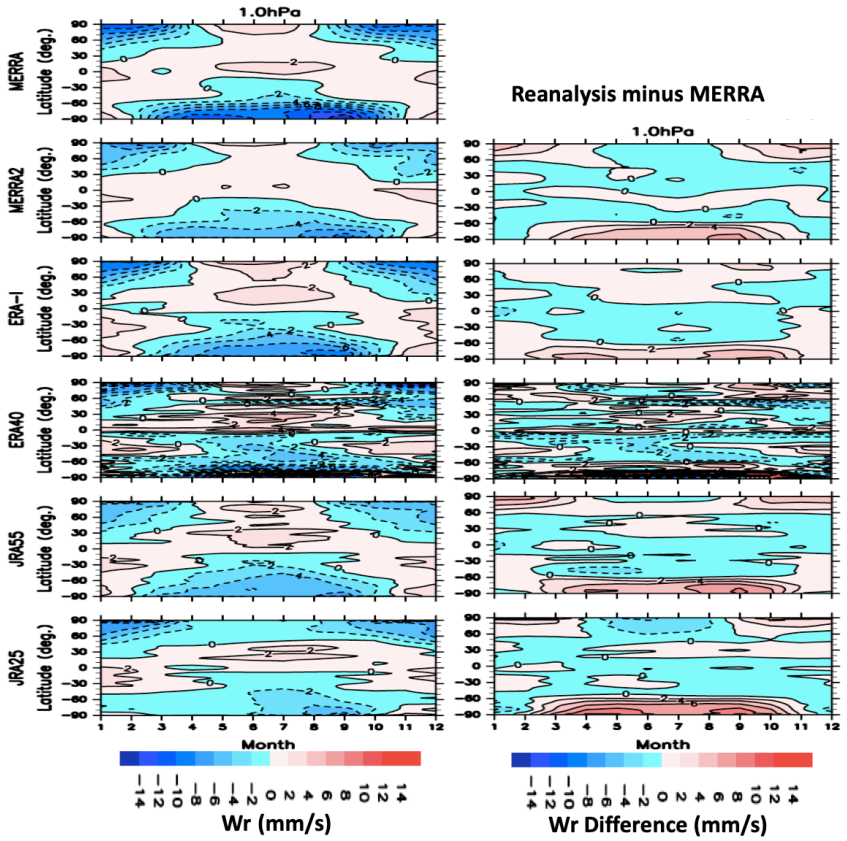

Figure 11.21: *Same as* ***Figure 11.17*** *except for the vertical component of the residual circulation. Contour intervals are 2 mm s^{-1} for all panels.*

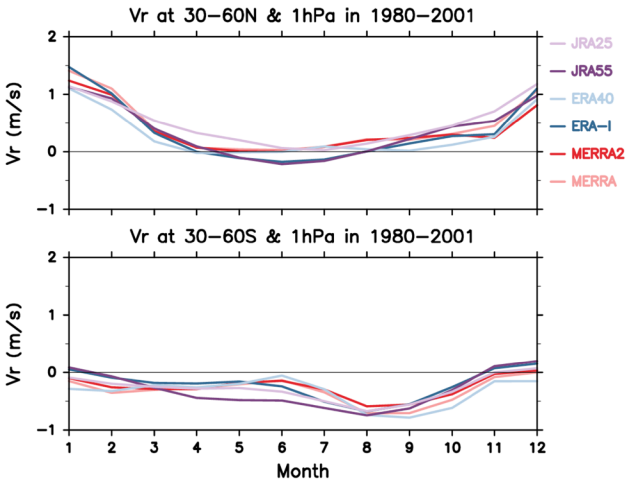

Figure 11.22: *Line plot showing the annual cycles of the meridional component of the residual circulation from 30°-60° latitude in the a) NH and b) SH at 1 hPa in 6 reanalysis datasets.*

Recall that temperature differences are large at all latitudes and increase with increasing altitude (shown in **Figure 11.4**). Here we explore whether those differences depend on the annual cycle. **Figure 11.25** depicts the annual cycle of zonal mean temperature at 60°N (top panels) and 60° S (bottom panels) at the stratopause (left panels) and in the lower mesosphere (right panels). There is excellent agreement among the reanalyses at 1 hPa (with the exception of CFSR which is ~ 10 K warmer in the winter). At this altitude the differences range from 3 - 8 K and are smallest in early winter. The right column shows that mid-latitude temperature differences grow rapidly in the lower mesosphere. At 0.3 hPa there are 10 - 15 K differences among the reanalyses year-round, with larger differences in the SH (bottom right) than in the NH (top right). It is not surprising that MERRA-2 (red contour) is in closest agreement with MLS (black contour) since the time period shown here is 2005 - 2015

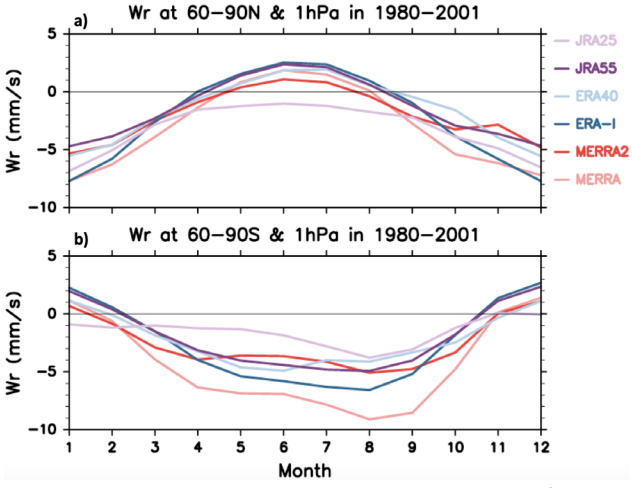

Figure 11.23: *Line plot showing the annual cycles of the vertical component of the residual circulation from 60°-90° latitude in the a) NH and b) SH at 1 hPa in 6 reanalysis datasets.*

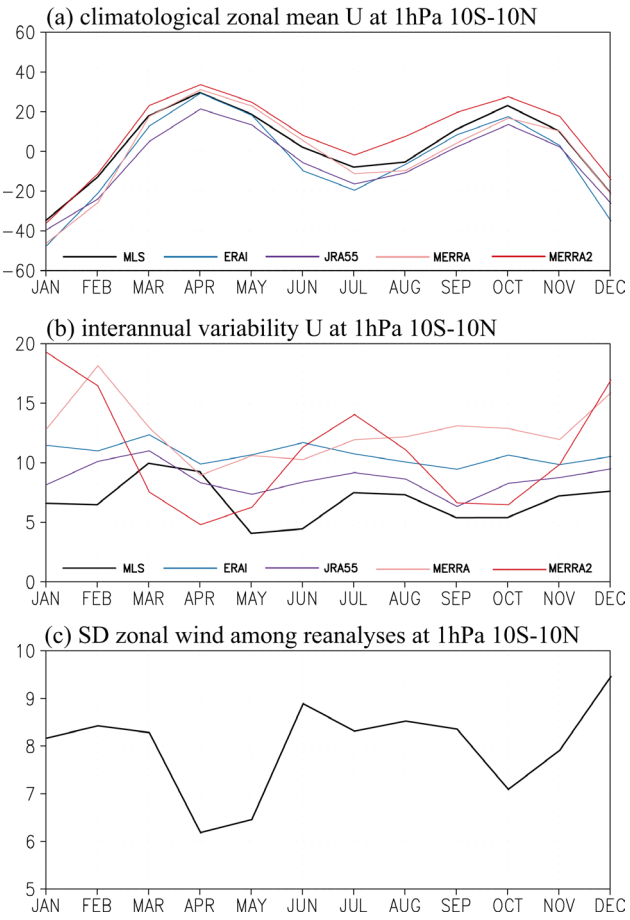

Figure 11.24: *Line plot of the 10° S - 10° N climatological annual marches of (a) zonal-mean zonal winds at 1 hPa for 1980 - 2010 for five reanalyses (color) and for the September 2004 to August 2014 average MLS gradient winds (black), (b) zonal wind interannual variability within each reanalysis dataset, and (c) zonal wind standard deviations showing variability among the five reanalyses. Wind is in m s^{-1}. Figures 11.24a and 11.24b are modified from Kawatani et al. (2020).*

when MERRA-2 assimilates MLS temperature data. Thus we conclude that reanalysis temperatures are suspect at 0.3 hPa in general, but are perhaps more believable in MERRA-2 because MERRA-2 assimilates some data at these altitudes.

11.2.3 Long-term variability

The reanalyses also exhibit long-term variability due to different climate forcing mechanisms. A multi-linear regression (MLR) analysis has been performed to characterize USLM variability associated with the ENSO, the QBO, the 11-year solar cycle, and volcanic eruptions (while taking into account any trend associated with GHG changes – see *Crooks and Gray*, 2005). Results from the following datasets are shown and discussed here: JRA-55, MERRA-2 and ERA-Interim, since these are the most up-to-date reanalysis products with available data on several pressure levels above 1 hPa.

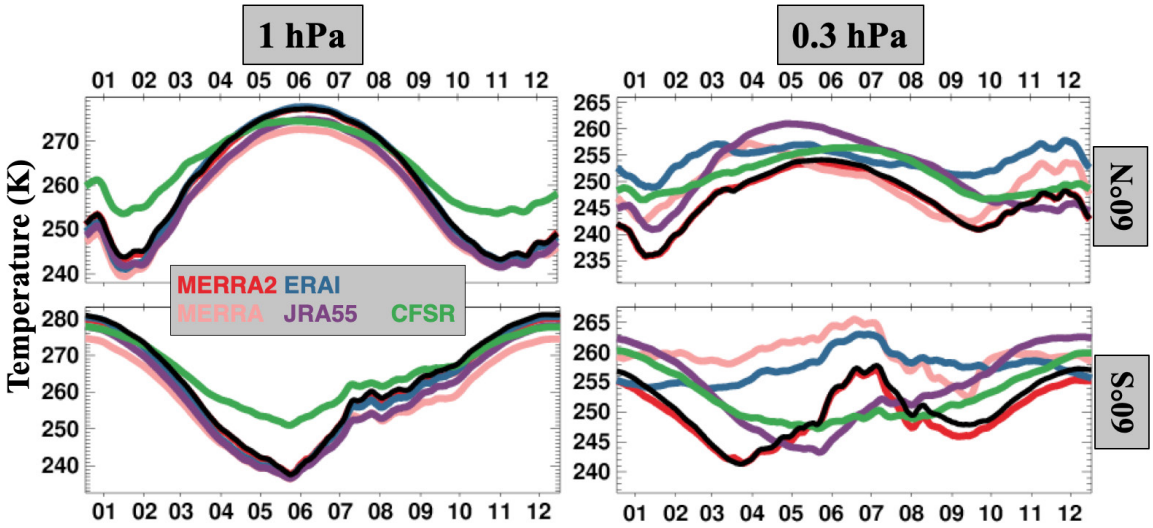

Figure 11.25: *Line plots of multi-year (2005 - 2015) annual cycles of temperature at 60° N (top) and 60° S (bottom) at 1 hPa (left) and 0.3 hPa (right) in five reanalyses (MERRA, MERRA-2, ERA-Interim, JRA-55, and CFSR) and MLS (black).*

Further comparisons including earlier reanalysis products and those that do not fully resolve the USLM can be found in *Mitchell et al.* (2015).

MLR Methodology and Indices

The ENSO index employed was the Nino3.4 time-series (5°S - 5°N; 120°W - 170°W) from the Extended Reconstructed Sea Surface Temperature (ERSST) dataset (*Smith and Reynolds*, 2003; **http://www.cpc.ncep.noaa.gov/data/indices/**). The volcanic eruption index was derived from the *Sato et al.* (1993) aerosol index. The 11-year solar cycle index was derived from an updated version of the Naval Research Laboratory model for Solar Spectral Irradiance (NRLSSI) time-series of total solar irradiance (*Wang et al.*, 2005) available at **http://solarisheppa.geomar.de/solarisheppa/cmip5**. QBO variability was expressed by a combination of two separate indices, comprised of the principal components of the 1st two terms from an Empirical Orthogonal Function (EOF) analysis of tropical winds averaged over the region 5°S - 5°N and 100 - 10 hPa (for more details see *Chapter 9*), in order to capture the time-variation at different heights associated with the gradually descending QBO phase. An autoregressive noise term was included (see *Crooks and Gray*, 2005) and a Student's t-test was employed to determine the probability that the regression coefficients are significantly different from the noise (light/dark shaded regions in all figures denote statistical significance at the 95 % / 99 % level). The regression coefficients have been re-scaled in all figures to show the typical maximum response *e.g.*, between opposite QBO/ENSO phases or between periods of solar maximum-minimum conditions. For further details see *Mitchell et al.* (2015).

Temperature and Zonal Wind Variability in the USLM

Figure 11.26 and Figure **11.27** show variability in annual-mean, zonally-averaged temperatures and zonal winds associated with ENSO, volcanic eruptions, QBO and 11-year solar cycle covering the period 1979-2009 (1980 - 2009 in the case of MERRA-2). Responses at high latitudes arise primarily from the winter season in each hemisphere (particularly in the case of the zonal winds) and can therefore be interpreted as the winter response.

As expected, the impact of ENSO on tropical tropospheric temperatures and winds (top row) is clearly evident and highly statistically significant. There is additionally a highly statistically significant influence of ENSO in the USLM temperatures, particularly in the mid-to-high latitudes of the NH. Anomalous warming of up to 5 K is present in the NH polar US peaking around 10 hPa with cooling of up to 5 K in the LM above ~ 1 hPa, together with a corresponding (but less significant) easterly zonal wind anomaly in both US and LM, indicating a more disturbed winter circulation. These signals are consistent among the reanalyses, although there are some variations in latitudinal extent and amplitude of the LM temperature response among the datasets. These results support previous observational and modeling studies (*e.g.*, *Garcia-Herrera et al.*, 2006) that suggest the presence of increased wave forcing from the troposphere and hence a more disturbed stratosphere/mesosphere winter circulation associated with warm ENSO events.

The zonal wind and temperature QBO anomalies (3rd row; only variability associated with one of the EOFs is shown for brevity – see also *Chapter 9*) extend upward into the tropical USLM with the familiar pancake-like structure in the vertical (*Pascoe et al.*, 2005). The equatorial QBO temperature anomalies reach 3 - 4 K near ~ 3 hPa and the USLM zonal wind anomalies, while not as strong as in the lower stratosphere nevertheless exceed 5 m s^{-1}. The temperature anomalies of opposite sign in the subtropics associated with local QBO-induced secondary circulations extend to around 60° N.

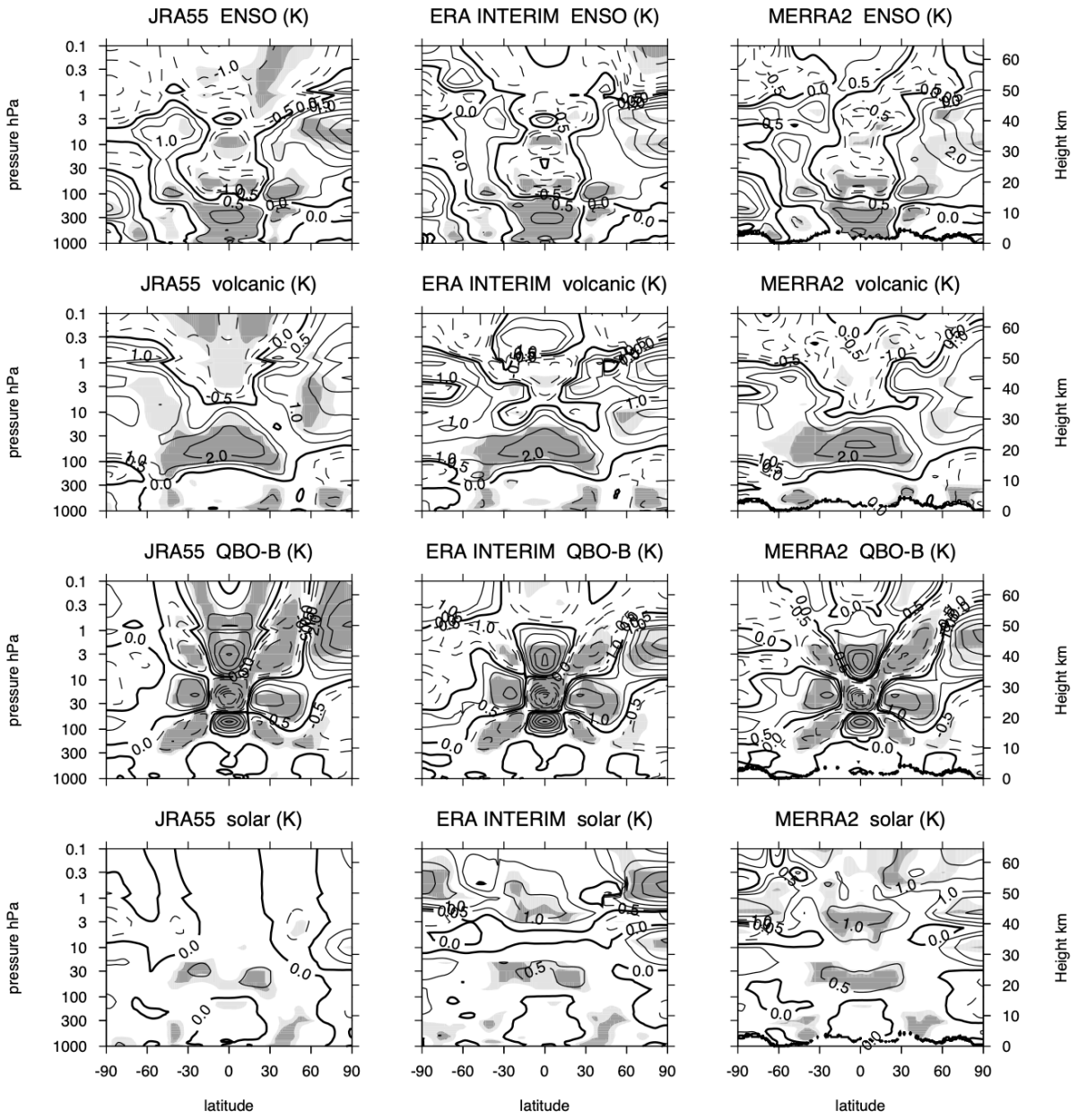

Figure 11.26: *The annual-mean temperature variability (K) associated with ENSO (top row), volcanic (2nd row), QBO (3rd row) and 11-year solar cycle (bottom row) for each of the 3 reanalysis datasets JRA-55, ERA-Interim and MERRA-2 from a multiple linear regression analysis. The regression coefficients have been multiplied to show the maximum temperature difference e.g., El Niño minus La Niña, QBO west minus east phase and Smax minus Smin. Contour intervals are 0.5, 1, 2, 3, 4, 5 K; the thick solid line denotes the zero contour, solid (dashed) contours denote positive (negative) responses. Light and dark gray shading indicates statistical significance at the 95 % and 99 % levels, respectively. Taken from Mitchell et al. (2015).*

While a mesospheric equatorial QBO has previously been identified (see *e.g.*, *Baldwin et al.*, 2001) it is not well characterized due to lack of observations and the reanalyses reflect this uncertainty, showing considerable variation in the structure, sign and statistical significance of the QBO signal in that region. At high latitudes there is a statistically significant response with warmer temperatures above ~3 hPa overlying cool anomalies and a stronger (westerly) zonal wind anomaly associated with QBO westerlies at 30 hPa, in good agreement with the Holton-Tan relationship (*Anstey and Shepherd*, 2014; *Holton and Tan*, 1982). Further discussion of the QBO response is provided in *Chapter 9*.

The 11-year solar cycle signal (bottom row) shows considerable differences among the reanalysis datasets. The primary radiative response to the 11-year solar cycle is in the mid-upper equatorial stratosphere, associated with both increased UV irradiance and ozone production (*Gray et al.*, 2010). Both ERA-Interim and MERRA-2 show a statistically significant warm anomaly of ~1.25 K from solar maximum to solar minimum (Smax-Smin) centered over the equatorial region near 1 hPa with a corresponding westerly (thermal) wind anomaly mainly in the subtropics. JRA-55 on the other hand shows a very weak temperature response with no statistical significance although the wind response agrees well with the other two reanalyses.

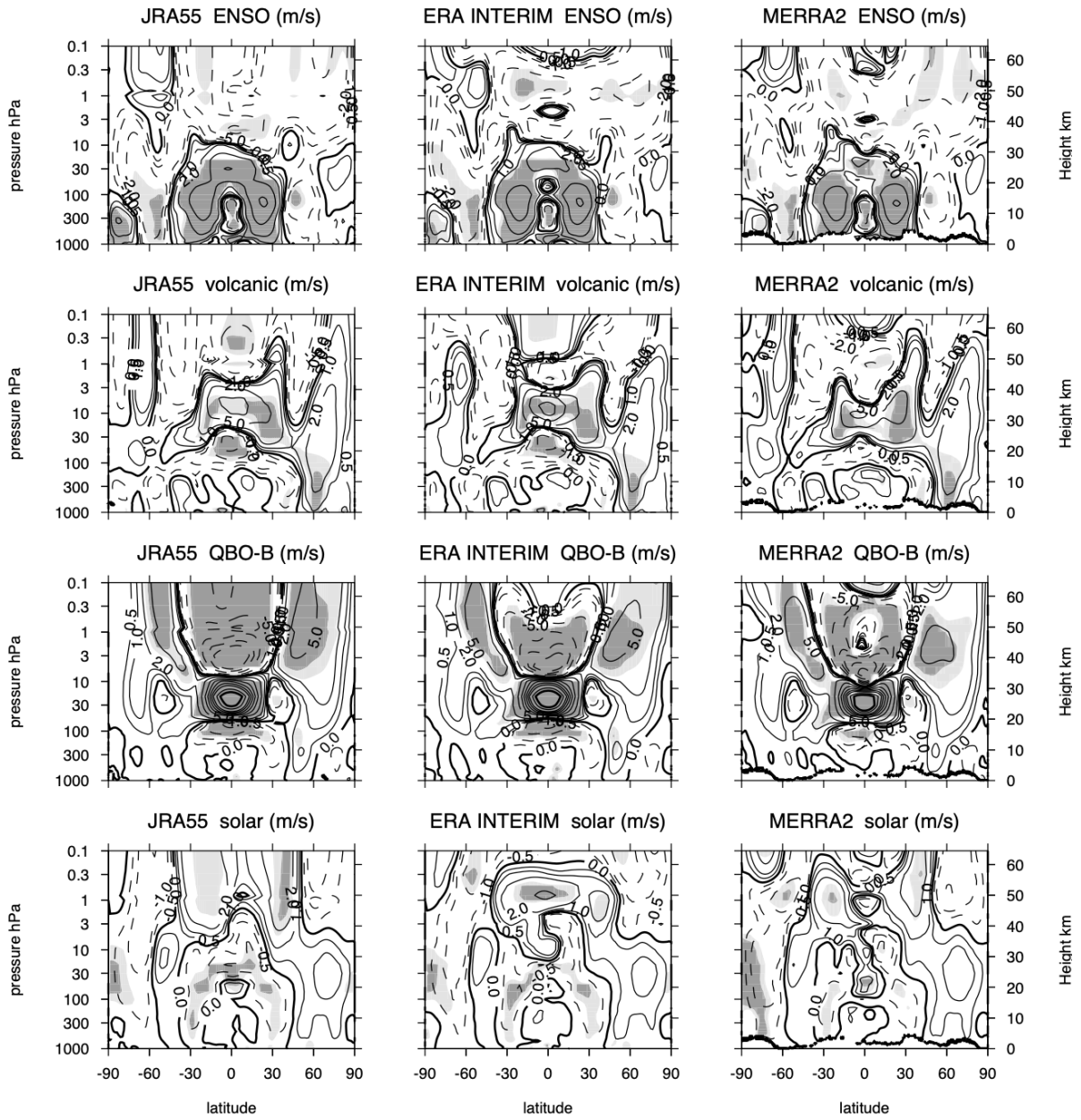

Figure 11.27: *The annual-mean zonal wind variability (ms-1) associated with ENSO (top row), volcanic (2nd row), QBO (3rd row) and 11-year solar cycle (bottom row) for each of the 3 reanalysis datasets JRA-55, ERA-Interim and MERRA-2 from a multiple linear regression analysis. The regression coefficients have been multiplied to show the maximum temperature difference e.g., El Niño minus La Niña, QBO west minus east phase and Smax minus Smin. Contour intervals are 1, 2, 3, 5, 10, 15, 20, 30, 40, 50 m s^{-1}; the thick solid line denotes the zero contour; solid (dashed) contours denote positive (negative) responses. Light and dark gray shading indicates statistical significance at the 95 % and 99 % levels, respectively. Taken from Mitchell et al. (2015).*

This inconsistency in the USLM solar response among the reanalysis datasets is likely due to a combination of poor vertical resolution of the available satellite data and the difficulties of extracting an 11-year signal from datasets that assimilate observations from relatively short-lived satellite instruments. This lack of agreement is in contrast to the lower stratospheric solar response which is much more consistent between the reanalyses, presumably because this region is covered extensively by radiosonde observations. Further investigation of the weak USLM solar cycle response in JRA-55 (*Stergios Misios, personal communication*, 2018) indicates that this is primarily because of a difference in timing of the peak solar response in JRA-55: the maximum response (which is statistically significant) occurs a year or so leading up to solar maximum and is therefore not captured in **Figure 11.26** since no lag/lead has been applied to the regression analysis. This highlights possible differences in the treatment of solar irradiance changes in the underlying reanalysis model and also the importance of careful examination of lead/lag responses when performing regression analysis of the solar signal; results may also be sensitive to the solar index employed in the analysis (*e.g.*, total solar irradiance, sunspot number, solar magnetic flux) since the different solar flux proxies show some variation in their timing.

11.3 Tropical Dynamics

11.3.1 Semi-Annual Oscillation

The SAO is a reversal of zonal winds from easterly to westerly at both the stratopause and at the mesopause (with the phase reversed) with a period of approximately six months (*Garcia et al.*, 1997). First discovered by Reed in 1962, the SAO is driven by a combination of planetary and gravity wave forcing as well as mean meridional advection (*Hamilton*, 1998), and exerts control over thermal and chemical transport processes at both the lower and upper regions of the USLM. It is crucial to examine this and other tropical processes in this chapter because differences in the reanalyses are largest in the tropical USLM. (See *Kawatani et al.* (2020) for the detailed reanalysis comparisons.)

Semiannual components are extracted from monthly mean data by applying an Ormsby time filter and then calculating the amplitude ($\sqrt{2} \times \sqrt{\sum U_{SAO}^2 / N}$, where USAO indicates SAO components of the zonal wind). **Figure 11.28** shows that the SAO in temperature is almost symmetric with respect to the Equator, and that the amplitude of the temperature SAO is larger in ERA-Interim compared to the other reanalyses at the tropical stratopause. In general, the structure of the SAO below 1 hPa is similar in the reanalyses, while differences among the reanalyses become large above that level. The SAO components in the mesosphere are very small in JRA-55 and MERRA-2. In order to see the effects of satellite observations, results from JRA-55C (in which only conventional data were assimilated; panel **f**) are shown alongside JRA-55 (panel **e**). The SAO amplitude in JRA-55C is severely underestimated both in the stratosphere and mesosphere. These results make clear that the physical parameterizations in the JRA-55 model apparently cannot simulate an SAO on their own.

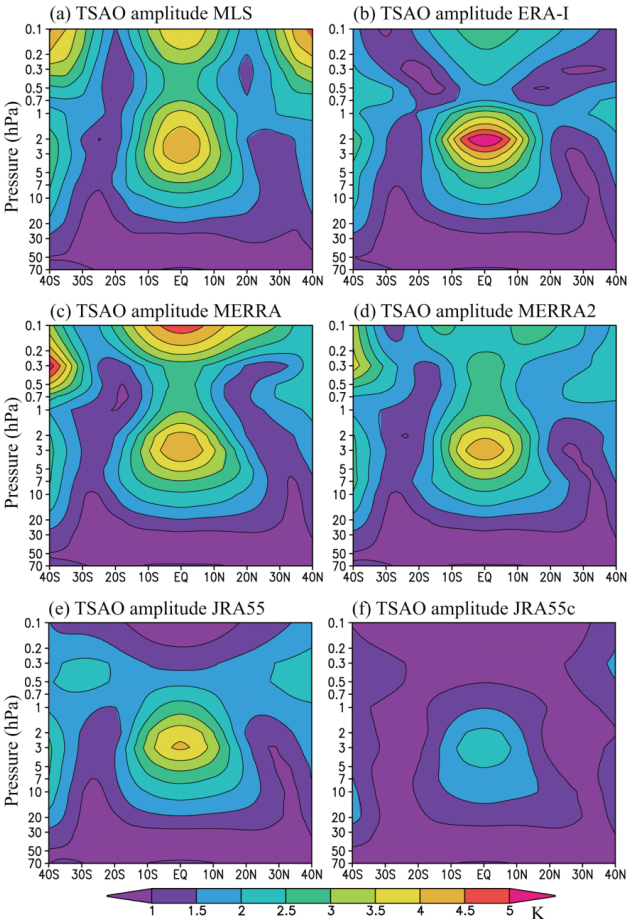

Figure 11.28: *Latitude-altitude distributions of the zonal mean temperature SAO component averaged over 2004 - 2014 for MLS observations (upper left) and 1980 - 2012 for the reanalyses. Temperature is in degrees K. Note that JRA-55C is a reanalysis without assimilated satellite observations. Modified from Kawatani et al. (2020).*

Turning to the SAO in winds, **Figure 11.29** shows that the zonal-wind SAO is asymmetric with respect to the Equator; the maximum amplitude exists from 10° - 20° S, which is consistent with earlier rocketsonde observations (*e.g.*, *Hopkins*, 1975). The above asymmetry is likely due to asymmetric components in the temperature SAO. The amplitude of the zonal-wind SAO is larger in ERA-Interim and MERRA compared to MERRA-2, the JRA model versions, and the MLS observations.

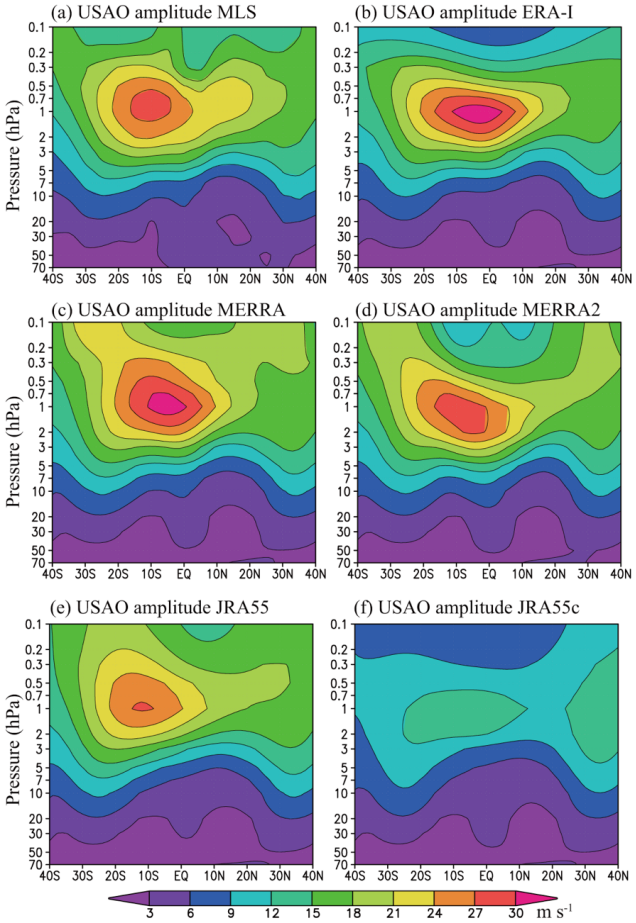

Figure 11.29: *Same as* ***Figure 11.28*** *but for the zonal mean zonal-wind SAO component in m s^{-1}. Modified from Kawatani et al. (2020).*

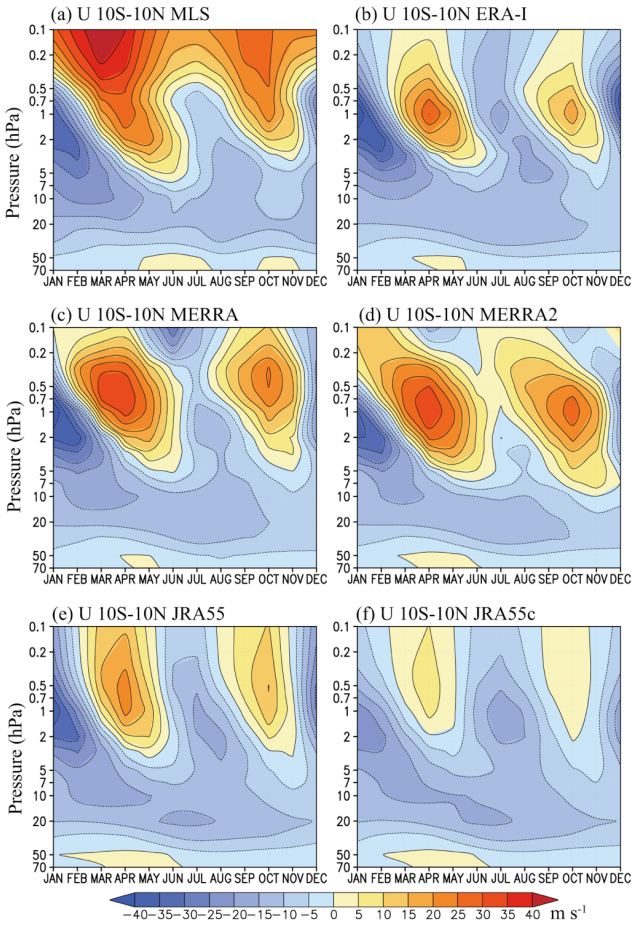

Figure 11.30: *Time-height sections of climatological zonal-mean zonal winds (in m s^{-1}) averaged between 10°S and 10°N for MLS derived gradient winds (top left) and five reanalyses. Modified from Kawatani et al. (2020).*

These results are consistent with *Das et al.* (2016) (see their **Figure 7d**) who showed the amplitude of the SAO to be larger in ERA-Interim and MERRA compared to rocket observations. Similarly, *Kishore Kumar et al.* (2015) (see their **Figure 4**) reported 30% larger SAO amplitudes near the stratopause in MERRA compared to rocketsonde winds. These results suggest that the JRA-55 model requires upper-air data assimilation to capture the SAO. Another possible factor for the weak winds in JRA-55C is the sponge layer; the forecast model might generate winds even if there were no observations.

Time-height sections of the zonal-mean zonal wind in the deep Tropics (**Figure 11.30**) reveal large differences between the reanalyses and the observations in the mesosphere. MLS-derived gradient winds (upper left panel) are strong westerly year-round above 0.5 hPa. This wind regime is consistent with the rocketsonde climatology of tropical zonal winds at Thumba (8.5°N, 77°E) in the lower mesosphere shown by *Kishore Kumar et al.* (2015; see their **Figure 1**, upper left panel). Persistent westerlies are also consistent with SABER observations (*Smith et al.*, 2017; see their **Figure 1**). However, the zonal wind climatology based on the Horizontal Wind Model 07 (also shown by *Kishore Kumar et al.*, 2015; see their **Figure 1**, lower left panel) indicates the presence of summer easterlies in the tropical lower mesosphere at Thumba. The overall features in the reanalyses are similar to the MLS and rocketsonde observations between 5 hPa and 0.5 hPa but diverge at higher altitudes. In ERA-Interim and JRA-55 above 0.5 hPa the onset of the westerlies occurs at the same time instead of progressing downward as in MLS, MERRA, and MERRA-2. This is probably due to the influence of sponge layers in the models, where equatorial waves cannot propagate upward. In MERRA-2, the downward progression of zonal wind anomalies is more pronounced such that the easterlies in the lower mesosphere occur during the equinoxes instead of during the solstices. As expected, differences between JRA-55 and JRA-55C are relatively small up to ~10 hPa, while they become large above this level. The JRA-55C results make clear the need to assimilate satellite data in the equatorial USLM where relatively small-scale gravity waves and Kelvin waves are dominant. Users are advised that JRA-55C cannot be used in the USLM.

New results from the ERA5 also shed light on the performance of different reanalyses with regard to the SAO. As seen in **Figure 11.31**, while the zonal winds are in excellent agreement between ERA-Interim and ERA5 in the QBO altitude regime, the mesopause SAO in ERA5 is substantially different from the same feature in ERA-Interim (see *Shepherd et al.* (2018) and references therein). In the region from 0.5 hPa to 0.1 hPa, ERA5 westerlies are at least 30 m s^{-1} larger than in ERA-Interim; ERA5 lacks descending solstitial easterlies in this region as well. The strong and persistent mesospheric jet in ERA5 is evident in both the average annual cycle of the zonal winds (bottom panels) and in individual years (top panels). Researchers at ECMWF note that the "predominance of westerlies in ERA5 is related to the spurious equatorial mesospheric jet that occurs in CY41R2 of the IFS and which peaks in the transition seasons" (*Shepherd et al.*, 2018; *Polichtchouk et al.*, 2017).

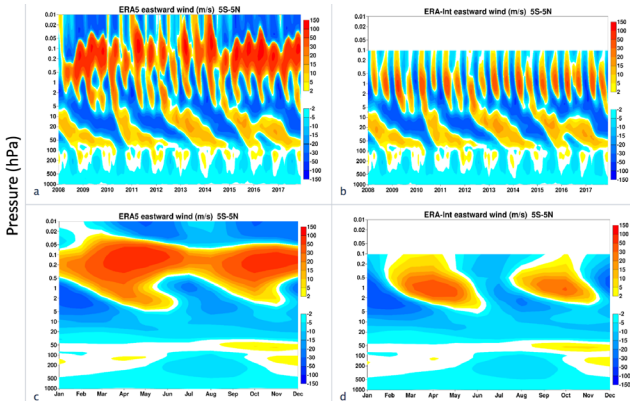

Figure 11.31: *Time-altitude section of monthly mean zonal mean zonal wind averaged from 5°S-5°N in ERA5 (left) and ERA-Interim (right). Top panels show interannual variability from 2008 to 2017. Bottom panels show the average annual cycle averaged between 2008 and 2017. Units are m s^{-1}. The vertical coordinate is the reference pressure of the model levels. Taken from* ***https://confluence.ecmwf.int/display/CKB/ERA5%3A+The+QBO+and+SAO****. ©Copernicus Climate Change Service/ECMWF. Used with permission.*

While this behavior diverges from the other reanalyses presented here, it is consistent with the year-round westerly winds observed by rocketsondes and derived using satellite temperatures. ERA5 validation efforts should accompany the use of this (and any) reanalysis dataset with regard to tropical mesospheric dynamics.

11.3.2 Middle-atmosphere Hadley circulation

The Hadley cell circulation, most often associated with tropospheric dynamics, extends into the USLM. By way of explanation, a brief synopsis of the theory explaining the middle-atmosphere Hadley circulation is given below.

The residual-mean meridional circulation ($\equiv(0, \bar{v}^*, \bar{w}^*)$) satisfies the following zonal momentum equation in the transformed Eulerian-mean formalism:

$$\bar{u}_t + \bar{v}^*\left[(a\cos\phi)^{-1}(\bar{u}\cos\phi)_\phi - f\right] + \bar{w}^*\bar{u}_z = (\rho_0 a\cos\phi)^{-1}\nabla\cdot\boldsymbol{F} + \bar{X} \quad (11.1),$$

where a is the Earth's radius, ϕ the latitude, f the Coriolis parameter, $\bar{X}$ the zonal-mean unresolved mechanical forcing, and $\nabla\cdot\boldsymbol{F}$ the Eliassen-Palm (E-P) flux divergence (*cf.*, *Andrews et al.*, 1987). Its alternative form can be expressed using the zonal-mean absolute angular momentum ($M \equiv a\cos\phi(\bar{u} + \Omega a\cos\phi)$, where Ω is the Earth's rotation rate) as

$$M_t + \bar{v}^* a^{-1} M_\phi + \bar{w}^* M_z = \rho_0{}^{-1}\nabla\cdot\boldsymbol{F} + \bar{X}a\cos\phi \quad (11.2).$$

This equation indicates that the residual mean flow cannot cross isopleths of M without non-zero E-P flux divergence under the assumption of $M_t = 0$ and $\bar{X} = 0$. This situation occurs in the extratropics for the monthly-mean (or longer timescales) residual circulation (which is driven by the E-P flux divergence due primarily to Rossby waves and explicitly resolved gravity waves). On the other hand, the steady state assumption does not hold in the Tropics because it takes a long time to achieve thermal wind balance due to the small Coriolis parameter there. This allows a meridional Hadley-type circulation to be thermally driven in the Tropics if there is an imbalance between the radiative equilibrium temperatures and the zonal wind distributions This circulation cancels the meridional gradients in ozone heating that form across the Equator in the USLM and those gradients are particularly large during the solstice seasons (*Semeniuk and Shepherd*, 2001a; 2001b; *Dunkerton*, 1989). Such a thermally-driven meridional circulation is referred to here as the middle-atmosphere or stratopause Hadley circulation.

The upwelling branch of the residual-mean meridional circulation in the tropical upper stratosphere and lower mesosphere is maximized in the summer subtropics (*e.g.*, *Eluszkiewicz et al.*, 1996). Planetary wave forcing in the winter extratropics can affect the summer subtropics (across the Equator). However, because the meridional gradient of absolute angular momentum in this region is small enough to neglect its advection (*Dunkerton*, 1989) it is unlikely that PW forcing explains latitudinal distributions and seasonal variations of upwelling in the tropical USLM. Instead, it is hypothesized that the existence of the middle-atmosphere Hadley circulation is required to explain these features (*Plumb and Eluszkiewicz*, 1999). It is also believed that the middle-atmosphere Hadley circulation plays a role in driving the easterly phase of the SAO through the absolute angular momentum transport because of strong nonlinearity around the tropical stratopause (*Dunkerton*, 1991). Although these features of the middle-atmosphere Hadley circulation have been examined in some general circulation models (*e.g.*, *Semeniuk and Shepherd*, 2001a; 2001b), they have not yet been confirmed by observations and reanalyses. Upward extension and improved accuracy of the latest reanalysis data will facilitate quantitative examination of the middle-atmosphere Hadley circulation (*e.g.*, *Sato and Hirano*, 2019) and its relationship with the SAO.

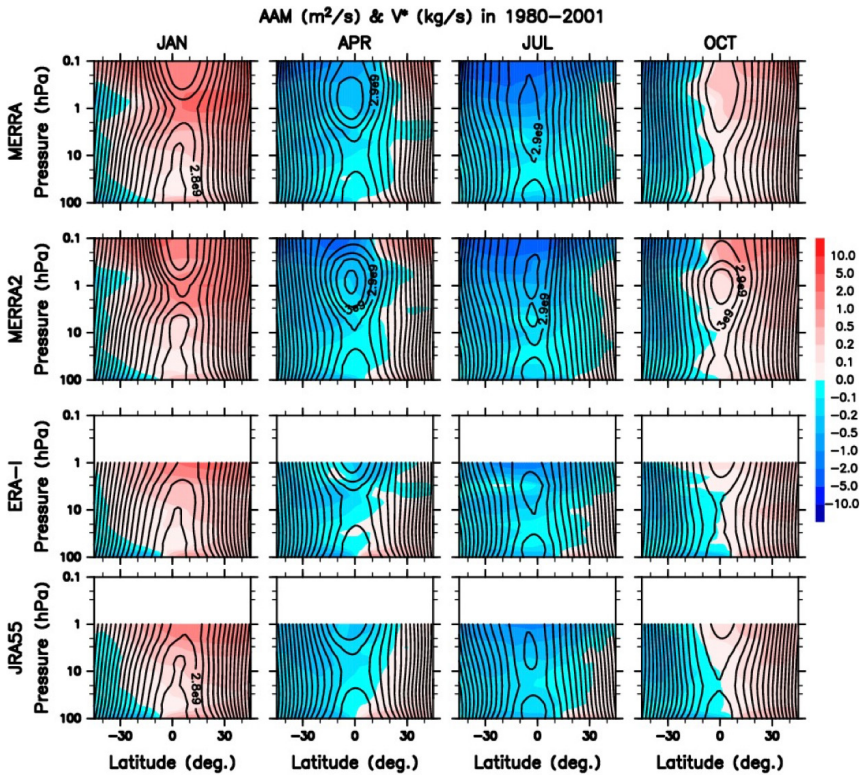

Figure 11.32: *Latitude-pressure sections of monthly- and zonal-mean absolute angular momentum (contours) and residual-mean meridional flow (colors) in (left to right) January, April, July, and October averaged over 1980-2001 from MERRA (top row), MERRA-2 (2nd row), ERA-Interim (3rd row), and JRA-55 (bottom row). Contour intervals are 10^8 m^2 s^{-1}.*

Next we show annual cycles of the residual-mean meridional circulation in the Tropics averaged over 1980 - 2001 for each of four reanalyses (*i.e.*, MERRA, MERRA-2, ERA-Interim, and JRA-55). Since it is difficult to distinguish wave-driven and thermally-driven meridional circulation in the Tropics, we just show basic features of the meridional circulation in the tropical USLM.

Figure 11.32 shows latitude-pressure sections of monthly zonal means of absolute angular momentum (M) and residual-mean meridional wind in January, April, July, and October. Four reanalyses show good agreement in the spatial structure of residual-mean meridional flow. The cross-equatorial flow from the summer to the winter pole, especially in January, tends to be maximized slightly above the trough in M, where the M isopleths become horizontal. This is probably because air parcels can move meridionally without any wave forcing in the trough of M (*Tung and Kinnersley*, 2001; *Dunkerton*, 1989; *Hitchman and Leovy*, 1986). The trough of M during the solstice seasons corresponds to the easterly phase of SAO.

In order to show a relationship between the residual-mean meridional flow and the SAO, seasonal variations in the residual-mean meridional wind and zonal-mean zonal wind from 15 °S - 15 °N at 1 hPa are shown in **Figure 11.33**. The SAO's easterly phase is maximized in January and July and stronger in January than in July for all the reanalyses, but MERRA-2 has a westerly bias compared to the other reanalyses throughout the year (see also *Section 11.3.1*). On the other hand, northward and southward residual-mean meridional flow in the Tropics is maximized in December and January and in July and August, respectively. In addition, maxima of northward and southward flow in MERRA-2 are smaller than those in the other reanalyses. These results are likely due to weaker planetary wave forcing in the winter subtropics (10 ° - 20 °N) in MERRA-2, which is associated with weaker cross-equatorial flow and weaker transport of absolute angular momentum (M). In addition, while weaker cross-equatorial flow induces weaker SAO easterlies through the weaker transport (*e.g.*, *Tomikawa et al.*, 2008), the weaker SAO easterly phase in MERRA-2 cannot create horizontally aligned isopleths of M and this suppresses cross-equatorial meridional flow due to "sideways control." Thus, the weaker cross-equatorial meridional circulation in MERRA-2 could not only be induced by the weaker subtropical wave forcing but also through the interaction between the SAO easterly phase and cross-equatorial flow. In the tropical USLM, wave-driven and thermally-driven (*i.e.*, Hadley) circulations as well as "sideways control" each contribute to driving the meridional circulation; it is beyond the scope of this report to quantify individual contributions.

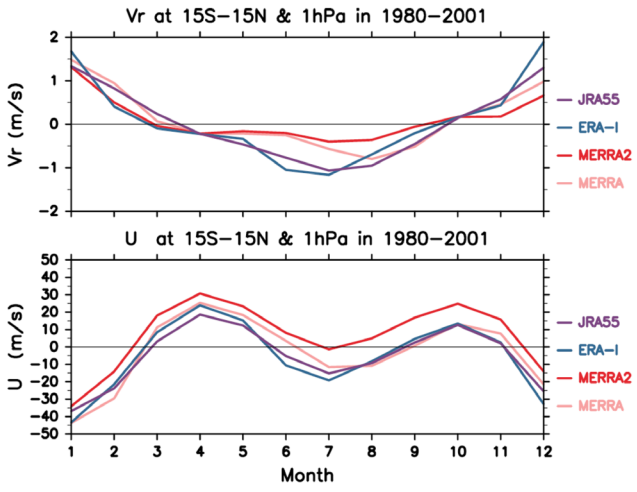

Figure 11.33: *Annual cycles averaged between 15 °S and 15 °N at 1 hPa of (top) the meridional component of the residual circulation and (bottom) the zonal mean zonal wind. Averages are over 1980 - 2001 and are given for JRA-55, ERA-Interim, MERRA, and MERRA-2.*

11.3.3 Inertial instability

Inertial instability is a hydrodynamic instability caused by an imbalance between the pressure gradient force and the centrifugal force. For zonally symmetric flow in the Earth's atmosphere, it is equivalent to the increase of the absolute angular momentum at latitudes moving away from the Equator. This condition is satisfied when a latitudinal shear of the zonal wind exists at the Equator, so that the inertial instability easily occurs in the Tropics. It creates vertically-stacked temperature structures (*i.e.*, pancake structures) induced by a local meridional circulation in the inertially unstable region (*cf.*, *Dunkerton*, 1981). An important role of inertial instability is to transport and homogenize the absolute angular momentum in the Tropics through the local meridional circulation, which partly contributes to an easterly phase of the SAO. A criterion of the inertial instability in zonally asymmetric flow is not yet established, but its analogue in zonally symmetric flow has been used in previous studies (*cf.*, *Knox*, 2003). Thus, we use $fq < 0$ as the criterion, where f is Coriolis parameter and q is Ertel's potential vorticity.

In this section, we show frequency of occurrence distributions of $fq < 0$, used here as a proxy for inertial instability. Ertel's PV (q) at 00 UT on each day was computed from MERRA, MERRA-2, ERA-Interim, and JRA-55, and used for the calculation. A horizontal resolution of the reanalysis data is 1.25 ° longitude and 1.25 ° latitude for MERRA and JRA-55, 0.625 ° and 0.5 ° for MERRA-2, and 1.5 ° and 1.5 ° for ERA-Interim. A missing value is assigned at the Equator for ERA-Interim and JRA-55 because of $f = 0$ there. Here, inertial instability frequency of occurrence rates are given as the percent of the time that a given longitude, latitude, and pressure grid point satisfies $fq < 0$.

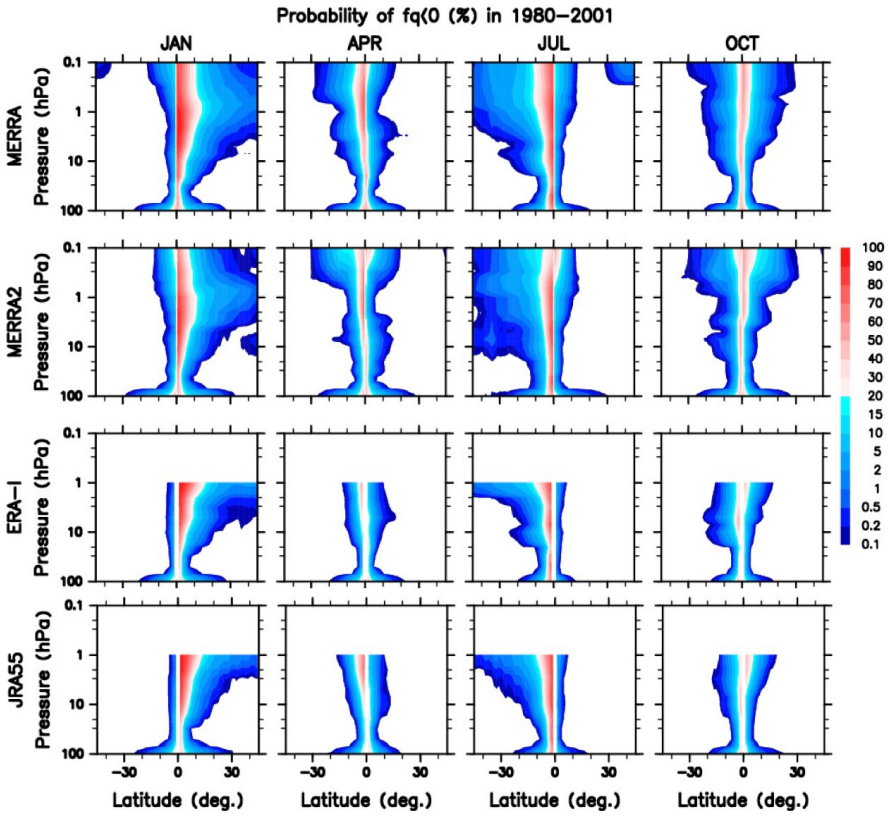

Figure 11.34: *Latitude-pressure sections of inertial instability frequency of occurrence rates in January, April, July, and October averaged over 1980 - 2001 for (from top to bottom) MERRA, MERRA-2, ERA-Interim, and JRA-55.*

Figure 11.34 shows latitude-pressure sections of the inertial instability frequency of occurrence rates during January, April, July, and October in MERRA, MERRA-2, ERA-Interim, and JRA-55. Although the magnitude of the frequencies is different among the four reanalyses because of the different horizontal resolution of the data used, they show qualitatively good agreement in their latitudinal and vertical distributions. The inertial instability frequency is larger in winter than in summer and is maximized around the winter stratopause. This feature is consistent with stronger planetary wave driving in the winter hemisphere, and with the fact that the SAO's easterly phase is maximized in the summer (*i.e.*, the absolute angular momentum is maximized in the winter). Isolated regions of 1 % occurrence rates near 40° latitude in MERRA in the summer near 0.1 hPa are due to noisier horizontal wind fields (and derived potential vorticity) compared to MERRA-2 (not shown).

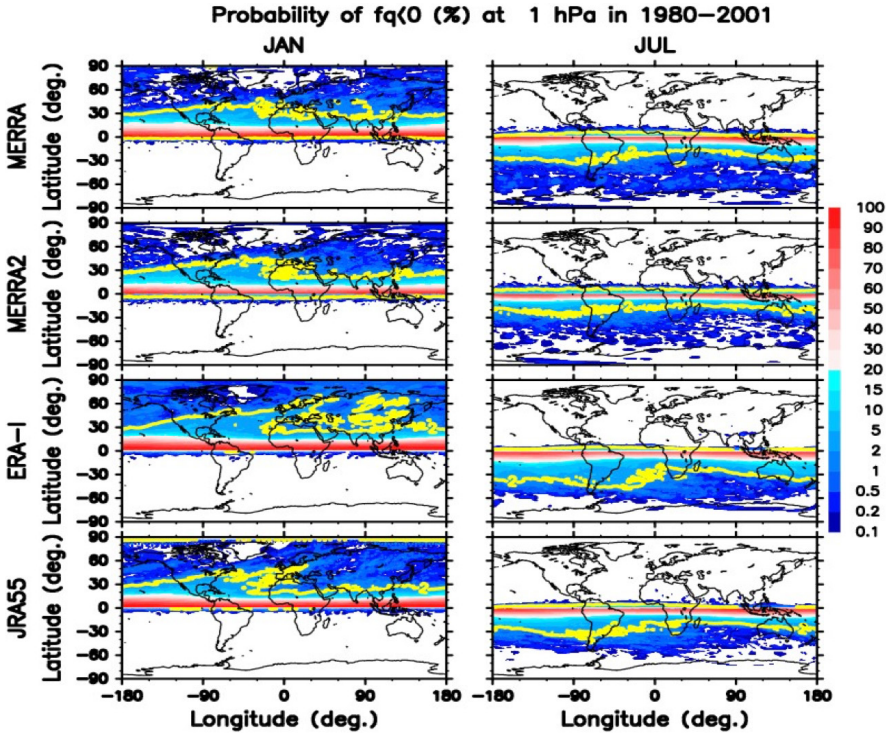

Figure 11.35: *Mercator maps of inertial instability frequency of occurrence rates at 1 hPa in January (left) and July (right) averaged over 1980 - 2001 for (from top to bottom) MERRA, MERRA-2, ERA-Interim, and JRA-55. The yellow contour indicates values of 2 %.*

Figure 11.35 shows Mercator maps of the inertial instability frequency at 1 hPa in January and July for each reanalysis. A tongue of high frequencies (highlighted by the yellow 2 % frequency contour) stretches poleward in the winter western hemisphere in both the NH (*i.e.*, January) and the SH (*i.e.*, July). The higher inertial instability frequencies in the western hemisphere are consistent with the results of *Knox and Harvey* (2005), but its magnitude is smaller here. Poleward elongation of the region of higher frequencies is larger in ERA-Interim and JRA-55 than in MERRA and MERRA-2. Since the zonally asymmetric inertial instability pattern is due primarily to the planetary wave breaking process, the differences in inertial instability frequency among the reanalyses may be related to the differences in planetary wave activity among the reanalyses mentioned in *Section 11.2.1.*

11.4 Polar Dynamics

11.4.1 Polar vortices

The circulation in the polar winter middle atmosphere is dominated by a large circumpolar vortex that forms as a result of decreased solar insolation (*Schoeberl and Hartmann*, 1991). These "polar vortices" are hemispheric in scale and persist throughout the winter in both hemispheres (*e.g.*, *Waugh and Polvani*, 2010; *Harvey et al.*, 2002, and references therein). They extend from the tropopause to the mesopause and they act to vertically couple the atmosphere-ionosphere system. For example, SSW disturbances to the polar vortex (*Butler et al.*, 2017; *Charlton and Polvani*, 2007, and references therein) are linked to weather patterns at the surface (*e.g.*, *Baldwin and Dunkerton*, 2001), mesospheric cooling (*Siskind et al.*, 2005; *Labitzke*, 1972), thermospheric warming (*Liu and Roble*, 2002; *Walterscheid et al.*, 2000), and anomalies in the ionosphere (*Goncharenko et al.*, 2010) both at high and low latitudes (*Pedatella et al.*, 2018). In the mesosphere-lower-thermosphere (MLT), descent in the vortex is required to transport reactive odd nitrogen produced by energetic particle precipitation from the thermosphere to the stratosphere (*Randall et al.*, 2015 and references therein). Throughout the stratosphere and mesosphere the shape and strength of the jet stream at the vortex edge affects vertical wave filtering (*Smith*, 1996; 1997). Thus, the polar vortices play an important role in coupling the atmosphere-ionosphere system.

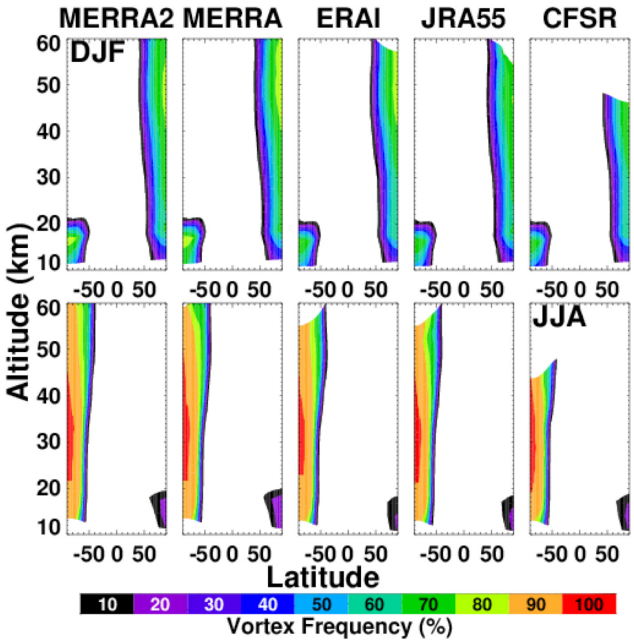

Figure 11.36: *Latitude-height plots of multi-year (2005 - 2015) average DJF (top) and JJA (bottom) polar vortex frequency as a function of latitude and altitude in five reanalyses (left to right, MERRA-2, MERRA, ERA-Interim, JRA-55, and CFSR).*

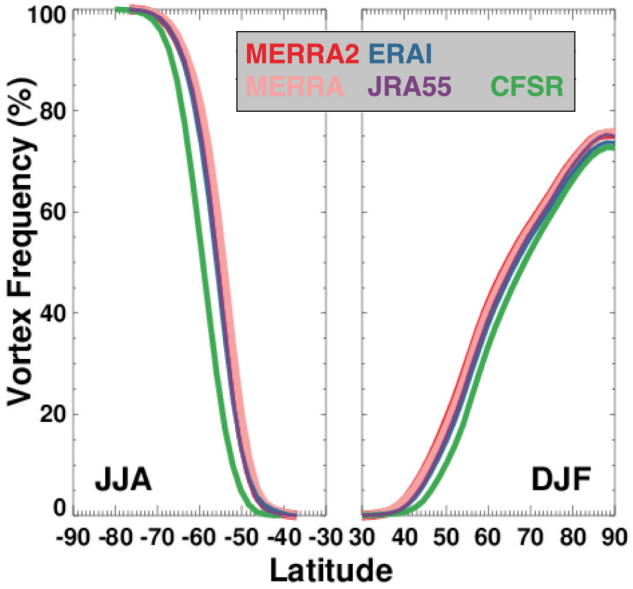

Figure 11.37: *Multi-year (2005 - 2015) average polar vortex frequency at one altitude in the upper stratosphere (1000 K; 2 hPa; 45 km) for JJA (left) and DJF (right) as a function of latitude.*

It is therefore of interest to evaluate the degree to which the reanalyses agree in terms of vortex structure and frequency of occurrence. In this work we identify the polar vortices using the streamfunction (ψ)-based algorithm described by *Harvey et al.* (2002). This vortex identification method is applied to MERRA-2, MERRA, ERA-Interim, JRA-55, CFSR/CFSv2 for the 11 years 2005 - 2015. In each reanalysis, on each day, for each altitude level and in each hemisphere, the polar vortex edge is defined and grid points inside (outside) the vortex are assigned a value of 1 (0). Thus, on each day a 3-D binary field of in-vortex points and exterior points is generated. Hereafter, vortex frequency of occurrence is defined as the percent of time a given grid point is located inside the vortex. As seen in **Figure 11.36**, all five reanalyses are in excellent agreement with respect to the latitude extension and magnitude of mean polar vortex frequency of occurrence rates during the winter months. These results demonstrate that all of these reanalysis datasets capture the primary multi-year winter mean vortex characteristics in both hemispheres.

In order to compare the reanalyses in more detail, we next look at depictions of polar vortex frequency in the upper stratosphere (**Figure 11.37**). This perspective reveals differences in vortex frequency that were obscured in the previous figure. At this altitude, multi-year mean polar vortex frequencies among MERRA, MERRA-2, ERA-Interim, and JRA-55 are in excellent agreement at all latitudes. CFSR wintertime vortex frequencies are 10 - 20 % lower than the other four reanalyses in the 50 ° to 70 ° latitude bands in both hemispheres. This could be attributed to the higher polar temperatures in the CFSR (see *Chapter 3*, **Figures 3.6** and **3.7**), hence a weaker polar night jet and lower vortex frequencies.

Figure 11.38 shows multi-year winter mean vortex frequency distributions in the longitude-altitude plane. All five reanalyses compared here are in excellent agreement with respect to their zonally asymmetric vortex frequency distributions. All five reanalyses contain a polar vortex that tilts westward with height from 15 km to stratopause altitudes. Overall, Antarctic vortex frequencies in CFSR (lower right panel) are lower compared to the other four datasets.

Finally, we examine the annual cycle in both the Arctic and Antarctic polar vortices near the stratopause in MERRA, MERRA-2, ERA-Interim, JRA-55, and CFSR. **Figure 11.39** shows multi-year (2005 - 2015) mean polar vortex frequencies (colored contours) as a function of geographic latitude and day of year at 1 hPa in the (**a**) NH and (**b**) SH in the five reanalysis datasets. MERRA-2 zonal mean winds are contoured in the background using thin black lines to provide dynamical context and illustrate how, at this altitude, 50 % frequency contours tend to coincide with maximum wind speeds. There is excellent agreement among the reanalyses in the vortex formation date in both hemispheres. In all five reanalysis datasets the Arctic vortex typically forms on 9 Sept and the Antarctic vortex forms on 6 March at this altitude.

There is also good overall agreement between the 5 reanalyses in the evolution of vortex latitudinal extent and duration. The polar vortices tend to be most confined to polar latitudes in CFSR/CFSv2 and present at lower latitudes in MERRA-2, and these differences are consistent with slight (1 ° - 2 °) differences in the mean latitude of the PNJ (not shown). The MERRA-2 (red) 50 % vortex frequency contour extends 5 - 10 % further equatorward than in the other four reanalyses, which reflects the sensitivity of the identification algorithm to slight differences in the horizontal

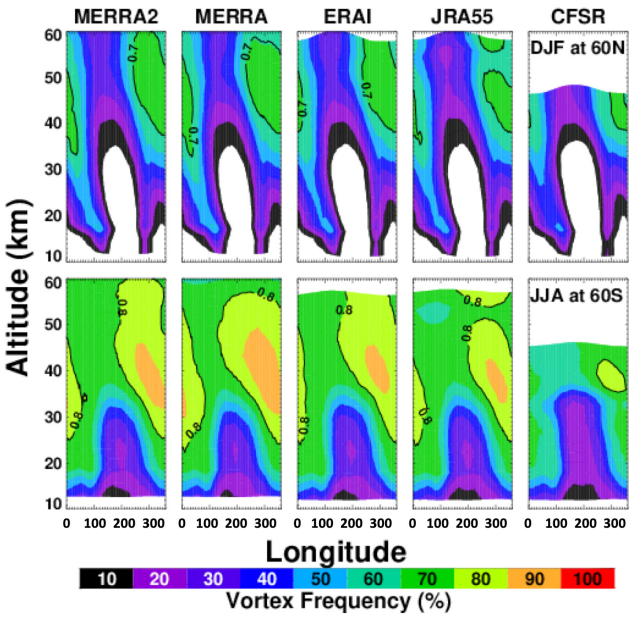

Figure 11.38: *Multi-year (2005 - 2015) average DJF (top) and JJA (bottom) polar vortex frequency as a function of longitude and altitude showing PW1 zonal asymmetry and a westward phase tilt with height.*

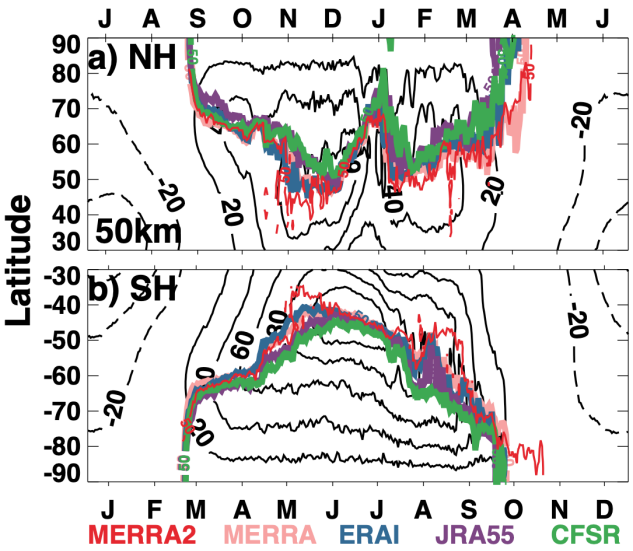

Figure 11.39: *Multi-year (2005 - 2015) mean polar vortex frequency (colored lines) as a function of geographic latitude and day of year at 1 hPa (~ 50 km) in the (a) NH and (b) SH in different 5 reanalysis datasets: MERRA, MERRA-2, ERA-Interim, JRA-55, and CFSR/CFSv2. Polar vortex frequencies correspond to the vortex being present 50 % of the time. Months in the NH are shifted such that the winter is in the middle of both panels. MERRA-2 zonal mean winds contoured every 20 m s^{-1} with thin black contour lines in the background. X-tick labels are on the 15th of each month. X-ticks appear on the top for the NH and on the bottom for the SH. Taken from Harvey et al. (2018). ©American Geophysical Union. Used with permission.*

winds. There is a 5-day spread in Arctic vortex breakup date and a 3-day spread in Antarctic vortex breakup date (when vortex frequencies go to zero, not shown). However, there is a significant amount of interannual variability in vortex breakup date, so small differences shown here are not necessarily representative of agreement in vortex longevity on a year-to-year basis. These results show that all of these reanalysis datasets sufficiently capture the multi-year mean seasonal evolution of the vortex at the stratopause during 2005 - 2015. However, users need to bear in mind that these multi-year averaged comparisons do not quantify the extent to which the reanalyses differ during individual years.

11.4.2 Planetary waves

According to *Charney and Drazin* (1961), low-frequency planetary waves (PWs) propagate upward from the troposphere during winter and grow to have large amplitudes in the stratosphere and mesosphere. PWs are supported by a northward potential vorticity gradient and can arise from tropospheric forcing due to zonal variability in solar heating (land-sea thermal contrasts), flow over large-scale orographic features, as well as through the growth of normal modes due to local instability, leading to both stationary and traveling PWs (*e.g.*, *Andrews et al.*, 1987).

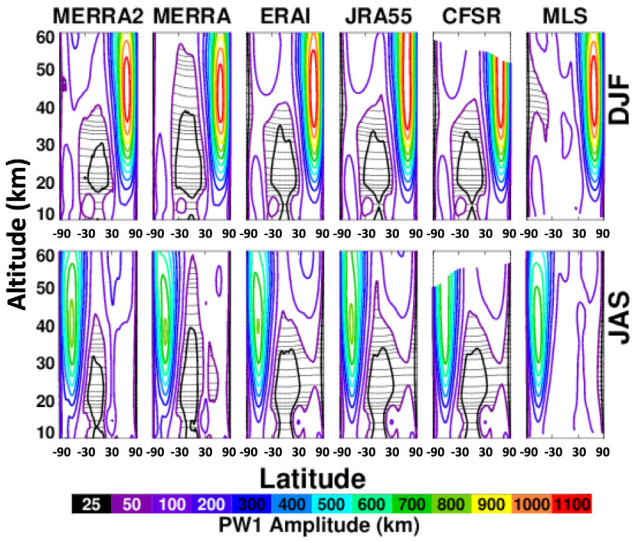

Figure 11.40: *Latitude-altitude plots of multi-year (2005 - 2015) mean PW-1 amplitudes based on MERRA, MERRA-2, ERA-Interim, JRA-55, CFSR, and MLS GPH for DJF (top) and JAS (bottom). Black symbols denote tropical regions where PW-1 amplitudes are smaller than 50 m.*

PWs deposit their momentum in the surf zone where winds are weak (*e.g.*, *Sassi et al.*, 2002). It is well known that PWs contribute significantly to the momentum budget of the stratosphere and mesosphere, act to redistribute trace species both meridionally and vertically (*e.g.*, *Kouker and Brasseur*, 1986), and create zonal asymmetries in temperature, winds, and gravity wave propagation (*Lieberman et al.*, 2013; *Smith*, 1996; 1997). Quasi-stationary planetary wave-1 (PW-1) structures have been documented extensively in observations of temperature, winds, and trace gas distributions (*e.g.*, *Demirhan Bari et al.*, 2013; *Ialongo et al.*, 2012; *Gabriel et al.*, 2011; *Offermann et al.*, 2003; *Allen et al.*, 2000; *Barnett and Labitzke*, 1990; *Hirota and Barnett*, 1977). In this section we compare the representation of quasi-stationary PW-1 patterns among MERRA, MERRA-2, ERA-Interim, JRA-55, and CFSR/CFSv2 during the 11 years spanning 2005 - 2015.

First, decadal average PW-1 latitude-altitude structures are compared in **Figure 11.40** during solstice. There is excellent agreement among the reanalyses and with MLS observations (far right column) in the magnitude and latitude-height structure of PW-1 amplitudes during the winter season. There are subtle differences in regions of the atmosphere where PW amplitudes are small; these occur in the Tropics and in the summer hemisphere. PW-2 results are similar (not shown).

Figure 11.41 shows the annual cycle of PW-1 amplitudes at 1 hPa near the stratopause at 60° latitude (left column) where amplitudes are largest and at 30° latitude (right column) where differences are large. Results indicate that there is remarkable agreement in winter PW-1 amplitudes among the reanalyses at 60° latitude in both hemispheres. In fact, the most apparent differences occur in the subtropics during summertime when PW-1 amplitudes are smallest (right column, note different y-axis range). It is interesting that all reanalyses except MERRA overestimate PW-1 amplitudes in the summer, in both hemispheres at this altitude level. This result is puzzling and requires further analysis.

11.4.3 Elevated stratopause events

Despite the absence of sunlight and the corresponding heating from shortwave absorption by ozone, the stratopause in polar night remains a well-defined feature of the general circulation. The temperature maximum is formed instead by adiabatic descent associated with the enhanced breaking of gravity waves which are also responsible for closing off the strong westerlies that form in the wintertime stratosphere (*Hitchman et al.*, 1989). The altitude of the stratopause is thus subject to dynamical variability, which is demonstrated most spectacularly over the Arctic in what are known as elevated stratopause (ES) events (*Chandran et al.*, 2013; *Limpasuvan et al.*, 2012; *Tomikawa et al.*, 2012; *Manney et al.*, 2008; *Siskind et al.*, 2007; 2010). These often occur during major SSWs (as first noted by *Labitzke*, 1972), when the persistently weakened lower stratospheric westerly jet and super-recovery of the upper stratospheric winds strongly modify the spectrum of gravity waves propagating up to the USLM (*Hitchcock and Shepherd*, 2013; *Tomikawa et al.*, 2012). They are characterized by a rapid (one to two week) initial descent or even disappearance of the polar stratopause, followed by the reformation of a temperature maximum at pressure levels as high as 0.03 hPa which, over the subsequent month or two, descends gradually to its climatological altitude near 1 hPa.

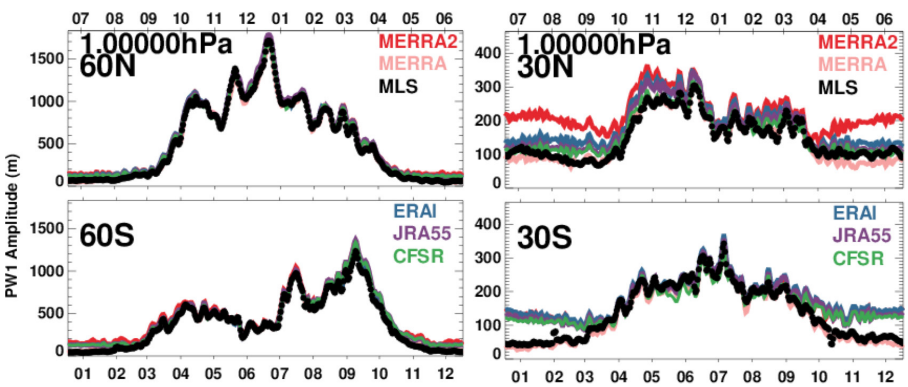

Figure 11.41: *Line plots of multi-year average (2005-2015) annual cycles of PW-1 amplitude at 30° and 60° N/S at 1 hPa near the stratopause. Note different y-axis ranges at the 60° vs. at 30° latitude. The months are shifted in the NH such that winter is in the middle of all panels.*

The initiation of the stratopause reformation as well as the slower descent of the mesospheric temperature anomalies are associated with an anomalous mean meridional circulation driven by planetary-scale Rossby waves likely generated within the middle atmosphere, as well as by small-scale gravity waves (*Hitchcock and Shepherd*, 2013; *Limpasuvan et al.*, 2012; *Tomikawa et al.*, 2012). The mechanism is related to but distinct from that responsible for the descent of tropical zonal jets in the QBO (*Hitchcock and Shepherd*, 2013). The stratopause reformation and descent is of particular importance for transporting trace species from the lower thermosphere into the mesosphere, as well as into the polar stratosphere (*Orsolini et al.*, 2017; *Siskind et al.*, 2010; *Manney et al.*, 2009; *Randall et al.*, 2006). The strong perturbation of the winds and temperatures throughout the stratospheric column and the interaction between stratospheric and mesospheric levels makes these events a challenging test for the representation of the gravity wave field in a forecast model. Given the general scarcity of observations to assimilate in the USLM, the forecast models of reanalyses are generally left to fend for themselves.

Figure 11.42 shows the evolution of the polar cap averaged temperature field plotted against time and pressure during four recent ES events that occurred in the Januaries of the years 2004, 2006, 2009, and 2013. These events coincided with major SSWs with 10 hPa, 60°N zonal mean zonal wind reversals that occurred on 5 Jan 2004, 21 Jan 2006, 24 Jan 2009, and 6 Jan 2013. Temperatures retrieved from the MLS instrument aboard the Aura satellite are available for the latter three events and serve as a good observational reference (top row of **Fig. 11.42**). The general evolution of the stratopause described above is evident in each case. There is some inter-event variability in the temperature of the elevated stratopause immediately following the disappearance of the climatological stratopause, as well as in the cold anomaly near 6 hPa that forms as the stratopause descends, but the overall similarity among the events is remarkable and apparent even in these three events.

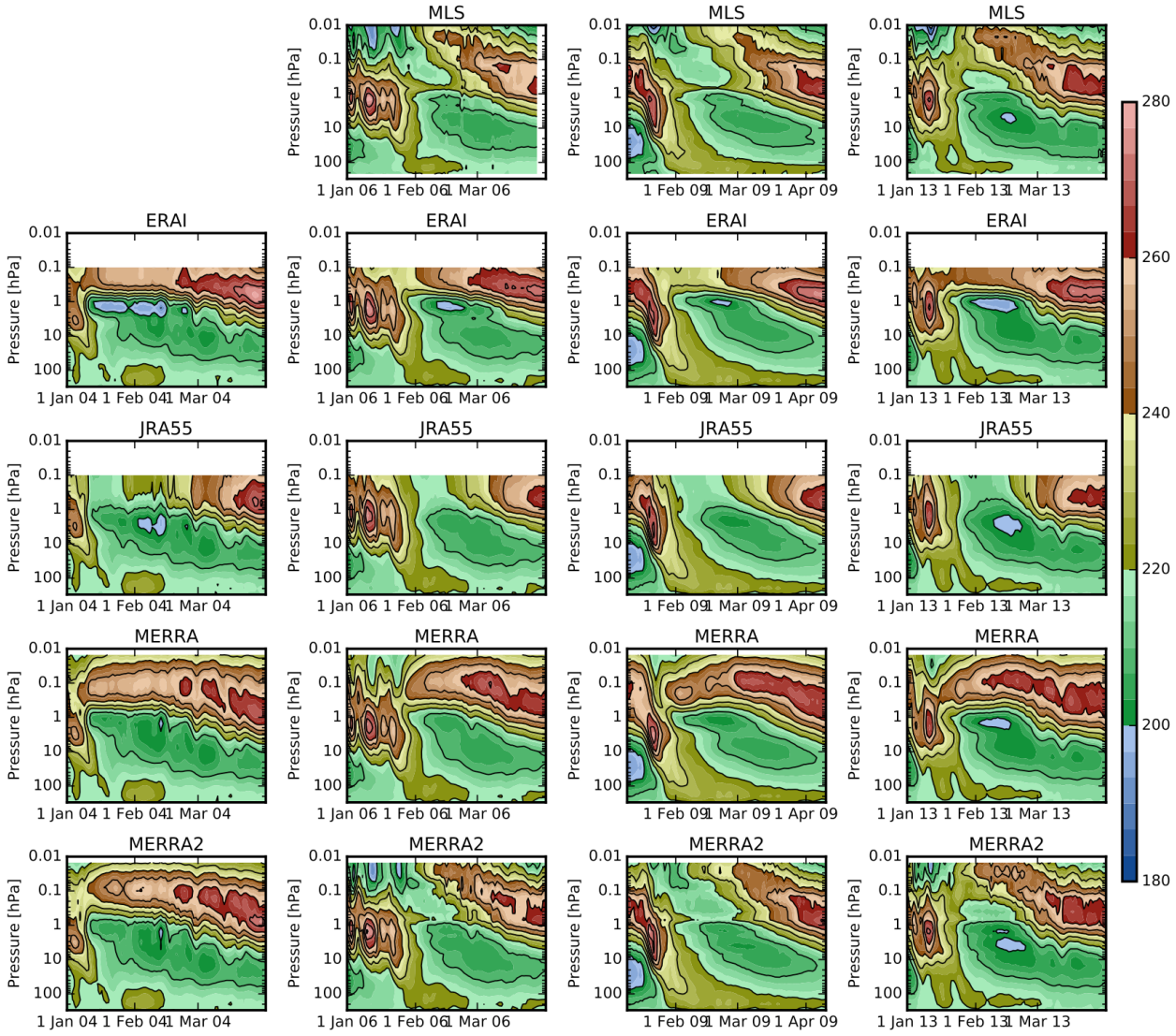

Figure 11.42: *Altitude-time sections of polar cap (averaged > 70°N) temperature (K) in (top) MLS, (2nd row) ERA-Interim, (3rd row) JRA-55, (4th row) MERRA, and (5th row) MERRA-2 during January, February, and March of (left) 2004, (2nd column) 2006, (3rd column) 2009, and (4th column) 2013.*

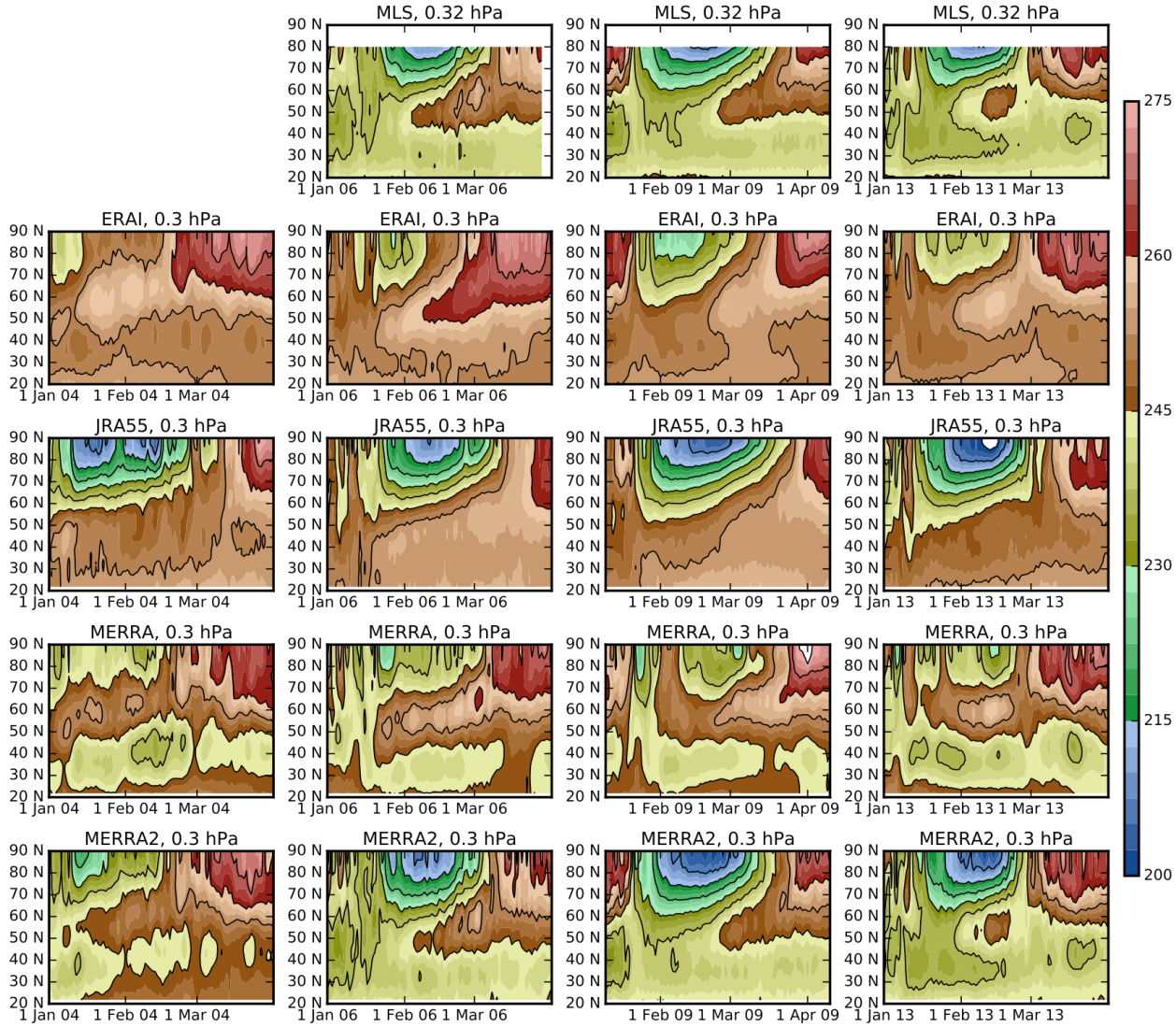

Figure 11.43: *Same as* ***Figure 11.42*** *but latitude-time plots at 0.3 hPa (~ 60 km).*

The corresponding temperatures from each of the four reanalyses are shown in the subsequent four rows. Three of the four reanalyses (ERA-Interim, MERRA, and MERRA-2) produce spuriously high temperatures near 0.1 hPa during the initial phase of the 2004 event. Similar biases are seen during the other three events in ERA-Interim and MERRA. MLS temperatures are assimilated in MERRA-2 when available; the effects of this assimilation on these events are immediately apparent. This may be associated with model lid or sponge layer effects in these three cases; however it is interesting that this temperature maximum occurs well below the model top (0.01 hPa) in the case of MERRA and MERRA-2. Also apparent is the formation of a shallow cold layer just below 1 hPa that is most pronounced in ERA-Interim but is also apparent in MERRA in all four events and in MERRA-2 during the 2004 event. The overall similarity between MERRA and MERRA-2 during the 2004 event suggests that the underlying forecast model in the two reanalyses treat these events quite similarly. The model lid of JRA-55 is at 0.1 hPa and it is therefore also unable to capture the elevated stratopause at its maximum altitude near 0.03 hPa. However, the JRA-55 reanalysis does not exhibit the temperature dipoles apparent in the other reanalyses, instead exhibiting nearly isothermal layers above 1 hPa that correspond to some extent with the descending stratopause seen in the observations. *McLandress et al.* (2013) studied the 2006 and 2009 events with the nudged Canadian Middle Atmosphere Model, which reproduced the MLS results almost perfectly (see their **Figures 3** and **4**). However the agreement degraded considerably when either the orographic or the non-orographic gravity wave drag, or both, were turned off (**Figures 5** and **6** of *McLandress et al.*, 2013), which shows the critical role of parameterized gravity wave drag in driving the mesospheric response to SSWs when there are no observations being assimilated in the mesosphere, and only the stratospheric state is being constrained.

Figure 11.43 shows a similar set of figures but now displays temperatures as a function of time and latitude at 0.3 hPa, an altitude just above the climatological stratopause. In the observed events, the cold anomaly is strongest at latitudes poleward of 60 °N.

Higher temperatures occur at lower latitudes first, giving rise about one month after the disappearance of the climatological stratopause to regions warmer than 245 K near 50 °N. These spread to the pole as the elevated stratopause descends. Latitudinal structure similar to this is seen in ERA-Interim, MERRA, and MERRA-2 even prior to the assimilation of MLS data, although overall temperatures are biased considerably high at this level, consistent with what was seen in the previous figure. In contrast, while the lower temperatures at higher latitudes in JRA-55 agree well with observations, there are no relatively warm regions to the south.

The temperature structures in ERA-Interim, MERRA, and MERRA-2 (when not constrained by the assimilation of MLS temperatures) are consistent with a strong sponge layer feedback caused by the presence of artificial momentum damping within the USLM, which, in these reanalyses, is acting to reduce the zonal mean zonal wind above 0.3 hPa (not shown). This feedback produces a spurious anomalous meridional circulation cell between the sponge layer and the region of anomalously low wave driving in the mid-stratosphere as described by *Shepherd et al.* (1996); see in particular their **Figure 1c**, though in this case the sign of the effective forcing is in the opposite sense. The different behavior of JRA-55 is consistent with the use of thermal damping towards the layer-averaged global mean temperature and the lack of momentum damping, unlike the other three reanalyses which use some form of momentum dissipation in their sponge layers (*Chapter 2*; *Fujiwara et al.*, 2017). Near a sponge layer, the presence or lack of a non-orographic gravity wave parameterization would seem to be of lesser direct relevance given that MERRA and MERRA-2 include such parameterizations while ERA-Interim and JRA-55 do not (*Chapter 2*; *Fujiwara et al.*, 2017). However, if the model lid is sufficiently high and the sponge is not applied to the zonal mean flow, *McLandress et al.* (2013) showed that non-orographic gravity waves can be important.

It is important to note that in almost all cases the representation of ES events in the USLM is not constrained by the assimilation of observations, and in all cases the effects of the forecast model sponge layers are directly felt and likely will be associated with artificial meridional circulations (*Shepherd et al.*, 1996). These inferred biases in the meridional circulations will have an effect on the inferred tracer transport as well. The assimilation of MLS temperatures into MERRA-2 results in close agreement with MLS temperatures during the period where observations are available, but events prior to this should be treated separately, and the presence of the sponge layer implies that the corresponding meridional circulation should not be trusted even during the assimilation period. The use of thermal dissipation as the sponge layer in JRA-55 avoids the strong spurious circulations that affect MERRA, ERA-Interim, and MERRA-2 prior to the assimilation of MLS temperatures, but the physical circulation evident in the observed temperature structure is also missing. Studies of ES events that make use of reanalyses must be aware of these shortcomings.

11.5 Tides and Normal Modes

11.5.1 Tides

Atmospheric solar tides are global-scale inertia-gravity waves with periods that are integer fractions of a solar day (*Chapman and Lindzen*, 1970). They are primarily driven by diurnally varying diabatic heating, such as the absorption of solar radiation by tropospheric water and stratospheric ozone, and the latent heat release associated with tropical convection (*Hagan and Forbes*, 2002; *Hagan et al.*, 1995). The diurnal (S_1) and semi-diurnal (S_2) variations around the globe can be decomposed into zonal harmonics with the "migrating" (Sun-synchronous) components for the S_1/S_2 tides represented by westward propagating wave number one / two. The remainder of the tidal zonal harmonics are "non-migrating components" and are excited mainly by zonally-asymmetric variations in (local time) heat sources or topography. Tides in reanalysis data provide an important "lower boundary condition" for driving so-called whole atmosphere models (*e.g.*, *Pedatella et al.*, 2014). They are also used for correcting the diurnal anomaly or drift seen in Sun-synchronous satellite measurements (*Zou et al.*, 2014).

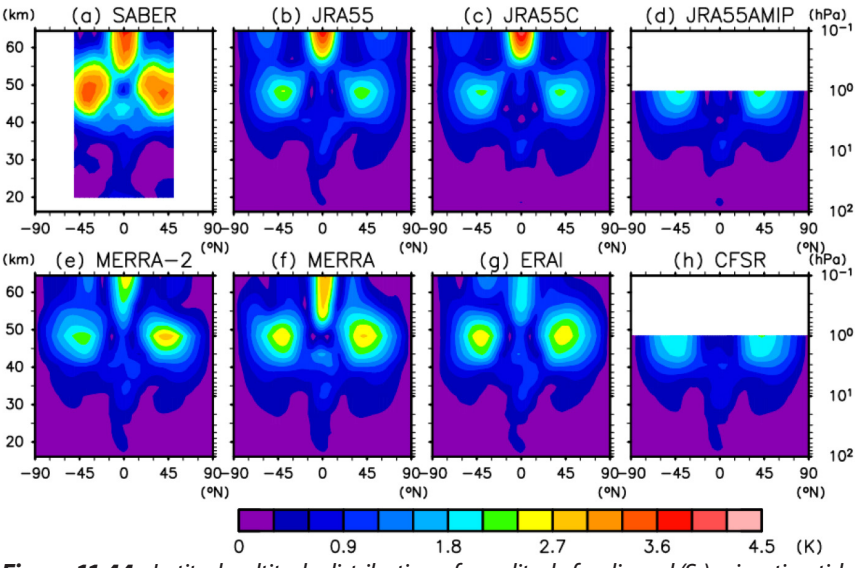

Figure 11.44: *Latitude-altitude distribution of amplitude for diurnal (S_1) migrating tide in temperature (K), as derived from (a) SABER, (b) JRA-55, (c) JRA-55-C, (d) JRA-55-AMIP, (d) MERRA-2, (e) MERRA, (f) ERA-Interim, and (h) CFSR. Taken from Sakazaki et al. (2018).*

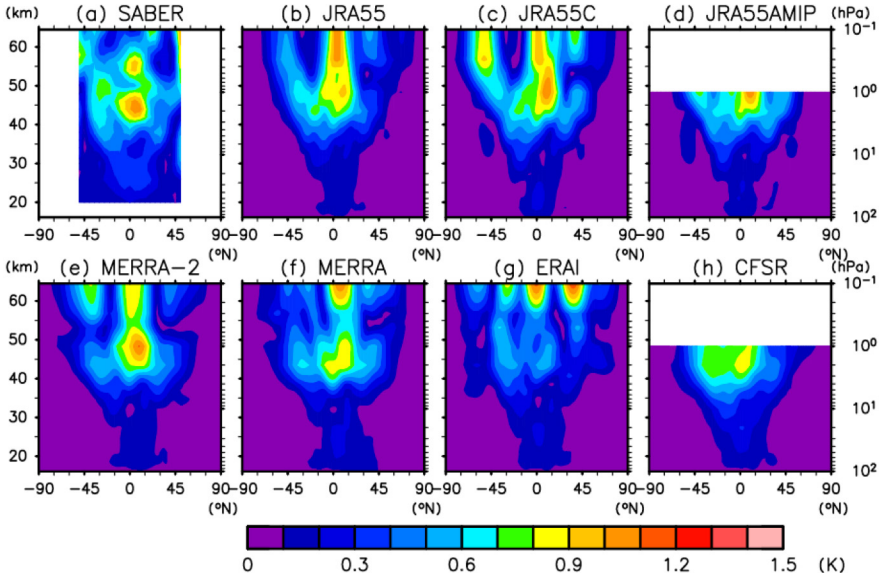

Figure 11.45: *Same as* ***Fig. 11.44*** *but for semidiurnal (S_2) migrating tide. Taken from Sakazaki et al. (2018).*

We analyze and compare data from five recent global reanalyses (MERRA-2, MERRA, JRA-55, ERA-Interim and CFSR) as well as SABER (not assimilated in any reanalyses) and MLS satellite measurements (only assimilated in MERRA-2) during the 7-year period 2006 - 2012. For JRA-55, the two other "family" members, JRA-55C and JRA-55AMIP, are analyzed to examine the effects of data assimilation on the representation of the solar tides. We will not consider here the JRA-25, ERA-40 and NCEP1/2 reanalyses. *Sakazaki et al.* (2012) showed that the global structure and seasonality of the S_1 migrating tide represented in JRA-25 or NCEP1/2 were less consistent with available observations than were the newer reanalyses data sets.

In this report, the (1) diurnal (S_1) migrating tide, (2) semidiurnal (S_2) migrating tide, and (3) nonmigrating tides are extracted and diagnosed individually. For SABER, a composite analysis is made at each longitude-latitude bin after a 60-day running mean that is regarded as daily-mean is subtracted from the original time series (see *Sakazaki et al.* 2018 for details). For reanalyses, first, 3- or 6-hourly diurnal variations in universal time (UT) are extracted at each grid point with a composite analysis after the subtraction of the daily-mean. Next, by averaging data at the same local time (LT) for each latitude band, migrating tides that are a function of LT are calculated; for example, for 6-hourly reanalyses, data at 0000 LT is the average of data points at (0000 UT, 0 °E) (0600 UT, 90 °E) (1200 UT, 180 °E) (1800 UT, 270 °E), while data at 01:00 LT is the average of data points at 00:00 UT (15 °E), 06:00 UT (105 °E), 12:00 UT (195 °E) and 18:00 UT (285 °E). Then, the harmonic fitting is performed for the diurnal variations in LT to extract the migrating S_1 and S_2 components. Note that the 6-hourly data (ERA-Interim, JRA-55 and CFSR) cannot resolve S_2 at each grid point; but the 'migrating component' of S_2 can be extracted by using data at grid points on the same latitude belt as noted above. Finally, we diagnose S_1 nonmigrating tides by applying the zonal wavenumber decomposition for the S_1 component (*Dai and Wang*, 1999). See *Sakazaki et al.* (2018) for the comparison of nonmigrating tides in physical space.

Figure 11.44 shows the latitude-altitude distribution of amplitude for annual-mean S_1 migrating temperature tides computed from SABER data (upper left panel) and from the various reanalyses from 2006 - 2012. Both reanalyses and observations show that tidal amplitudes increase with altitude in the Tropics; tides based on SABER observations reach ~4 K in the tropical lower mesosphere. This feature is underestimated by 30 - 50 % in the various reanalyses. The tidal maxima in the midlatitude upper stratosphere are similarly underestimated by the reanalysis systems by 20 - 30 % compared to SABER. Notably the JRA-55C and JRA-55AMIP results are close together and differ from the JRA-55 results, indicating that satellite measurements improve the tidal representation in reanalyses.

Figure 11.45 shows the latitude-altitude distribution of amplitude for annual-mean S_2 migrating tides in temperature. Observations and reanalyses indicate that amplitudes are largest in the Tropics, with a local maximum around at 40 - 45 km (up to ~1.2 K), *i.e.*, close to the location of maximum in ozone heating. Note that the ERA-Interim overall shows a smaller amplitude in the stratosphere (reduced by up to ~50 % compared to SABER and the other reanalyses).

Figure 11.46 shows the zonal wavenumber dependence for the annual-mean *S*1 (24 hour) harmonic of non-migrating tides for each symmetric and anti-symmetric component with respect to the Equator (migrating component, westward zonal wavenumber 1, is not shown). All data sets show that zonal wavenumber 0 (so-called D0; particularly for anti-symmetric components), westward zonal wavenumbers 5 and 2 (DW5 and DW2), and eastward zonal wavenumber 3 (DE3) are dominant, being consistent with previous studies (*Sakazaki et al.*, 2015; *Forbes and Wu*, 2006; *Zhang et al.*, 2006). Although the dominant wavenumbers agree among the data sets, their magnitudes display some differences. The biggest outliers are JRA-55C and JRA-55AMIP and those two datasets display somewhat larger amplitudes than the full-input reanalyses (that assimilate both conventional and upper air observations). Another marked difference is seen for DE3; the MERRA and MERRA-2 results are close to the SABER but the other reanalyses have larger amplitudes than SABER above the middle stratosphere (pressures less than 3 hPa).

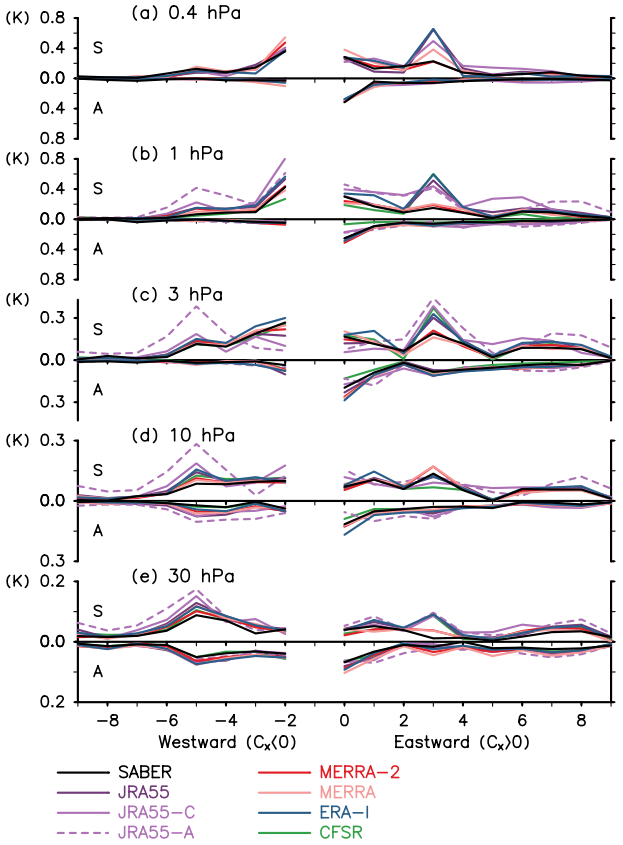

Figure 11.46: *Amplitudes for each zonal wavenumber component of diurnal (S_1) nonmigrating tides for the region between 10°S and 10°N, at (a) 0.4 hPa, (b) 1 hPa, (c) 3 hPa, (d) 10 hPa and (e) 30 hPa. Top and bottom half in each panel shows the results of symmetric and anti-symmetric components, respectively. Positive and negative wavenumbers are for the eastward and westward travelling waves, respectively. The S1 migrating tide (westward wavenumber 1) is not shown. Modified from Sakazaki et al. (2018).*

To summarize, the latest reanalyses agree reasonably well with each other and with the satellite observations for both migrating and nonmigrating components including their vertical and meridional structure. However, the agreement among reanalyses is better in the lower stratosphere and differences increase in the USLM. The diurnal migrating tides are weaker in the reanalyses compared to SABER, although such differences are less clear between MLS and the reanalyses (not shown). Reanalyses are a very useful tool to investigate the global structure of tides and its temporal variability. At the same time, one should note that the representation of tides is significantly affected by assimilated satellite data so that the present intercomparison results during 2006-2012 do not necessarily apply to other periods with different data assimilated (especially before 2000 when AMSU was not assimilated; see **Fig. 11.46.** See also *Sakazaki et al.*, 2018 for more details.

11.5.2 Quasi-2-day wave

The quasi-2-day wave (QTDW) is a well-documented feature of upper stratospheric and mesospheric dynamics that consists primarily of a westward propagating zonal wave number 3 that moves around a latitude circle in approximately 6 days. With a wave-3, this leads to local oscillations of 2 days, giving it the name "2-day wave". Early evidence of the QTDW was found in wind observations and radiances from meteor radar, satellite, and rocket-borne instruments (*e.g.*, *Burks and Leovy*, 1986; *Rodgers and Prata*, 1981; *Coy*, 1979; *Muller and Nelson*, 1978). Subsequent analyses of wind, temperature, and constituent observations from a plethora of ground-based and satellite-based instruments have shown the QTDW to be a major, recurring dynamical feature in the mesosphere and lower thermosphere (MLT) that is most prominent in the extratropical summer hemisphere (*Gu et al.*, 2013; *Tunbridge et al.*, 2011; *Pancheva*, 2006; *Garcia et al.*, 2005; *Limpasuvan and Wu*, 2003; *Lieberman*, 1999; *Harris*, 1994; *Wu et al.*, 1993).

Detailed studies of the upper stratospheric QTDW using operational meteorological analyses (*e.g.*, *Orsolini et al.*, 1997; *Randel*, 1994) have analyzed wavenumber-frequency spectra and potential vorticity-based diagnostics from daily wind and temperature fields. The results of these studies supported earlier theoretical results indicating that the QTDW originates primarily from regions of baroclinic instability in the easterly mesospheric summer jet (*Pfister*, 1985; *Plumb*, 1983), but also from regions of barotropic instability of the easterly jet in the subtropical upper stratosphere (*e.g.*, *Manney and Nathan*, 1990; *Burks and Leovy*, 1986), itself triggered by inertial instability (*Orsolini et al.*, 1997). The QTDW also projects onto a global zonal wavenumber 3 normal mode. Furthermore, these studies also clearly demonstrated the utility of stratospheric analyses for providing a fully self-consistent set of meteorological variables needed to describe the physical mechanisms that drive the QTDW and other key circulation features related to normal modes in the stratosphere, mesosphere, and lower thermosphere.

One aspect of the QTDW that is not yet well understood is the cause of its intraseasonal and interannual variability, which can have a wide-ranging effect on, *e.g.*, summer polar mesopause temperatures (*France et al.*, 2018; *Siskind and McCormack*, 2014), thermospheric neutral winds (*Chang et al.*, 2011), and ionospheric electron content (*Yue et al.*, 2012). Modeling and observational studies have shown that underlying variations in the background zonal wind field throughout the tropical and extratropical stratosphere and lower mesosphere that promote both baroclinic and barotropic instability are likely a key source of observed intraseasonal and interannual variability in the QTDW (*McCormack et al.*, 2014; *Rojas and Norton*, 2007; *Limpasuvan et al.*, 2000; *Norton and Thuburn*, 1999).

Reanalysis data sets extending into the USLM can now provide a more comprehensive understanding of the dynamical origins of QTDW variability. To this end, it is necessary to first understand how the QTDW is represented in current reanalysis data sets. In this section, the characteristics of the QTDW are compared using three reanalysis temperature data sets extending into the mesosphere: MERRA-2, JRA-55, and ERA-Interim.

The comparisons are performed using data from 2010, focusing on the seasonal variability in the QTDW.

The representation of the QTDW, and any other planetary scale normal modes, in reanalyses of the USLM will depend on a variety of factors. These factors include the vertical domain of the analysis system, the physical parameterizations used in the atmospheric model component, and the type of observations (if any) that provide information within this altitude region. In comparing the QTDW among the three reanalysis data sets, we note that there are two important features that distinguish MERRA-2 from JRA-55 and ERA-Interim. First, MERRA-2 extends to higher altitudes than ERA-Interim and JRA-55; the top pressure levels used for this comparison are 0.015 hPa for MERRA-2 and 0.1 hPa for both ERA-Interim and JRA-55. Second, only MERRA-2 assimilates temperature observations from the MLS instrument in the USLM.

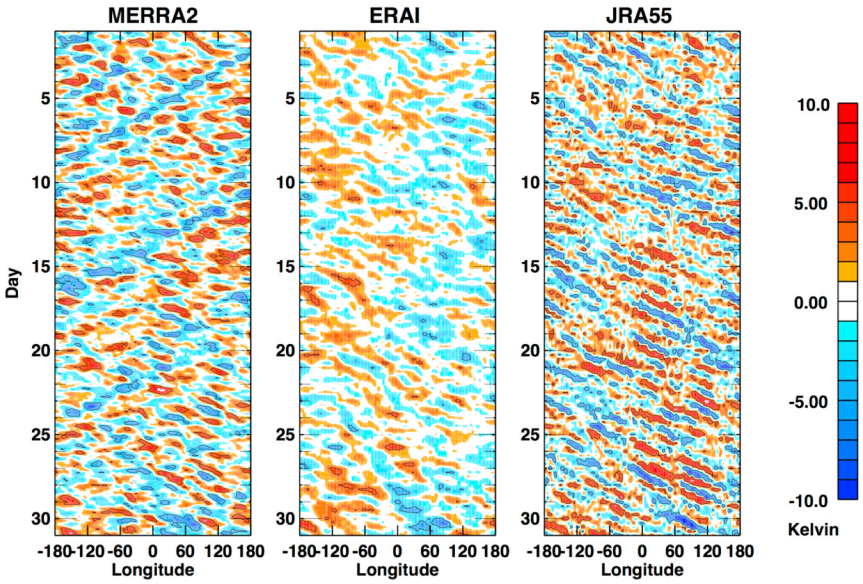

Figure 11.47: *Hovmöller diagrams at 30 °S and 0.3 hPa of temperature anomalies (minus the zonal and time mean) in MERRA-2 (left), ERA-Interim (middle), and in JRA-55 (right) during January 2010. Solid contours drawn at ± 4 K.*

To illustrate how these and other differences impact the reanalysis, **Figure 11.47** shows Hovmöller plots of temperature anomalies (zonal and time mean subtracted at each grid point to remove stationary wave components) for 30 °S at the 0.3 hPa level for January 2010 from (left) MERRA-2, (center) ERA-Interim, and (right) JRA-55. During this time period, prominent westward- and eastward-propagating temperature anomalies in the range of ±5 K can be seen in MERRA-2. The corresponding ERA-Interim temperature anomalies are weaker, typically in the range of ±2 K, and show some eastward propagation but little to no westward propagation. The JRA-55 temperature anomalies at this latitude and pressure level exhibit higher frequency eastward propagating features than either ERA-Interim or MERRA-2 up to ± 10 K. We note that 0.1 hPa is the top reported level of the JRA-55 data set, and so the reanalysis may be influenced by model upper boundary effects. Although a more detailed comparison is needed to conclusively identify the reasons for the differences among the three reanalyses shown in **Figure 11.47**, this initial comparison illustrates that all reanalysis data sets (even MERRA-2) must be used with caution in the USLM. Ideally, any studies using reanalyses at these upper levels should include validation with independent observations whenever possible.

With this caveat in mind, we compare the representation of the QTDW in MERRA-2, ERA-Interim, and JRA-55 during 2010. To describe the characteristics of the QTDW, a two-dimensional fast Fourier transform (2DFFT) (*Hayashi*, 1971) in longitude and time is applied to the reanalysis temperature anomaly fields (see **Fig. 11.47**) at a given latitude and pressure level. Following the procedure described in *McCormack et al.* (2009), daily zonal means are subtracted from each 3-hourly (MERRA-2) or 6-hourly (JRA-55 and ERA-Interim) longitude-time field and then a cosine taper is applied to the first and last 10 % of each record in time. The resulting power spectrum describes the amount of variance at each frequency and zonal wave number. Variance associated with the QTDW is isolated by reconstructing the longitude-time fields using the inverse 2DFFT with a bandpass filter for a given zonal wavenumber at frequencies from 0.45 - 0.6 cycles per day. This frequency range was determined by examining individual wavenumber-frequency spectra from the reanalysis temperature data throughout the year at latitudes in the lower mesosphere where the QTDW signal is largest. The 2DFFT is applied to reanalysis temperature fields on a monthly basis, producing a mean amplitude of the QTDW over the month-long analysis interval. Observational studies of the global QTDW structure have found evidence of prominent westward zonal wavenumber 3 and wavenumber 4 components (*e.g.*, *McCormack et al.*, 2014; *Gu et al.*, 2013; T*unbridge et al.*, 2011). Here we examine both components, focusing on the months of January and July when the QTDW amplitudes are found to be largest in the respective summer hemispheres. For these comparisons, we limit our attention to the region of the USLM between 0.1 - 10 hPa.

Figure 11.48 plots the altitude and latitude dependence of mean QTDW wavenumber 3 amplitudes for January 2010 (left column) and July 2010 (right column) from MERRA-2 (top), ERA-Interim (middle), and JRA-55 (bottom). All three reanalyses show qualitatively similar latitudinal structure in the QTDW, but there are large quantitative differences. MERRA-2 shows the largest amplitude in the mid-latitude mesosphere and in a narrow subtropical tongue extending down to the stratopause level, likely tied to the aforementioned regions of jet instability.

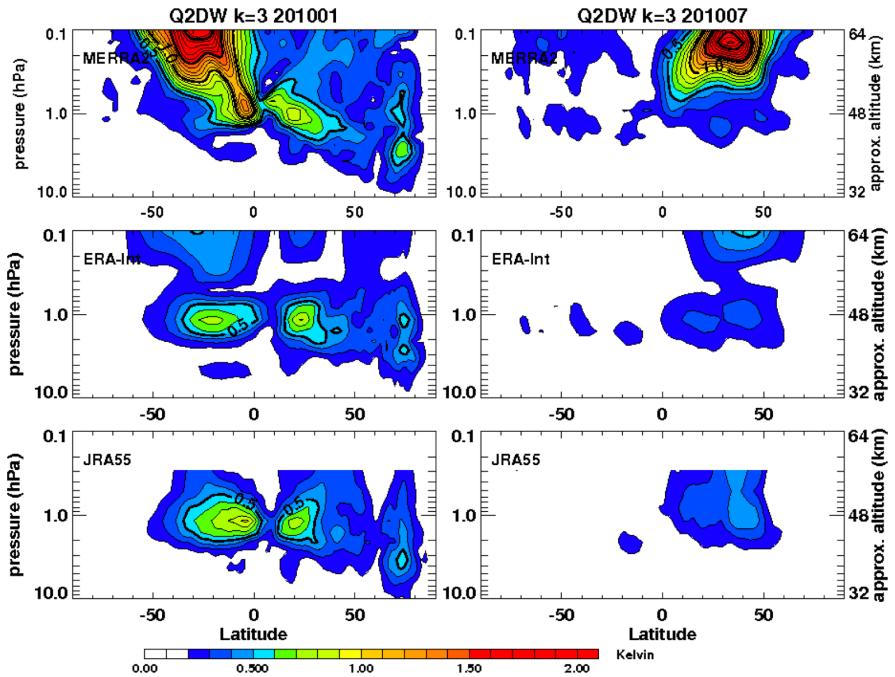

Figure 11.48: *Latitude-altitude sections of quasi-2-day wave amplitudes for westward zonal wavenumber 3 for January (left) and July (right) in 2010 from MERRA-2 (top), ERA-Interim (middle) and JRA-55 (bottom). Thin contours drawn every 0.1 K starting at 0.2 K, thick contours drawn every 0.5 K.*

In both months, peak QTDW amplitudes from MERRA-2 range from 1.5 - 2 K from 10° - 50° latitude in the summer hemisphere above the 1 hPa level. These values are much larger than the peak amplitudes of 0.7 - 0.9 K seen in ERA-Interim and JRA-55, which are limited to the region between 1 - 2 hPa. This is to be expected since the MERRA-2 reanalysis extends higher in altitude and includes mesospheric temperature observations. All three reanalyses show similar seasonal behavior in the upper stratosphere, in that the zonal wavenumber 3 QTDW amplitudes are larger in SH summer (January) than in NH summer (July) near the 1 hPa level.

Figure 11.49 shows monthly mean amplitudes of the QTDW for zonal wavenumber 4 during January and July 2010 from the three different reanalyses. As with the wavenumber 3 case, here all three reanalysis data sets show similar latitude structure in the peak QTDW amplitudes. In contrast to the zonal wavenumber 3 component, the zonal wavenumber 4 QTDW is largest during NH summer throughout the stratosphere and lower mesosphere in MERRA-2, ERA-Interim, and JRA-55. Again, the peak values of the QTDW amplitudes are much larger in MERRA-2 temperatures than in JRA-55 and ERA-Interim, and only MERRA-2 exhibits a strong QTDW signal above the 1 hPa level.

Since the QTDW is mainly a mesospheric phenomenon, the extended vertical domain and additional mesospheric observations from MLS allow the MERRA-2 reanalysis to better capture the main features of the QTDW in USLM temperatures as compared to ERA-Interim and JRA-55. Reanalysis systems with lower tops that lack mesospheric observations will not capture the main features of the QTDW. This reinforces the concept that the origin and propagation of the QTDW is mainly controlled by mesospheric dynamical variability. Reanalysis systems need to reproduce this variability in order to properly diagnose the physical mechanisms controlling both intraseasonal and interannual variability of the QTDW.

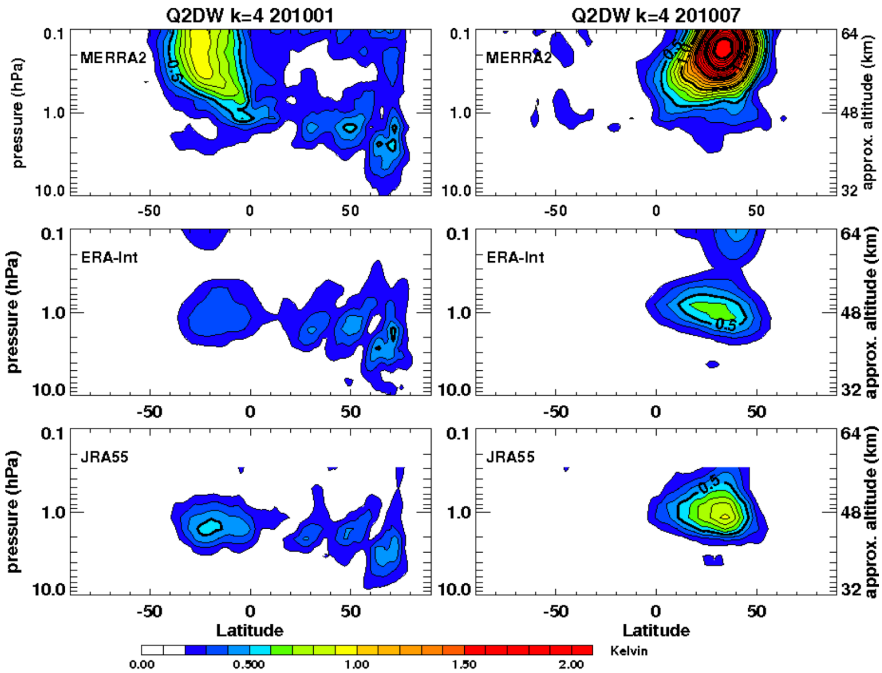

Figure 11.49: *Latitude-altitude sections of quasi-2-day wave amplitudes for planetary wavenumber 4 in January (left) and July (right) in 2010 in MERRA-2 (top), ERA-Interim (middle) and JRA-55 (bottom). Thin contours drawn every 0.1 K starting at 0.2 K, thick contours drawn every 0.5 K.*

11.5.3 Quasi-5-day wave

The quasi-5-day wave (QFDW) consists of a westward propagating zonal wavenumber 1 disturbance that is related to the first symmetric normal (Rossby) mode. It has been observed in surface pressure observations (see, *e.g.*, *Madden and Julian*, 1972, and references therein), and is routinely found in reanalysis data sets throughout the tropical and extratropical troposphere and stratosphere, having a period ranging from ~4 - 7 days. The QFDW has also been observed in the mesosphere (*e.g.*, *Iimura et al.*, 2015; *Talaat et al.*, 2001, 2002). The origins of the QFDW in the stratosphere and lower mesosphere are complex, and may involve different mechanisms, including latent heat release in the tropical upper troposphere (*Miyoshi and Hirooka*, 2003), possible nonlinear interactions in the stratosphere between extratropical planetary scale waves propagating upward from the troposphere (*Talaat et al.*, 2002), and amplification via baroclinic instability in the mesosphere (*Lieberman et al.*, 2003). The QFDW plays a prominent role in the dynamics of the MLT region, particularly in the occurrence of polar mesospheric clouds (PMCs) at high latitudes in summer (*Nielsen et al.*, 2010).

Given the complex dynamical interactions throughout the troposphere, stratosphere, and mesosphere that give rise to the QFDW, capturing the key characteristics of the global circulation feature is a good test for reanalysis systems extending into the USLM region. In this section we compare the QFDW in temperature during 2010 from the MERRA-2, ERA-Interim, and JRA-55 reanalyses using the 2DFFT method described in the previous section. For this comparison, the 2DFFT is applied to temperature anomaly fields using a bandpass for westward zonal wavenumber 1 and 0.16 - 0.25 cycles per day (periods of 4.25 - 6 days). This frequency range was determined by examining individual wavenumber-frequency spectra from the reanalysis temperature data throughout the year at latitudes in the stratosphere where the QFDW signal is largest.

Figure 11.50 shows the latitude and altitude dependence of the mean QFDW temperature amplitudes from 10 - 0.1 hPa during January 2010 (left column) and August 2010 (right column) from MERRA-2 (top), ERA-Interim (middle), and JRA-55 (bottom). The January 2010 results from all three reanalyses show remarkably consistent results, both qualitatively and quantitatively. In January, two distinct patterns emerge. The first pattern is relatively weak (0.6 - 1 K) and hemispherically symmetric with maxima near 40°N and 40°S from 1 - 3 hPa. This pattern is qualitatively consistent with the theoretical structure of the first symmetric normal mode. The second pattern is much stronger (2 - 3 K) and is present throughout the stratosphere and lower mesosphere at high Northern latitudes, in contrast to the expected theoretical structure of the first symmetric normal mode. There is hemispheric asymmetry in this second QFDW pattern in the sense that amplitudes in January are substantial poleward of 60°N, but are extremely small in the SH polar regions. This high northern latitude signal extends above the 1 hPa level in the MERRA-2 results, consistent with the system's higher top and inclusion of MLS mesospheric temperature observations, as discussed in the previous section. Between 10 hPa and 1 hPa, the amplitudes of the high-latitude QFDW signal in all three reanalyses are in good agreement. As discussed below, these two distinct patterns in the QFDW structure shown in **Figure 11.50** suggest that different processes may be involved in producing the QFDW signal within different latitude regions.

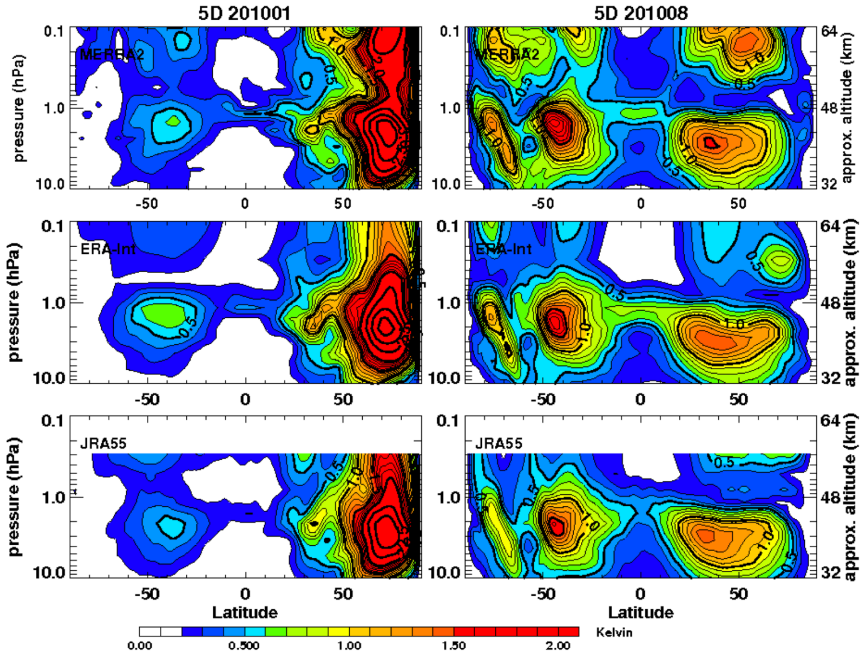

Figure 11.50: *Latitude-altitude sections of quasi-5-day wave amplitudes for January (left) and August (right) in 2010 in MERRA-2 (top), ERA-Interim (middle) and JRA-55 (bottom). Thin contours drawn every 0.1 K starting at 0.2 K, thick contours drawn every 0.5 K.*

During August 2010 (**Figure 11.50**, right column), all three reanalyses again show very good qualitative and quantitative agreement between 10 hPa and 1 hPa. The dominant pattern is a hemispherically symmetric feature with peak amplitudes of ~2 K near 2 hPa between 20° and 50° latitude that is qualitatively consistent with the expected structure of the first normal mode. The amplitude of this hemispherically symmetric feature is roughly twice as large as a similar pattern seen in the upper stratosphere between 30° - 50° latitude during January (**Figure 11.50**, left column). In contrast to the very strong 2 - 3 K QFDW signal seen at high Northern latitudes in January, the corresponding high latitude feature in the SH during August is a much weaker ~1 K signal over a narrower latitude region and smaller altitude range.

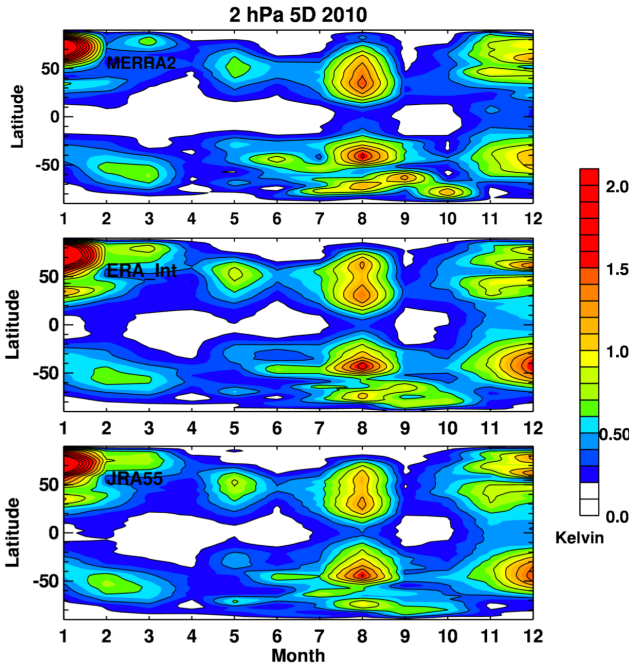

Figure 11.51: *Latitude-time plots of quasi-5-day wave amplitudes at 2 hPa during 2010 in MERRA-2 (top), ERA-Interim (middle) and JRA-55 (bottom). Contours every 0.2 K.*

In addition, while in January (left panels) the QFDW amplitudes largely maximize at high northern (winter) latitudes, in the SH winter (right panels) there is a double maximum, with large amplitudes poleward of the jet core that are distinct from the maximum in mid-latitudes. MERRA-2 and ERA-Interim results both show a separate maximum in the QFDW signal in the lower mesosphere from 0.3 - 0.1 hPa. There is also evidence of a separate QFDW amplitude maximum in the NH extratropical lower mesosphere in all three reanalyses from 40° - 70° N.

The seasonal variation of the monthly mean QFDW amplitudes at 2 hPa during 2010 is shown in **Figure 11.51**. This pressure level is near the peak of the upper stratospheric, hemispherically symmetric feature seen in all three reanalyses (**Figure 11.50**). The largest QFDW amplitudes (> 2 K) are seen consistently at high Northern latitudes in January 2010 among all three data sets. During August 2010, there is a broad region of QFDW amplitudes ranging from 1 - 1.5 K between 30° N and 60° N, and a somewhat narrower region of slightly larger magnitude from 30° - 50° S that is sharply cut off poleward of 50° S. During November and December 2010, there is evidence in all three data sets of increasing QFDW amplitudes from 20° - 60° latitude in each hemisphere, with larger amplitudes and more coherent latitude structure in the SH. The evolution of the QFDW in 2010 is consistent with the seasonal cycle observed during 2002 - 2016 using SABER temperatures (*Huang et al.*, 2017). Their results show a consistent peak near the stratopause of 1 - 4 K from 30° - 50° N in December and January and from 30° - 50° S from June through September. The symmetry shown across the Equator in all three reanalyses during August in **Figure 11.50** is consistent with a QFDW signal related to the hemispherically symmetric normal mode (e.g., *Lieberman et al.*, 2003).

The very good agreement seen in the latitude, altitude, and seasonal variations in QFDW amplitudes for 2010 among the MERRA-2, ERA-Interim, and JRA-55 reanalyses suggests that much of the origin and propagation of the QFDW largely involves stratospheric processes that are well represented in these reanalyses. The two distinct patterns of QFDW amplitudes seen here further suggest that different processes are affecting the development and propagation of the QFDW. The first process, related to the apparent hemispherically symmetric mode, could be related to the interaction of the 5-day normal mode and tropospheric processes such as convective latent heat release (*Garcia and Salby*, 1987). The second process, related to the high Northern latitude maximum in January, could be related to growth through baroclinic/barotropic instability, leading to what is commonly referred to as the 6.5-day wave in the mesosphere and lower thermosphere (*Lieberman et al.*, 2003; *Talaat et al.*, 2002). Subsequent investigations of the QFDW in these and other reanalysis products over longer time periods, focusing on the periodicities of QFDW signals in the mid-latitude and polar latitudes would be helpful to further elucidate possible mechanisms for the origin and propagation of this signal throughout the stratosphere and mesosphere.

11.6 Summary, Key Findings, and Recommendations

In summary, differences in the USLM among reanalyses are smaller in recent years (*vs.* in the 1980s and 1990s), increase with altitude, and increase nearer to the Equator. Improvements in observational data and in data assimilation explain much of the increasing agreement since 1998. The differences increase with altitude because of differences in model top altitude, the characteristics of the sponge layers near the model tops, and the differences in the gravity wave drag parameterizations in this region. The tropical USLM provides a particular challenge because the sparse observations leave key dynamical phenomena in this region weakly constrained in the models. As a result, large differences in USLM features can arise among the different reanalysis systems due to the different physical parameterizations in their respective model components. The intercomparisons presented in this chapter demonstrate that, while no one reanalysis system is clearly better in representing all aspects of the USLM, higher-top systems such as MERRA, MERRA-2, and ERA5 are essential for capturing the mesospheric circulation features such as the SAO and the QTDW, for example. However, we recommend that researchers interested in exploring a particular phenomenon within the USLM see the appropriate section of this chapter before choosing any one reanalysis for use in such research.

We also emphasize here that it is critical to compare reanalyses to independent observations (*e.g.*, radar winds, rocket winds, SABER temperatures). This process is imperative for data users to determine the optimum reanalysis dataset to use and to quantify the differences between a reanalysis dataset and observations prior to each scientific study. To the extent that such independent observations are lacking, we encourage additional observational campaigns to help establish which reanalyses perform best - as well as operational observational platforms to help tether models to observations within the reanalyses. With no firm plans to replace the aging satellites that are currently relied upon for temperature and constituent observations of the middle atmosphere, reanalysis systems could soon lack the key measurements needed to constrain models in the USLM region. Thus, it is imperative that plans are formulated and are executed to continue space-based global observations of the middle atmosphere to ensure the future of accurate simulation of middle atmosphere processes known to impact tropospheric weather forecasting.

Key findings

- Differences among the reanalyses 1) decrease with time due to improvements in assimilated observational data, 2) increase with altitude due to differences in model top, sponge layers, and gravity wave drag treatments, and 3) increase nearer the Equator where sparse observations leave key dynamical phenomena largely unconstrained.

- Although no single reanalysis system is clearly better in representing all aspects of the USLM, higher-top systems such as MERRA and MERRA-2 are essential for capturing mesospheric circulation features such as the SAO and the QTDW.

- Different satellite data assimilated into reanalyses as a function of time introduces discontinuities in both basic state variables and higher order diagnostics and this precludes trend studies based on a single reanalysis system.

- Differences in temperature among the reanalyses increase with height into the mesosphere at all latitudes. Likewise the inter-reanalysis differences in zonal wind increase with height especially in the equatorial region.

- Seasonal mean temperature differences (defined here to be with respect to MERRA) are larger in older reanalyses (ERA-40 and JRA-25) and smaller in newer reanalyses (MERRA-2, ERA-Interim, and JRA-55).

- Westerly and easterly jets in the winter and summer stratosphere, respectively, are well reproduced in MERRA, MERRA-2, ERA-Interim, JRA-55, and CFSR/CFSv2.

- The descending branch of the residual circulation in the winter stratosphere is strongest in MERRA, consistent with results prepared for *Chapter 5* (not shown; *Thomas Birner, personal communication*, 2021).

- There are anomalous vertical temperature gradients around 3 hPa in JRA-25 that lead to anomalous flow in the winter stratosphere and these are not observed in the other reanalyses.

- Noisy meridional and vertical winds in ERA-40 can cause larger dispersion of air parcels, which leads to "younger" age of air values and a weaker subtropical barrier in the stratosphere.

- Throughout the year, MERRA-2 has weaker cross-equatorial flow, a weaker middle-atmosphere Hadley circulation, and a westerly bias in the tropical USLM compared to ERA-Interim, JRA-55, and MERRA.

- Signatures of long-term variability due to the ENSO, the QBO, the 11-year solar cycle, and volcanic eruptions are shown in JRA-55, MERRA-2 and ERA-Interim; there are substantial differences among the reanalyses in the USLM, especially at equatorial latitudes.

- The mean SAO amplitude is reasonable in ERA-I, JRA-55, MERRA and MERRA-2; comparison between JRA-55 and JRA-55C highlights the inability for the free-running model to capture the SAO and the crucial role of assimilating satellite temperatures into this reanalysis system in order to accurately represent the SAO.

- The spatial patterns and magnitudes of inertial instability frequency are in good agreement among MERRA, MERRA-2, ERA-Interim, and JRA-55.

- MERRA, MERRA-2, ERA-Interim, JRA-55, and CFSR/CFSv2 all capture multi-year winter mean polar vortex characteristics in both hemispheres; CFSR wintertime vortex frequencies are 10 - 20 % lower than the other four reanalyses in the 50 ° to 70 ° latitude bands in both hemispheres.

- MERRA, MERRA-2, ERA-Interim, JRA-55, and CFSR/CFSv2 sufficiently capture the multi-year mean seasonal evolution of the polar vortex at the stratopause during 2005 - 2015; interannual variability is not assessed here.

- Quasi-stationary PW-1 amplitudes show remarkable agreement among the reanalyses and with MLS observations in the extratropics during winter; larger differences are seen at lower latitudes and during the summer.

- ES events are generally unconstrained by observations (with the exception of MERRA-2 which assimilates temperatures from Aura MLS after 2004). Their representation in reanalyses depends strongly on the nature of the sponge layer in the underlying forecast model of each reanalysis, and thus reanalyses cannot be regarded as trustworthy to study these phenomena.

- While reanalyses reproduce the global patterns in the diurnal and semi-diurnal migrating tides, their amplitudes are underestimated by 20 - 50 % compared to SABER.

- The representation of the quasi-2-day wave is qualitatively similar in MERRA-2, ERA-Interim, and JRA-55, but there are 50 % differences in amplitude.

- There is excellent agreement in the representation of the quasi-5-day wave among the MERRA-2, ERA-Interim, and JRA-55 reanalyses suggesting that much of its origin and propagation involves stratospheric processes that are well represented in these systems.

Recommendations

- Scientific studies using reanalyses in the USLM should make every effort to also include comparisons with independent observations.

- Large discontinuities that occur due to differences in the data assimilation process preclude trend studies based on a single reanalysis system.

- There are large temperature and wind differences among the reanalyses in the tropical USLM. Using two or more reanalysis datasets to study phenomena (*e.g.*, the SAO, the diurnal tide) in this region of the atmosphere is recommended to increase confidence.

- There are large uncertainties in MERRA-2 zonal winds in the Tropics prior to 1998 as it shows westerly biases in excess of 10 m s^{-1} compared to MERRA, ERA-Interim, and JRA-55 between 10 hPa and 1 hPa.

- There are large uncertainties in "older" reanalysis datasets in the USLM; the meridional circulation in the stratosphere and mesosphere is more realistic in MERRA-2, ERA-Interim, and JRA-55 than in MERRA, ERA-40, and JRA-25.

- Both Eulerian-mean and residual-mean meridional flows in ERA-40 are noisier than those in the other reanalyses, thus, science studies based on ERA-40 residual circulation velocities would likely generate noisier results.

- JRA-55C is not suitable for studies of the SAO.

- Low polar vortex frequency biases in CFSR/CFSv2 (due to high polar temperatures and a weak polar night jet) render this reanalysis dataset less suitable for polar vortex studies compared to MERRA, MERRA-2, ERA-Interim, or JRA-55.

- MERRA, MERRA-2, ERA-Interim, JRA-55, and CFSR/CFSv2 are all suitable to study quasi-stationary PW-1 patterns in the winter extratropics but care should be exercised if the focus is in the subtropics or during the summer.

- Reanalyses should not be relied upon for studying ES events. Even for MERRA-2, the underlying forecast model does not capture the evolution of ES events correctly and so derived quantities (other than temperatures that are directly assimilated) should be treated with caution.

- Older reanalyses such as ERA-40 or JRA-25 are not suitable for tidal studies.

- Tidal results should not be extrapolated from one year to another as the representation of tides is sensitive to the satellite data assimilation.

- There are large uncertainties in using reanalysis data to study 5-day and 2-day wave normal modes; different reanalyses may yield different results.

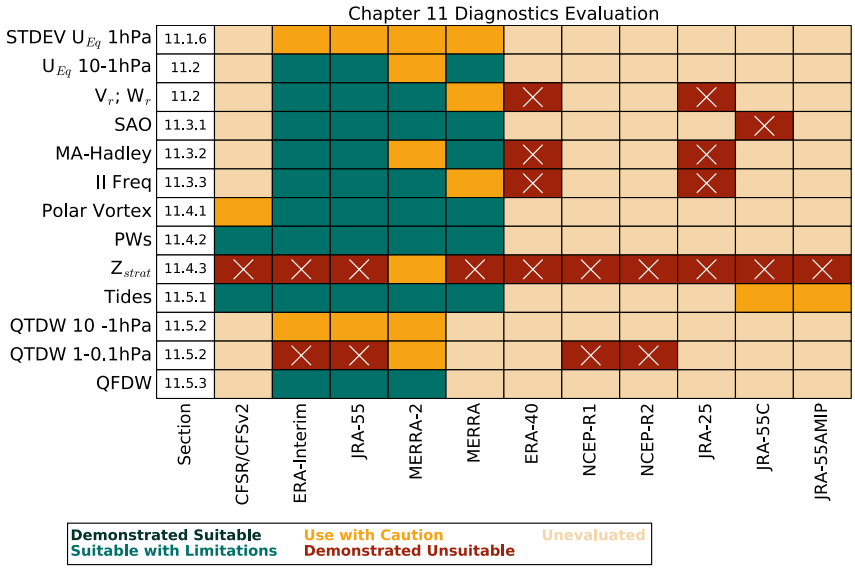

Figure 11.52: *Evaluation table of diagnostics relevant to Chapter 11 topics, listed along the y-axis. Different reanalyses are listed along the x-axis. The corresponding chapter and section numbers are given in the far left column. STDEV is the standard deviation, U_{Eq} is the zonal wind at the Equator, V_r and W_r are residual circulation meridional and vertical velocities, respectively, SAO is the Semi-Annual Oscillation, MA-Hadley is the middle-atmosphere Hadley circulation, II Freq is the inertial instability frequency of occurrence, PWs is planetary waves, Z_{strat} is the height of the stratopause with emphasis on elevated stratopause events, QTDW is the quasi-2-day wave, and QFDW is the quasi-5-day wave.*

Data availability

All of the reanalysis data included in this chapter are publicly accessible. JRA-55, ERA-Interim, and CFSR data are available at the Research Data Archive at the National Center for Atmospheric Research, Computational and Information Systems Laboratory at **https://rda.ucar.edu/**. ERA-Interim data are also available at **http://apps.ecmwf.int/datasets/**. CFSR/CFSv2 data were also made available by Sean Davis at **ftpshare.al.noaa.gov**. The processing of CFSR/CFSv2 output was funded by the NOAA HPC grant "Climate Forecast System Reanalysis products for reanalysis validation and intercomparisons" to NOAA ESRL CSD with the bulk of the work performed by Sean Davis, Jeremiah Sjoberg and H. Leroy Miller. MERRA and MERRA-2 data are available at the NASA Goddard Earth Sciences (GES) Data and Information Services Center (DISC) at **https://gmao.gsfc.nasa.gov/reanalysis/**. TS analyzed diurnal monthly reanalysis data provided under the framework of the Data Integration and Analysis System (DIAS) funded by the Japan Ministry of Education, Culture, Sports, Science and Technology (MEXT). MLS v4.2 data are available from the NASA Goddard Space Flight Center for Earth Sciences DISC at **https://mls.jpl.nasa.gov/data/**. SABER data are available from **http://saber.gats-inc.com/**.

Acknowledgements

VLH acknowledges support from NASA grants NNX-14AH54G, NNX17AB80G, 80NSSC181046, and 80NSSC20K0628, and travel support from the Stratospheric Processes and their Role in Climate (SPARC) Reanalysis Intercomparison Project (S-RIP). JAF acknowledges support from NASA Small Explorer Program contract NAS5-03132 and NASA HGI grant 80NSSC18K0051. MF acknowledges support from the Japan Society for the Promotion of Science (JSPS) through Grants-in-Aid for Scientific Research (16K05548). LJG was supported by the U.K. Natural Environment Research Council (NERC) through the National Centre for Atmospheric Science (NCAS). TH was supported by JSPS KAKENHI Grant Number JP16H04052. PH acknowledges support from the European Research Council through the ACCI project (Grant 267760) and the NASA GNSS Remote Sensing Science Team Grant NNX16AK37G. MH was supported by NSF grant AGS-1555851. GLM was supported by the NASA MeaSUREs MUSTARD project via a JPL subcontract (#1483517). YK was supported by JSPS KAKENHI Grant Number JP15KK0178 and 18H01286. YK also acknowledges Anne Smith for her cubic spline codes used in the calculation of MLS gradient winds. JPM acknowledges support from NASA LWS award NNH13AV95I. YOR was supported by the Research Council of Norway grant SOLENA #255276. TS acknowledges support from the JSPS through Grants-in-Aid for Scientific Research (15K17761). YT was supported by JSPS KAKENHI grant number JP15HP8027. The authors acknowledge useful conversations with Jonathon Wright, Sean Davis, Craig Long, Krzysztof Wargan, Rossana Dragani, Yayoi Harada, and the S-RIP Team.

References

Abalos, M., B. Legras, F. Ploeger, and W. J. Randel, 2015: Evaluating the advective Brewer-Dobson circulation in three reanalyses for the period 1979 - 2012. *J. Geophys. Res. Atmos.,* **120**, 7534 - 7554, doi: 10.1002/2015JD023182.

Allen, D.R., *et al.*, 2000: Antarctic polar descent and planetary wave activity observed in ISAMS CO from April to July 1992. *Geophys. Res. Lett.*, **27**, 665 - 668, doi: 10.1029/1999GL010888.

Andrews, D.G., J.R. Holton, and C.B. Leovy, 1987: Middle Atmosphere Dynamics. *Academic Press*, San Diego, 489 pp., doi: 10.1002/qj.49711548612.

Anstey, J.A., and T.G. Shepherd, 2014: High latitude influence of the quasi-biennial oscillation. *Q. J. Roy. Met. Soc.*, **140**, 1 - 21, doi: 10.1002/qj.2132.

Baldwin, M., et al., 2001: The quasi biennial oscillation. *Rev. Geophys.*, **39**, 179 - 229, doi: 10.1029/1999RG000073.

Baldwin, M.P., and T.J. Dunkerton, 2001: Stratospheric harbingers of anomalous weather regimes. *Science*, **294**, 581 - 584, doi: 10.1126/science.1063315.

Baker, D., *et al.*, 2019: The Scientific Foundation of Space Weather. 587 pp, *Springer Netherlands*, Dordrecht, Netherlands, **https://www.springer.com/gp/book/9789402415872**.

Barnett, J.J., and K. Labitzke, 1990: Climatological distribution of planetary waves in the middle atmosphere. *Adv. Space Res.*, **10**, 63 - 91, doi: 10.1016/0273-1177(90)90387-F.

Becker E., and S. L. Vadas, 2018: Secondary gravity waves in the winter mesosphere: Results from a high-resolution global circulation model. *J. Geophys. Res.*, **123**, 2605 - 2627, doi: 10.1002/2017JD027460.

Beig, G., J. Scheer, M.G. Mlynczak, and P. Keckhut, 2008: Overview of the temperature response in the mesosphere and lower thermosphere to solar activity. *Rev. Geophys.*, **46**, RG3002, doi: 10.1029/2007RG000236.

Bosilovich, M., *et al.*, 2015: MERRA-2: Initial evaluation of the climate. *NASA Tech. Rep. Series on Global Modeling and Data Assimilation*, *NASA/TM–2015-104606*, Vol. **43**, 139 pp.

Burks, D., and C. Leovy, 1986: Planetary waves near the mesospheric easterly jet. *Geophys. Res. Lett.*, **13**, 193 - 196, doi: 10.1029/GL013i003p00193.

Butler, A.H., J.P. Sjoberg, D.J. Seidel, and K.H. Rosenlof, 2017: A sudden stratospheric warming compendium. *Earth Syst. Sci. Data*, **9**, 63 - 76, doi: 10.5194/essd-9-63-2017.

Chandran, A., *et al.*, 2013: A climatology of elevated stratopause events in the whole atmosphere community climate model. *J. Geophys. Res. Atmos.*, **118**, 1234 - 1246, doi: 10.1002/jgrd.50123.

Chang, L.C., S.E. Palo, and H.-L. Liu, 2011: Short-term variability in the migrating diurnal tide caused by interactions with the quasi 2-day wave. *J. Geophys. Res.*, **116**, D12112, doi:10.1029/2010JD014996.

Charlton, A.J., and L.M. Polvani, 2007: A new look at stratospheric sudden warmings. Part I. Climatology and modeling benchmarks. *J. Climate*, **20**, 449 - 469, doi: 10.1175/JCLI3994.1.

Charney, J.G., and P.G. Drazin, 1961: Propagation of planetary-scale disturbances from the lower into the upper atmosphere. *J. Geophys. Res.*, **66**, 83 - 109, doi: 10.1029/JZ066i001p00083.

Chapman, S., and R.S. Lindzen, 1970: Atmospheric Tides, *D. Reidel Publishing Company*, Dordrecht, Holland, 200 pp, doi: 10.1007/978-94-010-3399-2.

Chun, H.-Y. and J.-J. Baik, 1998: Momentum flux by thermally induced internal gravity waves and its approximation for large-scale models. *J. Atmos. Sci.*, **55**, 3299 - 3310, doi: 10.1175/1520-0469(1998)055<3299:MFBTII>2.0.CO;2.

Coy, L., 1979: A possible 2-day oscillation near the tropical stratopause. *J. Atmos. Sci.*, **36**, 1615 - 1618, doi: 10.1175/1520-0469(1979)036<1615:APDONT>2.0.CO;2.

Coy, L., *et al.*, 2016: Structure and Dynamics of the Quasi-Biennial Oscillation in MERRA-2. *J. Climate*, **29**, 5339 - 5354, doi: 10.1175/JCLI-D-15-0809.1.

Crooks S.A., and L.J. Gray, 2005: Characterisation of the 11-year solar signal using a multiple regression analysis of the ERA-40 data set. *J. Climate*, **18**, 996 - 1015, doi: 10.1175/JCLI-3308.1.

Dai, A., and J. Wang, J., 1999: Diurnal and semidiurnal tides in global surface pressure fields. *J. Atmos. Sci.*, **56**, 3874 - 3891, doi: 10.1175/1520-0469(1999)056<3874:DASTIG>2.0.CO;2.

Das, S.S., *et al.*, 2016: Four-decadal climatological intercomparison of rocketsonde and radiosonde with different reanalysis data: results from Thumba equatorial Station. *Q. J. Roy. Meteorol. Soc.*, **142**, 91 - 101, doi: 10.1002/qj.2632.

Dee, D.P., *et al.*, 2011: The ERA-Interim reanalysis: Configuration and performance of the data assimilation system, *Q. J. R. Met. Soc.*, **137**, 553 - 597, doi: 10.1002/qj.828.

Demirhan Bari, D., A. Gabriel, H. Kornich, and D.W.H. Peters, 2013: The effect of zonal asymmetries in the Brewer-Dobson circulation on ozone and water vapor distributions in the northern middle atmosphere. *J. Geophys. Res.*, **118**, 3447 - 3466, doi: 10.1029/2012JD017709.

Diallo, M., B. Legras, and A. Chédin, 2012: Age of stratospheric air in the ERA Interim. *Atmos. Chem. Phys.*, **12**, 12,133 - 12,154, doi: 10.5194/acp-12-12133-2012.

Dunkerton, T.J., 1981: On the inertial stability of the equatorial middle atmosphere. *J. Atmos. Sci.*, **38**, 2354 - 2364, doi: 10.1175/1520-0469(1981)038<2354:OTISFT>2.0.CO;2.

Dunkerton, T. J., 1989: Nonlinear Hadley circulation driven by asymmetric differential heating. *J. Atmos. Sci.*, **46**, 956 - 974, doi: 10.1175/1520-0469(1989)046<0956:NHCDBA>2.0.CO;2.

Dunkerton, T. J., 1991: Nonlinear propagation of zonal winds in an atmosphere with Newtonian cooling and equatorial wave driving. *J. Atmos. Sci.*, **48**, 236 - 263, doi: 10.1175/1520-0469(1991)048<0236:NPOZWI>2.0.CO;2.

Eluszkiewicz, J., *et al.*, 1996: Residual Circulation in the Stratosphere and Lower Mesosphere as Diagnosed from Microwave Limb Sounder Data. *J. Atmos. Sci.*, **53**, 217 - 240, doi: 10.1175/1520-0469(1996)053<0217:RCITSA>2.0.CO;2.

Forbes, J.M., and D. Wu, 2006: Solar tides as revealed by measurements of mesosphere temperature by the MLS experiment on UARS. *J. Atmos. Sci.*, **63**, 1776 - 1797, doi: 10.1175/JAS3724.1.

France, J.A., *et al.*, 2018: Local and remote planetary wave effects on polar mesospheric clouds in the Northern Hemisphere in 2014. *J. Geophys. Res. Atmos.*, **123**, 5149 - 5162, doi: 10.1029/2017JD028224.

Fritts, D.C., and M.J. Alexander, 2003: Gravity wave effects and dynamics in the middle atmosphere. *Rev. Geophysics*, **41**, 1003, doi: 10.1029/2001RG000106.

Fujiwara, M., *et al.,* 2017: Introduction to the SPARC Reanalysis Intercomparison Project (S-RIP) and overview of the reanalysis systems. *Atmos. Chem. Phys.*, **17**, 1417 - 1452, doi: 10.5194/acp-17-1417-2017.

Gabriel, A., *et al.*, 2011: Zonal asymmetries in middle atmospheric ozone and water vapour derived from Odin satellite data 2001 - 2010. *Atmos. Chem. Phys.*, **11**, 9865 - 9885, doi: 10.5194/acp-11-9865-2011.

Garcia, R.R. and M.L. Salby, 1987: Transient Response to Localized Episodic Heating in the Tropics. Part II: Far-Field Behavior. *J. Atmos. Sci.*, **44**, 499 - 532, doi: 10.1175/1520-0469(1987)044<0499:TRTLEH>2.0.CO;2.

Garcia, R.R., and B.A. Boville, 1994: Downward control of the mean meridional circulation and temperature distribution of the polar winter stratosphere. *J. Atmos. Sci.*, **51**, 2238 - 2245, doi: 10.1175/1520-0469(1994)051<2238:COTMMC>2.0.CO;2.

Garcia, R.R., T.J. Dunkerton, R.S. Lieberman, and R.A. Vincent, 1997: Climatology of the semiannual oscillation of the tropical middle atmosphere. *J. Geophys. Res.*, **102**, D22, 26019 - 26032, doi: 10.1029/97JD00207.

Garcia, R.R., R. Lieberman, J.M. Russell, and M.G. Mlynczak, 2005: Large-scale waves in the mesosphere and lower thermosphere observed by SABER. *J. Atmos. Sci.*, **62**, 4384 - 4399, doi: 10.1175/JAS3612.1.

Garcia-Herrera, R., N. Calvo, R.R. Garcia, and M.A. Giorgetta, 2006: Propagation of ENSO temperature signals into the middle atmosphere: A comparison of two general circulation models and ERA-40 reanalysis data. *J. Geophys. Res.*, **111**, D06101, doi:10.1029/2005JD006061.

Garfinkel, C.I., D.W. Waugh, and L.M. Polvani, 2015: Recent Hadley cell expansion: The role of internal atmospheric variability in reconciling modeled and observed trends. *Geophys. Res. Lett.*, **42**, 10,824 - 10,831, doi: 10.1002/2015GL066942.

Gelaro, R., *et al.*, 2017: The Modern-Era Retrospective Analysis for Research and Applications, Version 2 (MERRA-2). *J. Climate*, **30**, 5419 - 5454, doi: 10.1175/JCLI-D-16-0758.1.

Gerrard A.J., *et al.*, 2002: Synoptic scale study of the Arctic polar vortex's influence on the middle atmosphere, 1, Observations. *J. Geophys. Res.*, **111**, D06107, doi: 10.1029/2001JD000681.

Global Modeling and Assimilation Office (GMAO), 2015a: MERRA-2 inst3_3d_asm_Np: 3d, 3-Hourly, Instantaneous, Pressure-Level, Assimilation, Assimilated Meteorological Fields V5.12.4. Greenbelt, MD, USA, *Goddard Earth Sciences Data and Information Services Center (GES DISC)*, Accessed in 2017, doi: 10.5067/QBZ6MG944HW0.

Global Modeling and Assimilation Office (GMAO), 2015b: MERRA-2 inst6_3d_ana_Nv: 3d, 6-Hourly, Instantaneous, Model-Level, Analysis, Analyzed Meteorological Fields V5.12.4. Greenbelt, MD, USA, *Goddard Earth Sciences Data and Information Services Center (GES DISC)*, Accessed in 2017, doi: 10.5067/IUUF4WB9FT4W.

Global Modeling and Assimilation Office (GMAO), 2015c: MERRA-2 inst3_3d_asm_Nv: 3d, 3-Hourly, Instantaneous, Model-Level, Assimilation, Assimilated Meteorological Fields V5.12.4. Greenbelt, MD, USA, *Goddard Earth Sciences Data and Information Services Center (GES DISC)*, Accessed in 2017, doi: 10.5067/WWQSXQ8IVFW8.

Global Modeling and Assimilation Office (GMAO), 2017: Use of MERRA-2 for Atmospheric Chemistry and Transport Studies. **https://gmao.gsfc.nasa.gov/reanalysis/MERRA-2/docs/ANAvsASM.pdf**.

Goncharenko, L.P., J.L. Chau, H.-L. Liu, and A.J. Coster, 2010: Unexpected connections between the stratosphere and ionosphere. *Geophys. Res. Lett.*, **37**, L10101, doi: 10.1029/2010GL043125.

Gu, S.-Y, *et al.*, 2013: Observations of quasi-two-day wave by TIMED/SABER and TIMED/TIDI. *J. Geophys. Res. Atmos.*, **118**, 1624 - 1639, doi: 10.1002/jgrd.50191.

Gray, L.J., *et al.*, 2010: Solar influences on climate. *Rev. Geophys.*, **48**, RG4001, doi: 10.1029/2009RG000282.

Hagan, M.E., J.M. Forbes, and F. Vial, 1995: On modeling migrating solar tides. *Geophys. Res. Lett.*, **22**, 893 - 896, doi: 10.1029/95GL00783.

Hagan, M.E., and J.M. Forbes, 2002: Migrating and nonmigrating diurnal tides in the middle and upper atmosphere excited by tropospheric latent heat release. *J. Geophys. Res.*, **107**, 4754, doi: 10.1029/2001JD001236.

Hagan, M.E., and J.M. Forbes, 2003: Migrating and nonmigrating semidiurnal tides in the upper atmosphere excited by tropospheric latent heat release. *J. Geophys. Res.*, **108**, doi: 10.1029/2002JA009466.

Hamilton, K., 1998: Dynamics of the tropical middle atmosphere: A tutorial review. *Atmosphere-Ocean*, **36**, 319 - 354, doi: 10.1080/07055900.1998.9649616.

Harris, T.J., 1994: A long-term study of the quasi-two-day wave in the middle atmosphere. *J. Atmos. Terr. Phys.*, **56**, 569 - 579, doi: 10.1016/0021-9169(94)90098-1.

Harvey, V.L., and M.H. Hitchman, 1996: A Climatology of the Aleutian High. *J. Atmos. Sci.*, **53**, 2088 - 2101, doi:10.1175/1520-0469(1996)053<2088:ACOTAH>2.0.CO;2.

Harvey, V.L., R.B. Pierce, T.D. Fairlie, and M.H. Hitchman, 2002: A climatology of stratospheric polar vortices and anticyclones. *J. Geophys. Res.*, **107**, 4442, doi: 10.1029/2001JD001471.

Harvey, V.L., et al., 2018: On the upward extension of the polar vortices into the mesosphere. *J. Geophys. Res. Atmos.*, **123**, 9171 - 9191, doi: 10.1029/2018JD028815.

Hayashi, Y., 1971: A generalized method of resolving disturbances into progressive and retrogressive waves by space Fourier and time cross-spectral analyses. *J. Meteorol. Soc. Jpn.*, **49**, 125 - 128, doi: 10.2151/jmsj1965.49.2_125.

Hersbach, H., and D. Dee, 2016: ERA5 reanalysis is in production. *ECMWF Newsletter*, **147**, 7.

Hirota, I., and J.J. Barnett, 1977: Planetary waves in the winter mesosphere - preliminary analysis of nimbus 6 PMR results. *Quart. J. Roy. Meteorol. Soc.*, **103**, 487 - 498. doi: 10.1002/qj.49710343709.

Hitchcock, P., and T.G. Shepherd, 2013: Zonal-mean dynamics of extended recoveries from stratospheric sudden warmings. *J. Atmos. Sci.*, **70**, 688 - 707, doi: 10.1175/JAS-D-12-0111.1.

Hitchman, M.H., and C.B. Leovy, 1986: Evolution of the zonal mean state in the equatorial middle atmosphere during October 1978 - May 1979. *J. Atmos. Sci.*, **43**, 3159 - 3176, doi: 10.1175/1520-0469(1986)043<3159:EOTZMS>2.0.CO;2.

Hitchman, M.H., J.C. Gille, C.D. Rodgers, and G. Brasseur, 1989: The separated polar winter stratopause: A gravity wave driven climatological feature. *J. Atmos. Sci.*, **46**, 410 - 422, doi: 10.1175/1520-0469(1989) 046<0410:TSPWSA>2.0.CO;2.

Holton, J., and H. Tan, 1982: The quasi-biennial oscillation in the Northern Hemisphere lower stratosphere. *J. Meteorol. Soc. Jpn.*, **60**, 140 - 148, doi: 10.2151/jmsj1965.60.1_140.

Hopkins, R.H., 1975: Evidence of polar-tropical coupling in upper stratosphere zonal wind anomalies. *J. Atmos. Sci.*, **32**, 712 - 719, doi: 10.1175/1520-0469(1975)032<0712:EOPTCI>2.0.CO;2.

Huang, Y.Y., *et al.*, 2017: Annual and interannual variations in global 6.5DWs from 20 to 110 km during 2002 - 2016 observed by TIMED/SABER. *J. Geophys. Res. Space Physics*, **122**, 8985 - 9002, doi: 10.1002/2017JA023886.

Ialongo, I., *et al.*, 2012: Ozone zonal asymmetry and planetary wave characterization during Antarctic spring. *Atmos. Chem. Phys.*, **12**, 2603 - 2614, doi: 10.5194/acp-12-2603-2012.

Iimura, H., *et al.*, 2015: Interhemispheric structure and variability of the 5-day planetary wave from meteor radar wind measurements. *Ann. Geophys.*, **33**, 1349 - 1359, doi: 10.5194/angeo-33-1349-2015.

Iwasaki, T., S. Yamada, and K. Tada, 1989a: A parameterization scheme of orographic gravity wave drag with two different vertical partitionings, Part I: Impact on medium range forecasts. *J. Meteorol. Soc. Jpn.*, **67**, 11 - 27, doi: 10.2151/jmsj1965.67.1_11.

Iwasaki, T., S. Yamada, and K. Tada, 1989b: A parameterization scheme of orographic gravity wave drag with two different vertical partitionings, Part II: Zonally averaged budget analyses based on transformed Eulerian-mean method. *J. Meteorol. Soc. Jpn.*, **67**, 29 - 41, doi: 10.2151/jmsj1965.67.1_29.

Iwasaki, T., H. Hamada, and K. Miyazaki, 2009: Comparisons of Brewer-Dobson circulations diagnosed from reanalysis. *J. Meteorol. Soc. Jpn.*, **87**, 997 - 1006, doi: 10.2151/jmsj.87.997.

Kawatani, Y., *et al.*, 2016: Representation of the tropical stratospheric zonal wind in global atmospheric reanalysis. *Atmos. Chem. Phys.*, **16**, 6681 - 6699, doi: 10.5194/acp-16-6681-2016.

Kawatani, Y., *et al.*, 2020: Representation of the equatorial stratopause semiannual oscillation in global atmospheric reanalyses. *Atmos. Chem. Phys.*, **20**, 9115 - 9133, doi: 10.5194/acp-20-9115-2020.

Kim, Y.-J. and A. Arakawa, 1995: Improvement of orographic gravity wave parameterization using a mesoscale gravity wave model. *J. Atmos. Sci.*, **83**, 1875 - 1902, doi: 10.1175/1520-0469(1995)052<1875:IOOGWP>2.0.CO;2.

Kishore Kumar, G., K. Kishore Kumar, G. Baumgarten, and G. Ramkumar, 2015: Validation of MERRA reanalysis upper-level winds over low latitudes with independent rocket sounding data. *J. Atmos. Sol. Terr. Phys.*, **123**, 48 - 54, doi: 10.1016/j.jastp.2014.12.001.

Knox, J.A., 2003: Inertial instability. In *Encyclopedia of the Atmospheric Sciences*, edited by J. R. Holton, J. Pyle, and J. A. Curry, pp. 1004 - 1013, Elsevier, New York.

Knox, J.A., and V.L. Harvey, 2005: Global climatology of inertial instability and Rossby wave breaking in the stratosphere. *J. Geophys. Res.*, **110**, D06108, doi: 10.1029/2004JD005068.

Kobayashi, S., *et al.*, 2015: The JRA-55 reanalysis: General specifications and basic characteristics. *J. Meteorol. Soc. Jpn.*, **93**, 5 - 48, doi: 10.2151/jmsj.2015-001.

Kouker, W., and G. Brasseur, 1986: Transport of atmospheric tracers by planetary waves during a winter stratospheric warming event: A three-dimensional model simulation. *J. Geophys. Res.*, **91**, 13167 - 13185, doi: 10.1029/JD091iD12p13167.

Labitzke, K., 1972: Temperature changes in the mesosphere and stratosphere connected with circulation changes in winter. *J. Atmos. Sci.*, **29**, 756 - 766, doi: 10.1175/1520-0469(1972)029<0756:TCITMA>2.0.CO;2.

Lieberman, R.S., 1999: Eliassen-Palm fluxes of the 2-day wave. *J. Atmos. Sci.*, **56**, 2846 - 2861, doi: 10.1175/1520-0469(1999)056<2846:EPFOTD>2.0.CO;2.

Lieberman, R.S., *et al.*, 2003: The 6.5-day wave in the mesosphere and lower thermosphere: Evidence for baroclinic/barotropic instability. *J. Geophys. Res.*, **108**, 4640, doi: 10.1029/2002JD003349.

Lieberman, R.S., D.M. Riggin, and D.E. Siskind, 2013: Stationary waves in the wintertime mesosphere: Evidence for gravity wave filtering by stratospheric planetary waves. *J. Geophys. Res. Atmos.*, **118**, 3139 - 3149, doi: 10.1002/jgrd.50319.

Lilienthal, F., C. Jacobi, and C. Geibler, 2018: Forcing mechanisms of the terdiurnal tide. *Atmos. Chem. Phys.*, **18**, 15725 - 15742, doi: 10.5194/acp-18-15725-2018.

Limpasuvan, V., C.B. Leovy, and Y.J. Orsolini, 2000: Observed temperature two-day wave and its relatives near the stratopause. *J. Atmos. Sci.*, **57**, 1689 - 1701, doi: 10.1175/1520-0469(2000)057<1689:OTTDWA>2.0.CO;2.

Limpasuvan, V., and D.L. Wu, 2003: Two-day wave observations of UARS Microwave Limb Sounder mesospheric water vapor and temperature. *J. Geophys. Res.*, **108**, 4307, doi: 10.1029/2002JD002903.

Limpasuvan, V., *et al.*, 2012: The roles of planetary and gravity waves during a major stratospheric sudden warming as characterized in WACCM. *J. Atmos. Sol. Terr. Phys.*, **78–79**, 84-98, doi: 10.1016/j.jastp.2011.03.004.

Liu, H.L., and R.G. Roble, 2002: A study of a self-generated stratospheric sudden warming and its mesospheric-lower thermospheric impacts using the coupled TIME-GCM/CCM3. *J. Geophys. Res.*, **107**, doi: 10.1029/2001JD001533.

Liu, H., E. Doornbos, M. Yamamoto, and S. Tulasi Ram, 2011: Strong thermospheric cooling during the 2009 major stratosphere warming. *Geophys. Res. Lett.*, **38**, L12102, doi: 10.1029/2011GL047898.

Livesey, N.J., *et al.,* 2017: Earth Observing System (EOS) Aura Microwave Limb Sounder (MLS) version 4.2X Level 2 data quality and description document. *Rep. JPL D-33509* Rev. **C**, Jet Propul. Lab., Pasadena, Calif.

Long, C.S., *et al.*, 2017: Climatology and interannual variability of dynamic variables in multiple reanalyses evaluated by the SPARC Reanalysis Intercomparison Project (S-RIP). *Atmos. Chem. Phys.*, **17**, 14593 - 14629, doi: 10.5194/acp-17-14593-2017.

Lott, F. and M.J. Miller, 1997: A new subgrid-scale orographic drag parametrization: Its formulation and testing. *Q. J. Roy. Meteorol. Soc.*, **123**, 101 - 127, doi: 10.1002/qj.49712353704.

Madden, R. and P. Julian, 1972: Further evidence of global-scale 5-day pressure waves. *J. Atmos. Sci.*, **29**, 1464 - 1469, doi: 10.1175/15200469(1972)029<1464:FEOGSD>2.0.CO;2.

Manney, G.L., and T.R. Nathan, 1990: Barotropic Stability of Westward-Moving Waves in Realistic Stratospheric Zonal Flows. *J. Atmos. Sci.*, **47**, 775-794, doi: 10.1175/1520-0469(1990)047<0775:BSOWMW>2.0.CO;2.

Manney, G.L., *et al.*, 2008: The evolution of the stratopause during the 2006 major warming: Satellite data and assimilated meteorological analyses. *J. Geophys. Res.*, **113**, D11115, doi: 10.1029/2007JD009097.

Manney, G.L., *et al.*, 2009: Aura Microwave Limb Sounder observations of dynamics and transport during the record-breaking 2009 Arctic stratospheric major warming. *Geophys. Res. Lett.*, **36**, L12815, doi: 10.1029/2009GL038586.

McCormack, J.P., L. Coy, and K.W. Hoppel, 2009: Evolution of the quasi 2-day wave during January 2006. *J. Geophys. Res.*, **114**, D20115, doi: 10.1029/2009JD012239.

McCormack, J.P., L. Coy, and W. Singer, 2014: Intraseasonal and interannual variability of the quasi 2-day wave in the Northern Hemisphere summer mesosphere. *J. Geophys. Res. Atmos.*, **119**, 2928 - 2946, doi:10.1002/2013JD020199.

McFarlane, N.A., 1987: The effect of orographically excited gravity-wave drag on the circulation of the lower stratosphere and troposphere. *J. Atmos. Sci.*, **44**, 1775 - 1800, doi: 10.1175/1520-0469(1987)044<1775:TEOOEG>2.0.CO;2.

McLandress, C., *et al.*, 2006: Large-scale dynamics of the mesosphere and lower thermosphere: An analysis using the extended Canadian Middle Atmosphere Model. *J. Geophys. Res.*, **111**, D17111. doi: 10.1029/2005JD006776.

McLandress, C., *et al.*, 2013: Dynamical control of the mesosphere by orographic and nonorographic gravity wave drag during the extended northern winters of 2006 and 2009. *J. Atmos. Sci.*, **70**, 2152 - 2169, doi: 10.1175/JAS-D-12-0297.1.

McLandress, C., D.A. Plummer, and T.G. Shepherd, 2014: Technical Note: A simple procedure for removing temporal discontinuities in ERA-Interim upper stratospheric temperatures for use in nudged chemistry-climate model simulations. *Atmos. Chem. Phys*., **14**, 1547 - 1555, doi: 10.5194/acp-14-1547-2014.

Mitchell, D.M., *et al.*, 2015: Signatures of naturally induced variability in the atmosphere using multiple reanalysis datasets. *Q. J. Roy. Met. Soc.*, **141**, 2011 - 2031, doi: 10.1002/qj.2492.

Miyoshi, Y., and T. Hirooka, 2003: Quasi-biennial variation of the 5-day wave in the stratosphere. *J. Geophys. Res.*, **108**, 4620, doi: 10.1029/2002JD003145.

Molod, A., L. Takacs, M. Suarez, and J. Bacmeister, 2015: Development of the GEOS-5 atmospheric general circulation model: evolution from MERRA to MERRA-2. *Geosci. Model Dev.*, **8**, 1339 - 1356, doi: 10.5194/gmd-8-1339-2015.

Monge-Sanz, B.M., M.P. Chipperfield, A.J. Simmons, and S.M. Uppala, 2007: Mean age of air and transport in a CTM: Comparison of different ECMWF analyses. *Geophys. Res. Lett*. **34**, L04801, doi: 10.1029/2006GL028515.

Muller, H.G., and L. Nelson, 1978: A traveling quasi 2-day wave in the meteor region. *J. Atmos. Terr. Phys.*, **40**, 761 - 766, doi: 10.1016/0021-9169(78)90136-8.

Nielsen, K., *et al.*, 2010: Seasonal variation of the quasi 5-day planetary wave: Causes and consequences for polar mesospheric cloud variability in 2007. *J. Geophys. Res.*, **115**, D18111, doi: 10.1029/2009JD012676.

Norton, W.A., and J. Thuburn, 1999: Sensitivity of mesospheric mean flow, planetary waves, and tides to strength of gravity wave drag. *J. Geophys. Res.*, **104**, 30,897 - 30,911, doi: 10.1029/1999JD900961.

Offermann, D., *et al.*, 2003: Zonal asymmetries in middle atmosphere temperatures. *Adv. Space. Res.*, **32**, 1771 - 1780, doi: 10.1016/S0273-1177(03)90475-3.

Onogi, K., *et al.*, 2007: The JRA-25 reanalysis. *J. Meteorol. Soc. Jpn.*, **85**, 369 - 432, doi: 10.2151/jmsj.85.369.

Orbe, C., *et al.*, 2017: Large-Scale Atmospheric Transport in GEOS Replay Simulations. *J. Adv. Mod. Earth Sys.*, **9**, 2545 - 2560, doi: 10.1002/2017MS001053.

Orr, A., *et al.*, 2010: Improved middle atmosphere climate and forecasts in the ECMWF model through a non-orographic gravity wave drag parametrization. *J. Climate*, **23**, 5905 - 5926, doi: 10.1175/2010JCLI3490.1.

Orsolini, Y.J., V. Limpasuvan, and C.B. Leovy, 1997: The tropical stratopause response in the UKMO stratospheric analyses: Evidence for a 2-day wave and inertial circulations. *Q. J. R. Meteorol. Soc.*, **123**, 1707 - 1724, doi: 10.1002/qj.49712354212.

Orsolini, Y.J., *et al.*, 2017: Modelling the descent of nitric oxide during the elevated stratopause event of January 2013. *J. Atmos. Sol. Terr. Phys*., **155**, 50 - 61, doi: 10.1016/j.jastp.2017.01.006.

Pancheva, D.V., 2006: Quasi-2-day wave and tidal variability observed over Ascension Island during January/February 2003. *J. Atmos. T Sol. err. Phys*., **68**, 390 - 407, doi: 10.1016/j.jastp.2005.02.028.

Pascoe, C.L., *et al.*, 2005: The quasi biennial oscillation: analysis using ERA-40 data. *J. Geophys. Res.*, **110**, D08105, doi: 10.1029/2004D004941.

Pedatella, N.M., *et al.*, 2014: The neutral dynamics during the 2009 sudden stratosphere warming simulated by different whole atmosphere models. *J. Geophys. Res. Space Physics*, **119**, 1306 - 1324, doi: 10.1002/2013JA019421.

Pedatella, N.M., *et al.*, 2018: How sudden stratospheric warming affects the whole atmosphere. *Eos*, **99**, doi: 10.1029/2018EO092441.

Pfister, L., 1985: Baroclinic instability of easterly jets with applications to the summer mesosphere. *J. Atmos. Sci.*, **42**, 313 - 330, doi: 10.1175/1520-0469(1985)042<0313:BIOEJW>2.0.CO;2.

Plumb, R.A., 1983: Baroclinic instability of the summer mesosphere: A mechanism for the quasi-two-day wave? *J. Atmos. Sci.*, **40**, 262 - 270, doi: 10.1175/1520-0469(1983)040<0262:BIOTSM>2.0.CO;2.

Plumb, A., and J. Eluszkiewicz, 1999: The Brewer–Dobson circulation: Dynamics of the tropical upwelling. *J. Atmos. Sci.*, **56**, 868 - 890, doi: 10.1175/1520-0469(1999)056,0868: TBDCDO.2.0.CO;2.

Polichtchouk, I., *et al.,* 2017: What influences the middle atmosphere circulation in the IFS? *ECMWF Technical Memorandum* No. **809**. doi: 10.21957/mfsnfv15o.

Randall, C.E., *et al.*, 2006: Enhanced NO_x in 2006 linked to strong upper stratospheric Arctic vortex. *Geophys. Res. Lett.*, **33**, L18811, doi: 10.1029/2006GL027160.

Randall, C.E., *et al*., 2015: Simulation of energetic particle precipitation effects during the 2003–2004 Arctic winter. *J. Geophys. Res. Space Phys.*, **120**, 5035 - 5048, doi: 10.1002/2015JA021196.

Randel, W.J., 1994: Observations of the 2-day wave in NMC stratospheric analyses. *J. Atmos. Sci.*, **51**, 306 - 313, doi: 10.1175/1520-0469(1994)051<0306:OOTDWI>2.0.CO;2.

Remsberg, E.E., *et al.,* 2003: On the verification of the quality of SABER temperature, geopotential height, and wind fields by comparison with Met Office assimilated analyses. *J. Geophys. Res. Atmos.*, **108**, doi: 10.1029/2003JD003720.

Rienecker, M.M., *et al.*, 2011: MERRA: NASA's Modern-Era Retrospective Analysis for Research and Applications. *J. Climate*, **24**, 3624 - 3648, doi: 10.1175/JCLI-D-11-00015.1.

Rodgers, C.D., and A.J. Prata, 1981: Evidence for a traveling two-day wave in the middle atmosphere. *J. Geophys. Res.*, **86**, 9661 - 9664, doi: 10.1029/JC086iC10p09661.

Rojas, M., and W. Norton, 2007: Amplification of the 2-day wave from mutual interaction of the global Rossby-gravity and local modes in the summer mesosphere. *J. Geophys. Res.*, **112**, D12114, doi: 10.1029/2006JD008084.

Saha, S., *et al.*, 2010: The NCEP climate forecast system reanalysis. *Bull. Am. Meteo. Soc.*, **91**, 1015 - 1057, doi: 10.1175/2010BAMS3001.1.

Saha, S., *et al.*, 2014: The NCEP Climate Forecast System version 2. *J. Climate*, **27**, 2185 - 2208, doi: 10.1175/JCLI-D-12-00823.1.

Sakazaki, T., et al., 2012: Diurnal tides from the troposphere to the lower mesosphere as deduced from TIMED/SABER satellite data and six global reanalysis data sets. *J. Geophys. Res.*, **117**, D13108, doi: 10.1029/2011JD017117.

Sakazaki, T., K. Sato, Y. Kawatani, and S. Watanabe, S., 2015: Three-dimensional structures of tropical nonmigrating tides in a high-vertical-resolution general circulation model. *J. Geophys. Res. Atmos.*, **120**, 1759 - 1775, doi: 10.1002/2014JD022464.

Sakazaki, T., M. Fujiwara, and M. Shiotani, M., 2018: Representation of solar tides in the stratosphere and lower mesosphere in state-of-the-art reanalyses and in satellite observations. *Atmos. Chem. Phys.*, **18**, 1437 - 1456, doi: 10.5194/acp-18-1437-2018.

Sassi, F., R.R. Garcia, B.A. Boville, and H. Liu, 2002: On temperature inversions and the mesospheric surf zone. *J. Geophys. Res.*, **107**, 4380, doi: 10.1029/2001JD001525.

Sato M., J. Hansen, M. McCormick, and J. Pollack, 1993: Stratospheric aerosol optical depths, 1850 - 1990. *J. Geophys. Res.*, **98**, 22987 - 22994, doi: 10.1029/93JD02553.

Sato, K., *et al.*, 2009: On the origins of mesospheric gravity waves. *Geophys. Res. Lett.*, **36**, L19801, doi: 10.1029/2009GL039908.

Sato, K., and S. Hirano, 2019: The Climatology of Brewer-Dobson Circulation and the Contribution of Gravity Waves. *Atmos. Chem. Phys.*, **19**, 4517 - 4539, doi: 10.5194/acp-19-4517-2019.

Semeniuk, K., and T.G. Shepherd, 2001a: The middle-atmosphere Hadley circulation and equatorial inertial adjustment. *J. Atmos. Sci.*, **58**, 3077 - 3096, doi: 10.1175/1520-0469(2001)058<3077:TMAHCA>2.0.CO;2.

Semeniuk, K., and T.G. Shepherd, 2001b: Mechanisms for tropical upwelling in the stratosphere. *J. Atmos. Sci.*, **58**, 3097 - 3115, doi: 10.1175/1520-0469(2001)058<3097:MFTUIT>2.0.CO;2.

Schoeberl, M.R., and D.L. Hartmann, 1991: The dynamics of the stratospheric polar vortex and its relation to springtime ozone depletions. *Science*, **251**, 46 - 52, doi: 10.1126/science.251.4989.46.

Schoeberl, M., A. Douglass, Z. Zhu, and S. Pawson, 2003: A comparison of the lower stratospheric age spectra derived from a general circulation model and two data assimilation systems. *J. Geophys. Res.*, **108**, 4113, doi: 10.1029/2002JD002652.

Shepherd, T.G., K. Semeniuk, and J.N. Koshyk, 1996: Sponge layer feedbacks in middle-atmosphere models. *J. Geophys. Res.*, **101**, 23447 - 23464, doi: 10.1029/96JD01994.

Shepherd, T.G., I. Polichtchouk, R.J. Hogan, and A.J. Simmons, 2018: Report on Stratosphere Task Force. *ECMWF Technical Memorandum* **824**.

Shiotani, M., and I. Hirota, 1985: Planetary wave-mean flow interaction in the stratosphere: a comparison between northern and southern hemispheres. *Q. J. Roy. Meteorol. Soc.*, **111**, 309 - 334, doi: 10.1002/qj.49711146804.

Simmons, A.J., *et al.*, 2014: Estimating low frequency variability and trends in atmospheric temperature using ERA Interim. *Q. J. Roy. Meteorol. Soc.*, **140**, 329 - 353, doi: 10.1002/qj.2317.

Siskind, D.E., L. Coy, and P. Espy, 2005: Observations of stratospheric warmings and mesospheric coolings by the TIMED SABER instrument. *Geophys. Res. Lett.*, **32**, L09804, doi: 10.1029/2005GL022399.

Siskind, D.E., *et al*., 2007: On recent interannual variability of the Arctic winter mesosphere: Implications for tracer descent. *Geophys. Res. Lett*., doi: 10.1029/2007GL029293.

Siskind, D.E. , *et al.*, 2010: Case studies of the mesospheric response to recent minor, major, and extended stratospheric warmings. *J. Geophys. Res.*, **115**, D00N03, doi: 10.1029/2010JD014114.

Siskind, D.E., and J.P. McCormack, 2014: Summer mesospheric warmings and the quasi 2-day wave. *Geophys. Res. Lett*., **41**, 717 - 722, doi: 10.1002/2013GL058875.

Smith, A.K., 1996: Longitudinal variations in mesospheric winds: evidence for gravity wave filtering by planetary waves. *J. Atmos. Sci.*, **53**, 1156 - 1173, doi:10.1175/1520-0469(1996)053<1156:LVIMWE>2.0.CO;2.

Smith, A.K., 1997: Stationary planetary waves in upper mesospheric winds. *J. Atmos. Sci.*, **54**, 2129 - 2145, doi: 10.1175/1520-0469(1997)054<2129:SPWIUM>2.0.CO;2.

Smith, A.K., R.R. Garcia, A.C. Moss, and N.J. Mitchell, 2017: The semiannual oscillation of the tropical zonal wind in the middle atmosphere derived from satellite geopotential height retrievals. *J. Atmos. Sci.*, **74**, 2413 - 2425, doi: 10.1175/JAS-D-17-0067.1.

Smith, T.M., and R.W. Reynolds, 2003: Extended reconstruction of global sea surface temperatures based on COADS data (1854 - 1997). *J. Climate*, **16**, 1495 - 1510, doi: 10.1175/1520-0442-16.10.1495.

Talaat, E.R., J.-H. Yee, and X. Zhu, 2001: Observations of the 6.5-day wave in the mesosphere and lower thermosphere. *J. Geophys. Res.*, **106**, 20715 - 20723, doi: 10.1029/2001JD900227.

Talaat, E.R., J.-H. Yee, and X. Zhu, 2002: The 6.5-day wave in the tropical stratosphere and mesosphere. *J. Geophys. Res.*, **107**, 4133, doi: 10.1029/2001JD000822.

Tomikawa, Y., *et al.*, 2008: Wintertime temperature maximum at the subtropical stratopause in a T213L256 GCM. J. *Geophys. Res.*, **113**, D17117, doi:10.1029/2008JD009786.

Tomikawa, Y., *et al.*, 2012: Growth of planetary waves and the formation of an elevated stratopause after a major stratospheric sudden warming in a T213L256 GCM. *J. Geophys. Res.*, **117**, D16101, doi: 10.1029/2011JD017243.

Tunbridge, V.M., D.J. Sandford, and N.J. Mitchell, 2011: Zonal wave numbers of the summertime 2-day planetary wave observed in the mesosphere by EOS Aura Microwave Limb Sounder. *J. Geophys. Res.*, **116**, D11103, doi: 10.1029/2010JD014567.

Tung, K.K., and J.S. Kinnersley, 2001: Mechanisms by which extratropical wave forcing in the winter stratosphere induces upwelling in the summer hemisphere. *J. Geophys. Res.*, **106**, 22781 - 22791, doi: 10.1029/2001JD900228.

Uppala, S.M., *et al.*, 2005: The ERA-40 reanalysis. *Q. J. Roy. Meteorol. Soc.*, **131**, 2961 - 3012, doi: 10.1256/qj.04.176.

Walterscheid, R.L., G.G. Sivjee, and R.G. Roble, 2000: Mesospheric and lower thermospheric manifestations of a stratospheric warming event over Eureka, Canada (80°N). *Geophys. Res. Lett.*, **27**, 2897 - 2900, doi: 10.1029/2000GL003768.

Wang, Y.M., J. Lean, and N. Sheeley Jr., 2005: Modeling the Sun's magnetic field and irradiance since 1713. *J. Astrophys.*, **625**, 522 - 538, doi: 10.1086/429689.

Watanabe, S., *et al.*, 2008: General aspects of a T213L256 middle atmosphere general circulation model. *J. Geophys. Res.*, **113**, D12110, doi: 10.1029/2008JD010026.

Waters, J.W., *et al.*, 2006: The Earth Observing System microwave limb sounder (EOS MLS) on the Aura satellite. *IEEE Trans. Geosci. Remote Sens.*, **44**, 1075 - 1092, doi: 10.1109/TGRS.2006.873771.

Waugh, D.W., and L.M. Polvani, 2010: Stratospheric polar vortices, in The Stratosphere: Dynamics, Transport, and Chemistry. *Geophys. Monogr. Ser.*, **190,** edited by L. M. Polvani, A. H. Sobel, and D. W. Waugh, pp. 43–57, AGU, Washington, DC, doi:10.1029/2009GM000887.

Wu, D.L., *et al.*, 1993: Observations of the quasi 2-day wave from the High Resolution Doppler Imager on UARS. *Geophys. Res. Lett.*, **20**, 2853 - 2856, doi: 10.1029/93GL03008.

Yue, J., W. Wang, A.D. Richmond, and H.-L. Liu, 2012: Quasi-two-day wave coupling of the mesosphere and lower thermosphere-ionosphere in the TIME-GCM: Two-day oscillations in the ionosphere. *J. Geophys. Res.*, **117**, A07305, doi: 10.1029/2012JA017815.

Zhang, X., *et al.*, 2006: Monthly tidal temperatures 20 - 120 km from TIMED/SABER. *J. Geophys. Res.*, **111**, A10S08, doi: 10.1029/2005JA011504.

Zou, C.-Z., *et al.*, 2014: Recalibration and merging of SSU observations for stratospheric temperature trend studies. *J. Geophys. Res. Atmos.*, **119**, 13,180 - 13,205, doi: 10.1002/2014JD021603.

Major abbreviations and terms

2DFFT	two-dimensional fast Fourier transform
AMIP	Atmospheric Model Intercomparison Project
ATOVS	Advanced TIROS Operational Vertical Sounder
CFSR	Climate Forecast System Reanalysis of the NCEP
CFSv2	Climate Forecast System version 2
DJF	December-January-February
ECMWF	European Centre for Medium-Range Weather Forecasts
ENSO	El Niño Southern Oscillation
EOF	Empirical Orthogonal Function
EOS	Earth Observing System
ERA-40	ECMWF 40-year reanalysis
ERA-Interim	ECMWF interim reanalysis
ERA5	the fifth major global reanalysis produced by ECMWF
ERSST	Extended Reconstructed Sea Surface Temperature
IFS	Integrated Forecast System
JJA	June-July-August
JRA-25	Japanese 25-year Reanalysis
JRA-55	Japanese 55-year Reanalysis
JRA-55AMIP	Japanese 55-year Reanalysis based on AMIP-type simulations
JRA-55C	Japanese 55-year Reanalysis assimilating Conventional observations only
MERRA	Modern Era Retrospective-Analysis for Research and Applications
MERRA-2	Modern Era Retrospective-Analysis for Research and Applications, Version 2
MLS	Microwave Limb Sounder
MLT	Mesosphere Lower Thermosphere
NCEP	National Centers for Environmental Prediction
NH	Northern Hemisphere
NOAA	National Oceanic and Atmospheric Administration
NRLSSI	Naval Research Laboratory model for Solar Spectral Irradiance
PMC	Polar Mesospheric Cloud
PW-1 / PW-2	Planetary Wave number 1/Planetary Wave number 2
QBO	Quasi-Biennial Oscillation
QFDW	Quasi-Five-Day Wave
QTDW	Quasi-Two-Day Wave
SABER	Sounding of the Atmosphere using Broadband Emission Radiometry
SAO	Semi-Annual Oscillation
SH	Southern Hemisphere
S-RIP	SPARC Reanalysis Intercomparison Project
SSU	Stratospheric Sounding Unit
SSW	Sudden Stratospheric Warming
TIMED	Thermosphere • Ionosphere • Mesosphere • Energetics and Dynamics
TIROS	Television and InfraRed Observation Satellite
TOVS	TIROS Operational Vertical Sounder
USLM	Upper Stratosphere Lower Mesosphere